Structure formation in alternatives to ΛCDM

MATTEO LEO

Structure formation in alternatives to ΛCDM

Matteo Leo

A Thesis presented for the degree of
Doctor of Philosophy

Institute for Particle Physics Phenomenology
Department of Physics
Durham University
United Kingdom

May 2019

Structure formation in alternatives to ΛCDM

Matteo Leo

Submitted for the degree of Doctor of Philosophy

May 2019

Abstract: The standard ΛCDM is currently the most accepted theory of the Universe. The model is characterised by a nearly-scale invariant primordial curvature power spectrum from inflation, cold and non-interacting dark matter particles and a cosmological constant Λ. Despite the success of ΛCDM, the nature of the dark sectors is still unknown. Moreover, the model faces some small-scale observational controversies that are still not resolved. In this thesis, we investigate structure formation in alternative scenarios to ΛCDM using high-resolution cosmological simulations. In the first part, we focus on non-cold dark matter (e.g. warm dark matter) and non-standard inflation (e.g. thermal inflation) models, that display damped matter density fluctuations on small scales. We investigate first the effects of adding thermal velocities to the gravitationally-induced velocities in simulations of warm dark matter. Considering different non-standard linear power spectra, we then assess which features survive the non-linear evolution and leave interesting signatures in non-linear power spectra and halo statistics. Exploiting these results, we present a new smooth-k space filter, to use in the Press-Schechter approach, to model the dark matter halo mass function, which overcomes shortcomings of other filters used in the literature. In the second part, we quantify the effects of modified gravity on neutral hydrogen abundances and 21-cm power spectra, finding that the HI clustering is a powerful test of gravity at redshifts $z \sim 3$.

Contents

List of Figures

List of Tables

Declaration

The work in this thesis is based on research carried out at the Institute for Particle Physics Phenomenology (IPPP) and the Institute for Computational Cosmology (ICC) in the Department of Physics at the University of Durham, United Kingdom. No part of this thesis has been submitted elsewhere for any other degree or qualification and it is all my own work unless referenced to the contrary in the text.

The contents of this work have appeared in the following papers.

- **M. Leo**, C. M. Baugh, B. Li, S. Pascoli, *The Effect of Thermal Velocities on Structure Formation in N-body Simulations of Warm Dark Matter*, JCAP **11**, 017 (2017) [arXiv:1706.07837 [astro-ph.CO]] (Ref. [1]) (**Chapter 2**).

- **M. Leo**, C. M. Baugh, B. Li, S. Pascoli, *Non-linear growth of structure in cosmologies with damped matter fluctuations*, JCAP **08**, 001 (2018), [arXiv:1712.02742 [astro-ph.CO]] (Ref. [2]) (**Chapter 3**).

- **M. Leo**, C. M. Baugh, B. Li, S. Pascoli, *A new smooth-k space filter approach to calculate halo abundances*, JCAP **04**, 010 (2018), [arXiv:1801.02547 [astro-ph.CO]] (Ref. [3]) (**Chapter 4**).

- **M. Leo**, C. M. Baugh, B. Li, S. Pascoli, *N-body simulations of structure formation in thermal inflation cosmologies*, JCAP **12**, 010 (2018), [arXiv:1807.04980 [astro-ph.CO]] (Ref. [4]) (**Chapter 5**).

The content of **Chapter 6** is based on the paper in preparation Ref. [5]. All figures presented in this thesis were prepared by the author.

Acknowledgements

First and foremost, I would like to thank my supervisors Silvia, Carlton and Baojiu for their support, patience and excellent guidance over these past years. Thank you for giving me the opportunity to continue to work and improve myself, supporting my career with valuable advices and pushing me to achieve important goals, even in the periods in which I was too pessimistic and I wanted to give up. I would like to thank Silvia and Baojiu also for the financial support provided by their grants during the PhD and Carlton for important discussions and tips on my future career. You are exceptional mentors and I could not have asked for a better supervision.

I would like to thank the European Research Council for their support during the PhD under ERC Grant "NuMass" (FP7- IDEAS-ERC ERC-CG 617143) and Starting Grant (ERC-StG-716532-PUNCA).

A special thank to Lydia, John and all the COSMA staff for being always keen to help me. Your prompt solutions to my problems were of crucial importance in achieving the results presented in this thesis. This work used the DiRAC Data Centric system at Durham University, operated by the Institute for Computational Cosmology on behalf of the STFC DiRAC HPC Facility (www.dirac.ac.uk). This equipment was funded by BIS National E-infrastructure capital grant ST/K00042X/1, STFC capital grants ST/H008519/1 and ST/K00087X/1, STFC DiRAC Operations grant ST/K003267/1 and Durham University. DiRAC is part of the National E-Infrastructure.

Thanks to my collaborators Christian Arnold and Tom Theuns for their fundamental help and contribution in developing the subjects presented in this thesis. I would

like also to thank Sownak Bose, Michael Buehlmann, Marius Cautun, Liang Gao, Jianhua He, Mark Lovell, Oliver Newton and Difu Shi for valuable comments and discussions on my research results. I truly enjoyed working with you all.

Thanks to my IPPP and ICC mates, to all my friends outside the Department of Physics and to the Pisiboys. Your company, discussions and laughs have been an important support for me during these years.

Thanks to my parents and my brother Alessandro for their infinite patience, support (moral and financial) and help during all my life. Although you are far from me physically, you are always on my mind and are my source of inspiration. I would like also to thank all my family-in-law for their important support, tips and financial help. Thank you for considering me as a son.

Finally, to the two loves of my life: Marzia and Lucrezia. Marzia, we have started together this adventure and, hopefully, we will finish it together. I hope that our future will be always as it was our past, full of achievements and fun. Thank you for being my wife, friend and co-worker. Without you, none of this would have been possible. Lucrezia, you have entered my life in the middle of these beautiful years, thank you for all the happiness you have brought to our family. I hope this little adventure of your father will inspire you to always achieve your goals and to fight for your dreams.

There is a theory which states that if ever anyone discovers exactly what the Universe is for and why it is here, it will instantly disappear and be replaced by something even more bizarre and inexplicable.

There is another theory which states that this has already happened.

— from *The Restaurant at the End of the Universe* by D. Adams

Dedicated to

Marzia and Lucrezia

Chapter 1

Introduction

The word *cosmology* comes from the Greek words *kosmos* (world) and *-logia* (study of), so it is the study of our world (the Universe) from its origin to its final fate. Dealing with the whole Universe means asking fundamental questions such as "Where do we come from? What are we made of? Where are we going?". These questions have always intrigued mankind and many ancient philosophers have tried to answer them. With the progress in mathematics and physics, and thanks also to technological achievements in computation and observations, cosmology has evolved from mere speculative philosophy to a solid scientific discipline. However, the central methodology remains: to search for answers we need to look at the sky.

The birth of modern cosmology is generally associated with the year 1917, when Albert Einstein realised that his theory of general relativity could be used to construct a self-consistent cosmological model [6–8]. Einstein himself recognised that the solutions of his equations pointed to an evolving universe and, believing in a static one, he resolved the "problem" by introducing a cosmological constant, the repulsive force of which would counteract the attractive gravitational force. However, Alexander Friedmann in 1922 [9] and Georges Lemaître in 1927 [10] discovered that Einstein's equations could describe a much larger class of dynamical models than those considered by Einstein himself. Indeed, analysing all the homogeneous and isotropic solutions of the field equations, they found that some solutions were char-

acterised by an expansion of the size (as given by the physical distance R between two points in space) of the Universe at cosmic time t. These models included ones which predicted $R = 0$ at $t = 0$, i.e. a singularity at the beginning of time. The Universe could be not static and eternal, but it could have an origin and, possibly, an end. The observations of a redshift in spectral lines from distant galaxies made by Slipher in 1915 [11] and by Hubble in 1929 [12] were considered as the first evidence in favour of the evolution of the Universe from a singularity at $t = 0$ (see e.g. [13, 14] for historical reviews on modern cosmology).

1.1 The history of our Universe

In this section we review the currently most widely-accepted theory of the Universe, the standard cosmological paradigm. This model predicts that after the singularity, during the very early Universe, there is a nearly-exponential expansion, called *inflation* [15–18]. In the simplest slow-roll class of models, the inflationary stage is driven by a scalar field ϕ (the so-called *inflaton*) slowly descending a nearly flat and smooth potential, $V(\phi)$. The field energy density is then dominated by the potential energy and the inflaton has a negative pressure, which induces an accelerated expansion of the Universe in Einstein's general relativity framework (see e.g. [19, 20]). Interestingly, due to the quantum nature of our world, the inflaton field is also characterised by quantum fluctuations [21–25]. Since the Universe is exponentially expanding during inflation, the wavelengths of the fluctuations are exponentially stretched, so that the fluctuation amplitudes do not cancel out between each other (as is the case in a flat space-time) but survive as small inhomogeneities, $\delta\phi$, of the inflaton field ϕ. In the standard slow-roll, the spectrum of these primordial perturbations is predicted to be nearly scale invariant, $\mathcal{P}^{\rm prim}(k) \sim k^{n-1}$ with $n \sim 1$, which is confirmed by the results at large scales e.g. from *cosmic microwave background* (or CMB, see below the definition) anisotropies [26–28] (e.g. the Planck experiment gives $n = 0.965 \pm 0.004$ [28]). This mechanism of producing perturbations is the

currently most-favoured theory for the origin of structure in the Universe (see e.g. the reviews [29–31]). The tiny inhomogeneities in the inflaton field are transferred to curvature fluctuations in the metric and to perturbations in the matter and radiation density content of the Universe. After inflation (and during the matter domination), matter perturbations will grow via gravitational instability to become the non-linear structures, i.e. galaxies and clusters, we see today.

During the inflation period, the inflaton field continues to descend $V(\phi)$, until it reaches the potential minimum. The inflaton density becomes rapidly dominated by the kinetic energy and eventually the field starts to oscillate around the minimum of $V(\phi)$. The Universe is then dominated by coherent oscillations of the inflaton field, which need to be converted into radiation to start the so-called *hot Big Bang* phase. The mechanism leading to this transition is called *reheating* (see e.g. the classical review [32] for further details).

After reheating, it is believed that the energy density of the Universe is dominated by radiation, and the Universe starts its decelerating expansion. This scenario is dubbed the hot Big Bang model. At this stage the Universe is filled with a tightly-coupled sea of relativistic particles, such as photons, electrons, neutrinos, muons, gluons and quarks. The temperature and density of this thermal bath reduce with the expansion. When the temperature drops below $T \lesssim 150\,\mathrm{MeV}$, gluons and quarks no longer have enough energy to exist separately (the so-called *QCD phase transition* occurs) and are confined inside hadrons: mesons and baryons. The lightest baryons are protons and neutrons, while the lightest mesons are the pions. After muons and pions have annihilated and the temperature has reached $T \sim 1\,\mathrm{MeV}$, the neutrino interaction rate is no longer sufficient to maintain these particles in thermal contact with the photon bath, so they decouple. Eventually, electrons and positrons become non-relativistic, and soon after this transition they annihilate reducing their total abundances. At this stage the Universe is dominated by photons and relativistic neutrinos.

Around 380,000 years after the Big Bang, the Universe is cold enough to enable

the formation of neutral hydrogen from the combination of electrons and protons, the so-called *recombination* period. The Universe then becomes transparent to photons, that decouple from the primordial bath and are free to stream in space. This radiation will travel from this point in time to the present, redshifting to microwave frequencies as the Universe expands. Due to their isotropic and homogeneous distribution in the sky, these photons (decoupled from the primordial plasma) are the CMB radiation (mentioned above) and they carry valuable information about the primordial Universe. Indeed, CMB observations have been used in the last two decades to paint a very detailed picture of the early Universe. In particular, the small temperature fluctuations ($\delta T/T \sim 10^{-5}$, which are believed to be seeded by the quantum fluctuations in inflation as mentioned above) in the CMB, in combination with large scale structure and type Ia supernovae observations, have been used to constrain the cosmological parameters with high precision [26–28].

1.1.1 Cold dark matter

In the above section, we have sketched the evolution of the Universe after inflation up to recombination. All the particles considered there are within the framework of the standard model (SM) of elementary particles. However, to describe the later stages of the evolution of the Universe, we need to first introduce another fundamental ingredient, whose "dark and stable" nature can explain gravitational effects that fail to be addressed relying on baryons only. This is commonly called *dark matter* (DM), which, according to the current standard cosmological model, is something beyond the SM theory of particles.

Several observations point towards the so-called *missing mass* on cosmological and astrophysical scales[1] (there is more mass than expected from a universe made of baryons only), e.g. flat rotational curves in galaxies, measurements of velocity dispersions and gravitational lensing in clusters of galaxies, CMB anisotropies and

[1]There are attempts to solve this problem without invoking dark matter, but relying on modifications of standard gravity, e.g. MOND [35] or the recent emergent gravity [36].

so on (see e.g. [33, 34] for recent reviews). For example, the analysis of the CMB anisotropies tells us that around 30% of the total energy density today is in some form of matter, of which only 5% of the matter density is in the form of baryons, meaning that the majority of the matter content should be of non-baryonic nature [27, 28]. Another simple argument (taken from [34]) in favour of dark matter as non-baryonic particles can be made by considering the evolution of the density perturbations. We know that the baryons are strongly coupled to the photons before recombination (see above), which takes place at $z_{\rm rec} \sim 1000$. For this reason, baryon matter density perturbations are of the same order of photon density perturbations ($\delta\rho/\rho \sim 10^{-5}$) at $z \sim z_{\rm rec}$ and they start to grow after baryons decouple from photons. At the linear order in perturbation theory and in the matter domination period, the growth of matter perturbations is proportional to the scale factor $a = 1/(1+z)$. If baryons were the only matter content of the Universe, we would expect that the matter perturbations today ($z = 0$) would be of the order of

$$\left.\frac{\delta\rho}{\rho}\right|_{z=0} = (1+z_{\rm rec}) \left.\frac{\delta\rho}{\rho}\right|_{z=z_{\rm rec}} \sim 10^{-2}, \tag{1.1.1}$$

which means that they would still be in linear regime (i.e. $\delta\rho/\rho \ll 1$) today. However, since we observe galaxies and clusters (and galaxies are observed out to high redshift), we know that by the present time perturbations on those scales have long entered the non-linear regime, $\delta\rho/\rho > 1$, and this implies that baryons alone cannot build up the structure we see today. Indeed, to solve the above issue, we need a non-baryonic matter fluid whose perturbations have started to grow earlier than recombination (i.e. at $z > z_{\rm rec}$), such that they are in the non-linear regime today. One interesting property that follows from the above argument is that dark matter needs to be decoupled from photons before recombination. The DM particles should also be long-lived in order to not decay into radiation during the expansion of the Universe.

In the standard cosmological model, we also add the adjective "cold" to the DM particles with the meaning that the DM behaves as a pressure-less fluid in the linear

regime and at cosmological and astrophysical scales[2]. A class of cold dark matter particles generally considered in the literature is that of weakly-interacting massive particles (WIMPs, see e.g. [37]) with a mass of a few GeV and negligible thermal velocities.

Before recombination, the Universe becomes dark matter dominated and the small matter density perturbations ($\delta\rho_{\rm m}/\rho_{\rm m}$) begin to grow under gravitational instability. Indeed, regions of space in which the density is slightly higher than the mean density of the Universe (over-dense regions) start to attract matter from the surroundings. When the perturbation is still in linear regime ($\delta\rho_{\rm m}/\rho_{\rm m} \ll 1$), the physical size of the over-density region increases as the Universe expands. However, once a perturbation reaches an overdensity of order of unity ($\delta\rho_{\rm m}/\rho_{\rm m} \sim 1$), it decouples from the background expansion, collapses and reaches a dynamical state near virial equilibrium, i.e. becomes a self-gravitating dark matter object called *halo* (see e.g. [30, 38–41] for reviews on this subject). Haloes increase in mass and size either by dragging material from the surrounding environment or by merging with other haloes. The matter distribution inside a halo is, in general, not smooth, and the halo is characterised by a number of self-bound sub-structures (the so-called *subhaloes*) within its virial radius.

1.1.2 Late acceleration and Λ

As mentioned above, the nature of dark matter is beyond the current standard model of fundamental particle physics. However, this is not the only "issue" within the standard cosmological paradigm that potentially requires the introduction of a "dark" sector in order to match observations. Indeed, in the late 1990s, observations of Type Ia supernovae at redshift $z > 1$ by two teams, the Supernova Cosmology Project Collaboration [42, 43] and Supernova Search Team [44, 45], in combination with the extant CMB measurements, led to the discovery of the late-time accelerating

[2]This does not mean that the DM is truly pressure-less. Pressure-like effects appear at such small scales that are not cosmologically relevant.

expansion of the Universe. However, a universe consisting of matter and radiation cannot explain such an acceleration of the expansion rate.

This has raised the still-open question of what is the nature of this component (the so-called *dark energy*) that dominates the energy content of the Universe today (around 70% of the total energy density today is in dark energy). A simple solution to this problem involves the (re)introduction of Einstein's *cosmological constant*, Λ. We recall that a cosmological constant was first introduced by Einstein to produce a static universe. However, in this case the constant serves another purpose, i.e. to obtain a late-time accelerating expansion of the Universe in line with the observations.

Dark matter and the cosmological constant Λ account for almost all the energy density of the Universe today and, for this reason, the standard cosmological model is now referred to as the Λ cold dark matter model or ΛCDM. Therefore, considering what we said above about the primordial fluctuations from inflation, the ΛCDM paradigm is characterised by three assumptions:

- a nearly scale-invariant primordial curvature power spectrum,
- cold and non-interacting dark matter particles (i.e. treating the DM as a pressure-less fluid) and
- a cosmological constant Λ.

These assumptions (in particular the first two) imply that matter density fluctuations are non-vanishing on all (astrophysically- and cosmologically-relevant) scales [19, 20, 37, 40, 41]. This has interesting implications for structure formation. Indeed, in ΛCDM structures build up hierarchically, i.e. small objects form first and then merge together to create larger haloes. Numerical simulations of hierarchical structure formation are remarkably in line with observations of large-scale clustering of galaxies [40, 41, 46–51], and the ΛCDM paradigm has successfully passed almost all observational tests on large scales available today.

1.2 Alternatives to ΛCDM

Despite the success of the ΛCDM paradigm, the true nature of dark matter and dark energy remain a mystery. Moreover, several studies have suggested tensions between pure CDM predictions and observations on galactic and sub-galactic scales (the so-called *small scale controversies*, for a recent review see [52]). In the subsections below, we review these challenges and describe some alternative models to ΛCDM that have been proposed in the literature to address these problems. Although these models do not resolve all the issues with the standard paradigm, they introduce variations in the large scale structure that can be used to test the validity of ΛCDM at different scales.

1.2.1 Damped matter fluctuations on small scales

CDM haloes display central density cusps in N-body simulations [53–55]. Such profiles are strongly excluded by the observed small scale dynamics of some spiral galaxies, which in turn seem to prefer a constant DM distribution (core) in the center [56, 57].

The *missing satellites* problem is another small scale issue. This refers to the large difference between the number of satellite galaxies observed in Milky Way-like galaxies and the number of subhaloes in ΛCDM simulations [58, 59]. It is unclear if this problem is really due to an absence of small structures or rather that these structures are "dark" haloes which contain no visible galaxies and hence are not detectable directly. Several solutions have been proposed to ameliorate these shortcomings of the ΛCDM paradigm, e.g. by taking into account baryonic physics [60–63]. The absence of massive subhaloes in the Milky Way could also be interpreted as an indication that the MW halo is less massive than is commonly assumed [64]. In any case, the observed lack of small structures implies that galaxy formation takes place in the most massive MW subhaloes, but when we look at these structures they appear less dense than expected in CDM simulations. This is the

so-called "too big to fail" problem, first identified by [65], although this issue can also be resolved by invoking baryonic physics [63].

These possible difficulties facing the standard ΛCDM paradigm have renewed interest in alternative cosmological scenarios that display less power on small-scales. Such damped matter fluctuations can be achieved by relaxing one of the first two above assumptions (see bullet points at the end of Section 1.1.2) in the standard paradigm. We can then divide the models with damped matter fluctuations (*damped models* hereafter) into two broad classes: those involving modifications to the primordial power spectrum (e.g. broken scale invariance during inflation, which we dub *non-standard inflation* models) [66–74] and those that suppress power at later times through some non-standard DM mechanisms (these models are generally referred to as *non-cold dark matter* or nCDM, see e.g. [75]) [76–96].

Non-standard inflation models are characterised by a suppression in the primordial curvature power spectrum on small scales, while the DM sector remains the same as in the standard paradigm (in these models the DM particles are still cold and non-interacting). A suppression in the curvature power spectrum can be achieved e.g. when the first derivative of the inflaton potential (in one-field inflation models) has a discontinuity [66, 72, 74] or when a second inflationary stage is introduced (as in models of thermal inflation [73]). Because of the coupling between matter and gravity, damped curvature fluctuations induce damped DM perturbations (i.e. in these non-standard inflation models a cut-off appears in the matter power spectrum at small scales).

nCDM models introduce non-standard DM mechanisms that modify the shape of the power spectrum during the evolution of the fluctuations in the radiation and matter dominated epochs, while the primordial power spectrum remains scale-invariant. The mechanism leading to a suppression of power in nCDM depends on the particular particle production process. Nevertheless, nCDM candidates are often characterized either by a non-negligible thermal velocity dispersion (the so-called *warm dark matter* models or WDM [76–89]), interactions (DM interacting with

standard model particles such as neutrinos or photons [90–92] and self-interacting DM [93]) or pressure terms from macroscopic wave-like behaviour (e.g. ultra-light axions [94–96]).

All these features introduce a characteristic scale below which the density fluctuations are erased. Independently of whether these models can give better matches to the observations than ΛCDM on small scales, it is interesting to find how structure grows in such alternatives. Indeed, testing variations from ΛCDM can help us to understand how much we can learn about the nature of dark matter and of the mechanisms (such as inflation) that occurred in the early Universe by measuring cosmic large-scale structure.

1.2.2 Modifications of general relativity

From the theoretical point of view, one of the biggest challenges faced by ΛCDM is related to the assumption that the late acceleration of the Universe is driven by a constant vacuum energy Λ. Indeed, the observed value of Λ, inferred from cosmology, is smaller than the expected ground state energy density of the vacuum predicted in quantum field theory by $50 \sim 60$ orders of magnitude [97, 98]. A fine-tuning mechanism is then needed to reconcile these two values, that, at the moment, is not provided in the framework of the standard model of particles or in its extensions (e.g. supersymmetric models). This is referred to as the *fine-tuning* problem. Moreover, the present value of the cosmological constant energy density is of the same order of magnitude of the mean matter density in the Universe today; given that these two densities evolve differently at earlier times, this coincidence is another potential theoretical issue generally called the *coincidence* problem.

Alternative scenarios that extend general relativity (GR) (the so-called *modified gravity* (MG) models) are generally not able to resolve the above-mentioned problems concerning the cosmological constant. However, these models are interesting because the most stringent tests for GR come from our solar system, while conclusive evidence that GR is valid on much larger scales is still missing. Future surveys such as

DESI [99,100], EUCLID [101] or SKA [102] (as we will see in this thesis) will be able to test gravity on cosmological scales, potentially finding or ruling out deviations from the standard paradigm.

There is a huge number of ways to modify GR (for reviews see e.g. [103, 104]), and, depending on the model chosen, non-standard features can be introduced in the background history and/or in the clustering of structure of the Universe. Analysing the theoretical predictions of these models helps us to identify cosmological observables that can potentially uncover any departures from GR. Here, we focus on the class of *chameleon* $f(R)$ gravity models [105, 106], in the popular variant proposed in [107], which can be constructed to reproduce the expansion history of a ΛCDM universe accurately. So, the main differences in chameleon $f(R)$ with respect to GR can be found in the formation and clustering of non-linear structures rather than in the background evolution.

1.3 Cosmological tools

In the era of precision cosmology, numerical simulations play a crucial role in helping us to understand how the initially small matter perturbations grow to become non-linear structures in the standard ΛCDM model and its alternatives. In this thesis, we run our N-body simulations in the case of damped models (Chapter 2-5), while we use the results from chameleon $f(R)$ gravity hydrodynamical simulations [108] to assess the effects of MG on the spacial distribution of neutral hydrogen and the 21-cm physics.

1.3.1 N-body simulations

N-body simulations follow the evolution of a patch of the Universe, by sampling the DM phase-space density via a finite number of N tracer (or simulation) particles [109]. The positions and velocities of these particles are obtained by solving the Newtonian equations of motion, embedded in an expanding (background) Universe. For DM-only

simulations, the interactions between the simulation particles occur only through gravity.

The first step to run a N-body simulation is to transfer the information about the small matter inhomogeneities, $\delta\rho_{\rm m}$, at some time t (information contained in the matter power spectrum, $P(k) \sim \langle|\delta\rho_{\rm m}(k)|^2\rangle$) to the simulation particles, initially distributed (generally) on a grid. This produces the N-body initial conditions (ICs). In the ICs, the particles are displaced from the initial grid positions and are provided with gravitationally-induced velocities following e.g. the Zel'dovich approximation (first order perturbation theory) [110] or a second-order Lagrangian perturbation theory (2LPT) [111, 112].

In this process, it is important that the Fourier modes of the perturbations at the scales and the redshift at which the ICs are generated are well inside the linear regime, so that the above perturbation theory approximations can be used. The choice of the starting redshift for a given simulation box is of great importance. For our simulation set-ups (as we will see in Chapter 2) we choose to generate the initial conditions at $z = 199$, using 2LPTic [112], which provides ICs based on 2LPT. We test the impact this choice of initial redshift has on our results (see Chapter 2). We then evolve the ICs using the publicly-available N-body and hydrodynamical simulation code Gadget-2 [113]. The Gadget-2 code calculates the gravitational forces between the simulation particles using a tree algorithm for short-range forces and a high-resolution particle-mesh for computing long-range forces. The results from N-body simulations are used to measure halo statistics and non-linear matter and velocity power spectra that give information on the non-linear clustering and distribution of the DM in the simulated Universe. The different N-body simulation set-ups (number of particles, box volume, etc) used in this work are described in more detail in the next Chapters.

1.3.2 Hydrodynamical simulations

N-body simulations trace the growth of DM structure into the non-linear regime. The DM, in the standard picture, is believed to be decoupled from the rest of the Universe, interacting only via gravity. Although DM accounts for the majority of the matter content of the Universe, in order to compare simulations with observations, we need to take into account baryonic physics, that is responsible for the galaxies that form within the DM structures. In a DM halo, the baryonic gas cools while descending the DM potential well [114]. Depending on the temperature and density, a variety of cooling processes can affect the gas (see e.g. [39, 115]). Eventually, its self-gravitational force dominates over the DM one, and the gas collapses under its own gravitational pull. The temperature and density of the gas rises and this self-gravitating cloud may fragment into small, high-density cores, producing stars [39]. However, supernovae and active galactic nuclei (AGN) feedback reduce the star-formation efficiency, by heating the surrounding gas, suppling it with momentum and removing it from the galaxy (in what is called a *galactic wind*). The energy of the AGN can also be dumped into the hot gas to balance the cooling flow, hence stopping the gas from cooling in the first place (the so-called *radio mode feedback*). As is clear from the above sketch, galaxy formation involves many interconnected processes that can modify the abundance of the main baryonic components (hot gas, cold gas, stars and a supermassive black hole) in a galaxy. Therefore, simulations of DM+baryon dynamics (or *hydrodynamical* simulations) are more computationally-expensive than DM-only simulations (where particles interact only via gravity), because they need to take into account of all these different effects that influence galaxy formation and evolution (for a review see e.g. [116]).

To model the baryonic physics in MG scenarios, we use the SHYBONE simulations [108], a set of very high-resolution full-physics hydrodynamical simulations in $f(R)$-gravity carried out with the AREPO simulation code [117] (this code is based on P-Gadget3, a version of the code Gadget2 [113]). The simulations use the Illustris-TNG hydrodynamical model [118–123] incorporating prescriptions for star and black hole

formation and feedback, gas cooling, galactic winds and magneto-hydrodynamics on a moving Voronoi mesh[3] [120, 124]. The equations for the modified gravity force in $f(R)$-gravity are solved to full non-linearity in the Newtonian limit by the modified gravity solver in the code [125], capturing the effects of the chameleon screening mechanism (see Chapter 6 for further details). The results from these hydrodynamical simulations are used to measure the neutral hydrogen abundance and power spectrum in the simulated Universe.

1.4 Thesis outline

In this thesis we study the effects of some alternatives to ΛCDM on structure formation using high-resolution cosmological simulations. In Chapter 2 we investigate the impact of adding thermal velocities in N-body simulations in thermal WDM cosmologies. We find that a new source of numerical noise is introduced in the simulations and we quantify the magnitude of this error in the non-linear matter and velocity power spectra and in halo statistics such as the halo mass function, halo radial density profiles and the halo mass-concentration relation. In Chapter 3, considering different power spectra with damped matter fluctuations, we assess up to which scale the information from the linear-theory power spectrum shapes the non-linear evolution and how non-linear quantities such as the power spectrum and the halo mass function are sensitive to variations in the linear power spectrum. We then propose a 2-parameter model for the power spectrum of damped scenarios and test its validity by comparing it with the standard 3-parameter model considered in [75]. Exploiting these results, in Chapter 4, we propose a new smooth-k space filter to be used in the Press-Schechter approach, to analytically estimate the DM halo mass function in models with damped matter fluctuations. We show how our filter resolves some problems of other filters raised in the literature. In Chapter 5 we study

[3]The main differences in the Illustris-TNG hydrodynamical model with respect to other models considered e.g. in Illustris [126,127] (or EAGLE [128]) simulations are in the implementation of an updated AGN feedback model, the choice of the parametrisation for galactic winds and the inclusion of magnetic fields (see e.g. [123] for a more complete comparison with Illustris simulations).

a new model of non-standard inflation that is characterised by an enhancement w.r.t. ΛCDM in the linear-theory power spectrum before a sharp cut-off. We show how the enhancement influences the non-linear power spectra and the halo properties, comparing the results with those expected in the standard ΛCDM and in the thermal WDM model. In Chapter 6, we focus our study on modified gravity theories, using the chameleon $f(R)$ gravity as an example. In this chapter, we model the neutral hydrogen distribution in MG using the hydrodynamical simulations in [108], assessing to what extent the HI and 21-cm power spectrum differ in $f(R)$ gravity theories when compared with results from GR. Finally, a summary of our work and future prospects is given in Chapter 7.

Chapter 2

Thermal velocities and structure formation in WDM

2.1 Introduction

Several nCDM models have been proposed in which candidates have non-negligible thermal velocities [76–89]. The main consequence of the presence of a non-vanishing velocity dispersion is free-streaming: the particles cannot be confined into regions smaller than the free-streaming length, $\lambda_{fs} \sim \sigma/H$, where σ is the particle velocity dispersion, so that density perturbations are damped on scales below λ_{fs} and a cut-off appears in the linear matter power spectrum. The shape of the matter power spectrum and the position of the cut-off depends on the velocity dispersion σ, which in turn depends on the particular velocity distribution of the particles. The free-streaming is a feature which is common in collisionless fluids with non-negligible velocity dispersions, e.g. active neutrinos (see e.g. [129]) exhibit such behaviour[1].

The simplest of these scenarios is the so-called thermal warm dark matter (thermal WDM), where DM particles are in thermal contact with the primordial bath, decouple when still relativistic, and enter the non-relativistic regime deep into

[1]CDM candidates such as WIMPs also display a cut-off in the power spectrum due to free-streaming or to interactions in the early Universe. Since such particles are heavy and interact weakly with Standard Model particles, the suppression scale appears at very small masses (between $10^{-12}\ h^{-1}\mathrm{M}_\odot$ and $10^{-4}\ h^{-1}\mathrm{M}_\odot$ depending on the parameters of the model [130, 131]).

the radiation-dominated period. This mechanism ensures that the particles have a Fermi-Dirac (if the particles are fermions) momentum distribution, which leads to a simple relation between the particle mass and the free-streaming length λ_{fs}, and a distinctive cut-off in the matter power spectrum [76–79]. The Lyman-α forest has proven to be a powerful tool to constrain the mass of the thermal WDM candidates, suggesting a mass of $m_{\rm WDM} \gtrsim 3.3$ keV [132] (although a recent analysis pushes the limit to slightly higher masses $m_{\rm WDM} \gtrsim 3.5$ keV when allowing a particular evolution of the temperature of the IGM, [133]). These constraints on the mass are strictly valid only if all the DM sector is in the form of thermal WDM particles. Mixed scenarios (thermal WDM + CDM) are also possible. In these models only a fraction of the dark matter is in the form of WDM, while the remaining fraction behaves as standard CDM. Such models do not display the sharp cut-off in the power spectrum that is characteristic of a pure WDM model since the CDM fluctuations are present on small scales [134]. Constraints on mixed DM using Lyman-α forest have been found in [134].

keV sterile neutrinos are another class of nCDM candidates with non-vanishing thermal velocities, which are well motivated by particle physics theories (see [135] for a summary of the cosmological impact of these particles). Their mixing with active neutrinos offers a possible mechanism for producing a primordial abundance of such particles. Moreover, sterile neutrinos ν_s produced via mixing can decay radiatively via $\nu_s \to \nu_a + \gamma$, where ν_a is an active neutrino, leading to a monochromatic X-ray line. The mass and the mixing angle of these particles can then be constrained by searching for decay signals in the X-ray spectrum [81, 135]. The production mechanism via mixing can be non-resonant ("Dodelson-Widrow") [80–82] or resonantly ("Shi-Fuller") enhanced by a lepton asymmetry in the early Universe [83–85]. However, a pure non-resonant production mechanism of keV sterile neutrinos is in conflict with the current astrophysical constraints from the Lyman-α and X-rays [132, 135]. Resonantly produced sterile neutrinos are more in line with observations and can potentially explain the recent (although controversial) detection of a 3.55 keV X-

ray emission line [136, 137]. However, such neutrinos are constrained to a very narrow range of masses $7 \leq m_s \leq 36$ keV and lepton asymmetries larger than 15×10^{-6} (at 95% CL) [138], and they are completely disfavoured when including constraints from Lyman-α forest [139]. Another possibility is that keV sterile neutrinos can be produced via the decay of a hypothetical parent particle in the early Universe [86–89]. The initial parent decay production can be followed by a non-resonant production [140]. This case is similar to a mixed DM scenario since there is a colder velocity component (spectrum from decay production) and a warmer velocity component (Dodelson-Widrow production). Sterile neutrinos produced by mixing or by particle decays have non-thermal distributions and cannot be treated in the simple framework of thermal WDM particles. Indeed, in some of these models, the sterile neutrino momentum distribution deviates significantly from Fermi-Dirac, so that, unlike thermal relics, the matter power spectrum cut-off is not a simple function of the mass. Consequently, keV sterile neutrinos can act as warm or cold DM depending on the model thus eluding the $m_{\rm WDM} \gtrsim 3.3$ keV Lyman-α constraint found in [132, 133] (which consider only matter power spectra from thermal WDM distributions). The very specific shape of the matter power spectrum has to be taken into account to constrain each (non-thermal) model using the Lyman-α forest. Another way to constrain non-thermal models using the Lyman-α forest has been proposed in [75].

2.2 Thermal velocities and structure formation

If DM is in the form of nCDM candidates, it is important to investigate how the predictions for structure formation differ in such models from those forecast in standard CDM. N-body simulations have proved to be a powerful tool to follow the evolution of the structure in the CDM scenario and can also be used to study the effects of the damping on small scales in nCDM. However, the difference between nCDM candidates, such as thermal relics or sterile neutrinos, and CDM is not

only in the shape of the linear matter power spectrum, but also in the presence of non-negligible thermal velocities for nCDM. Indeed, in structure formation we can have two sources of DM velocities: those intrinsically due to the thermodynamical distribution of the DM particles and those induced by the gravitational collapse and clustering of structures (gravitationally-induced velocities), see e.g. [134]. When running a simulation of structure formation, the starting redshift is generally chosen to be at a reasonably high value, to ensure that all of the scales we are interested in are well within the linear regime (see discussion in Subsection 1.3.1). If we start at $z = 199$, for a typical simulation the gravitationally-induced velocities (generally called peculiar velocities) are around or below $v_{\rm pec} \sim 10$ km/s. CDM candidates have negligible thermal velocities respect to the peculiar velocities $v_{\rm pec}$ at the redshift considered, and so their thermal velocities can be safely neglected. This is not always the case for nCDM candidates, e.g. for a thermal WDM candidate with mass of 3.3 keV, the thermal velocity dispersion is of the order $\sigma_{\rm therm} \sim 2$ km/s at $z = 199$ [76]. So, thermal velocities are non-negligible and should be taken into account in the simulations. However, numerical simulations of nCDM are usually initialised by taking into account only the cut-off in the linear matter power spectrum, while thermal velocities are not explicitly included (see e.g. [75, 76, 141–147]). This is because thermal velocities are assumed to have no influence on the halo mass function at late times so long as the mass resolution of the N-body simulation at the starting redshift is well above the Jeans mass of the warm particle fluid [143] (if a simulation belongs to this class, we say that the Jeans mass criterion is satisfied). Another argument that is often invoked to justify neglecting thermal velocities in N-body simulations concerns the distance travelled by particles free-streaming due to their thermal motions over the duration of the calculation, which is e.g. around a few kiloparsecs for thermal WDM candidates with masses around a few keV [141]. If this length is smaller than the mean-interparticle separation in the simulation, thermal velocities are neglected since free-streaming only influences scales that are not well resolved in the simulation (if a simulation belongs to this class, we say that the free-

streaming length criterion is satisfied). Anyway, neglecting thermal velocities remains an approximation which we test in this chapter. The only physical effect expected when introducing primordial thermal velocities is a "phase-packing" limit, which prevents the density in the central regions of the haloes from increasing arbitrarily (producing a central core) [148–150], but for values of WDM candidate masses compatible with the upper limits from the Ly-α forest [132,133], the cores are only a few parsecs in size and therefore are not relevant astrophysically [149,150]. However, there are other models in which thermal velocities cannot be easily discarded, e.g. in the case of composite DM simulations, in which there are two DM components (e.g. the simulations of CDM + massive ν discussed in [151–153]). The aim of this chapter is to assess the impact of including thermal velocities in simulations of structure formation in thermal WDM (using the standard technique described below) to see if this affects the range of scales on which the simulation results are accurate.

A common approach used to implement thermal velocities in N-body simulations consists of adding the physical thermal velocities to the gravitationally induced peculiar velocities of the simulation particles in the N-body initial conditions (ICs) [134,149–157]. The subsequent evolution of structure will then follow both sources of the velocity field[2]. This approach is also used in galactic dynamics, where the fluid is made up of stars. In this case it is well known that ignoring the stellar velocity dispersion produces gravitational instability (see e.g. [159]). Simulations of galactic dynamics are performed by adding a stellar velocity, drawn from a distribution, to the simulation particles. However, as pointed out by [151,152,154,155] (see also the discussion in [145,146]), the above approach of adding thermal velocities in the ICs can introduce a new source of numerical error. Indeed, since a simulation particle contains a huge number of physical particles[3], the net thermal velocity has to be zero

[2]A different approach to simulate gravitational evolution of collisionless WDM particles has been recently proposed in [158].

[3]Simulation particles are always many orders of magnitude more massive than physical particles, e.g. in our simulations the simulation particle mass is around $10^7\ h^{-1}\mathrm{M}_\odot$, while the warm particle mass is of the order of keV $\sim 10^{-63}\ h^{-1}\mathrm{M}_\odot$. So each simulation particle is made up of around 10^{70} physical particles.

if the thermal velocities of physical particles are drawn from a distribution without a preferred direction. Extra numerical noise is then introduced because we assign a net (non-zero) thermal velocity (taken from the Fermi-Dirac distribution of physical WDM particles) to each simulation particle. [154] pointed out that the numerical noise can be reduced by choosing a lower ($z \sim 40$) redshift at which to generate the ICs. However, a detailed study of how the noise affects the formation and the evolution of the structures has not been carried out before.

Our aim in this chapter is to perform a comprehensive study of the effects of thermal velocities in N-body simulations for the simplest scenario of thermal WDM where the velocity distribution is Fermi-Dirac[4]. Using the approximation of assigning thermal velocities to the simulation particles, we quantify the impact of the numerical noise by analysing the matter and velocity power spectra measured from simulations at different redshifts. We also show how these numerical artefacts can affect halo properties such as the halo mass function and radial density profiles. In particular, we derive a new mass cut-off below which spurious haloes dominate in simulations with thermal velocities. Note also that the non-thermal production of sterile neutrinos produces, in general, colder velocity spectra than thermal WDM. For this reason, our results can be considered as an upper bound on the impact of thermal velocities in sterile neutrino models.

The layout of this chapter is organised as follows. In Section 2.3, we measure velocity power spectra for ICs generated at $z = 199$ for WDM simulations, quantifying the source of the noise introduced by the thermal velocities in the initial conditions. We run a series of WDM simulations with thermal velocities varying the number of particles, box size and the physical WDM particle mass, in all cases extracting velocity power spectra and comparing with WDM simulations without

[4]We stress here the fact that our simulations of thermal WDM satisfy both the Jeans mass [143] and the free-streaming length criteria [141], so, in principle, we can also apply the approximation of neglecting thermal velocities. However, since we are interested in quantifying the effects of the noise introduced in the simulations when adding thermal velocities, we will take into account thermal velocities with the justification that at the initial high redshift, $z_{\rm ini} = 199$, at which the ICs are generated, thermal velocities are comparable with peculiar ones.

thermal velocities. Section 2.4 is devoted to the evolution of the ICs at $z = 199$ up to $z = 0$, showing how the noise in the ICs propagates through to subsequent times. We also discuss the possibility of reducing the numerical noise by generating the ICs at a lower redshift, $z = 39$. In Section 2.5, we explore how haloes are affected by thermal velocities, focusing on the halo mass function and radial density profiles of haloes.

2.3 Thermal velocities and initial conditions

This section explores the impact of thermal velocities in the N-body initial conditions. First, we introduce the WDM model chosen for our analysis. Then, we describe how we generated N-body initial conditions for such a model. Finally, we measure velocity power spectra from simulations which include thermal velocities and compare the results with simulations which ignore thermal velocities.

2.3.1 The thermal WDM model

We choose for our analysis the so-called thermal WDM scenario. In this model, a non-standard fermionic species with mass $m_{\rm WDM}$ is in thermal contact with the primordial bath, decouples when still relativistic and enters the non-relativistic regime deep into the radiation-dominated period [76, 78]. Since this component freezes-out when relativistic and in thermal contact, the functional form of the momentum distribution remains Fermi-Dirac after decoupling,

$$f_{\rm WDM}(p) = \frac{1}{e^{p/T_{\rm WDM}} + 1}, \tag{2.3.1}$$

where the momenta p redshift as $(1 + z)$. $T_{\rm WDM}$ is the temperature of the WDM species and its present value can be related to the so-called present neutrino temperature $T^0_\nu = (4/11)^{1/3}\, T^0_\gamma$ (where T^0_γ is the present photon temperature, note that T^0_ν actually represents the temperature that active neutrinos would have if still in the

relativistic regime today) as [78],

$$T^0_{\rm WDM} = \left(\frac{\Omega^0_{\rm WDM}\, h^2}{m_{\rm WDM}/94\,{\rm eV}}\right)^{1/3} T^0_\nu,$$

where $\Omega^0_{\rm WDM}$ is the present day fractional contribution of WDM in units of the total (critical) density of the Universe $\rho^0_c \equiv 3H_0^2/8\pi G$ and $h \equiv H_0/(100$ km/s/Mpc) is the dimensionless value of the Hubble constant. We make the extra assumption that all the DM sector is in form of WDM, i.e. $\Omega^0_{\rm WDM} = \Omega^0_{\rm m} \sim 0.3$, where $\Omega^0_{\rm m}$ is the present day total contribution of the DM in units of the critical density. When WDM particles become non-relativistic, their thermal velocities remain a Fermi-Dirac distribution with rms velocity of the form [76],

$$\sigma_{\rm therm} \equiv \sqrt{\langle v^2_{\rm therm}\rangle} = 0.0429 \left(\frac{\Omega^0_{\rm WDM}}{0.3}\right)^{1/3} \left(\frac{h}{0.7}\right)^{2/3} \left(\frac{\rm keV}{m_{\rm WDM}}\right)^{4/3} (1+z)\ \ {\rm km/s}. \tag{2.3.2}$$

For the model discussed in this section, a parametrisation of the linear power spectrum of density fluctuations exists [76], which we will use throughout. This parametrisation can be written in terms of a transfer function relative to CDM, $T^2(k) \equiv P^{\rm WDM}(k)/P^{\rm CDM}(k)$:

$$T(k) = \left(1 + (\alpha k)^\beta\right)^\gamma, \tag{2.3.3}$$

where

$$\alpha = a \left(\frac{\Omega^0_{\rm WDM}}{0.25}\right)^b \left(\frac{h}{0.7}\right)^c \left(\frac{m_{\rm WDM}}{\rm keV}\right)^d, \quad \beta = 2\nu, \quad \gamma = -5/\nu, \tag{2.3.4}$$

and

$$a = 0.049, \quad b = 0.11, \quad c = 1.22, \quad d = -1.11, \quad \nu = 1.12,$$

as computed in [79]. More accurate power spectra for more general non-cold DM models can be generated using Boltzmann codes such as CLASS [160, 161].

The characteristic scale at which the cut-off in the WDM power spectra occurs can be defined through the half-mode wavenumber $k_{1/2}$. $k_{1/2}$ is the wavenumber at which the transfer function $T(k)$ falls to 50%. Given the parametrisation in Eq.

(2.3.3) for $T(k)$, we have

$$k_{1/2} = \frac{1}{\alpha}\left(2^{\nu/5} - 1\right)^{1/2\nu}. \tag{2.3.5}$$

2.3.2 The mass of the WDM candidates

Thermal WDM with a particle mass around a keV has a free-streaming characteristic length of the order of dwarf galaxy scales, so candidates with such masses can be able to solve the missing satellite problem [76–79]. The current strongest constraints on the free-streaming length of DM particles come from the Lyman-α forest. The Lyman-α forest is a series of absorption lines in the spectra of distant quasars due to the inhomogeneous distribution of the intergalactic medium (IGM). These lines can be used as a measure of the matter power spectrum on scales $0.5\,h^{-1}\text{Mpc} < \lambda < 100\ h^{-1}\text{Mpc}$ over a range of redshifts $2 < z < 6$ [79,132,133]. In [132] the authors find the following constraints[5] on thermal WDM using the Lyman-α forest, $m_{\text{WDM}} \gtrsim 3.3$ keV. However, the Lyman-α forest does not probe directly the DM power spectrum, but rather that of the neutral hydrogen. The neutral hydrogen gas does not necessarily follow the distribution of DM, since the process of reionisation heats the hydrogen, preventing it from clustering at small scales [162]. To translate the results from the Lyman-α forest to constraints on the DM power spectrum, a crucial parameter is the temperature of the IGM. However, the IGM temperature is not precisely known, so some approximations are made in the literature, depending on which the constraints on WDM particle mass can vary. Indeed, the $m_{\text{WDM}} \gtrsim 3.3$ keV mass bound can be relaxed to $m_{\text{WDM}} \gtrsim 2$ keV by changing the assumptions about the IGM thermal history [132] (see also [163], in which the authors have re-analysed the Lyman-α forest spectra considered in [132]). Motivated by the above discussion, whilst the assumptions about the thermal history of the IGM remain controversial, we choose three benchmark values for the WDM particle mass in our analysis: $m_{\text{WDM}} = 2$ keV, $m_{\text{WDM}} = 3.3$ keV and $m_{\text{WDM}} = 7$ keV (which will be our coldest WDM candidate).

[5] A recent analysis pushes the limit to slightly higher masses, indeed, depending on the thermal history of the IGM, we can have $m_{\text{WDM}} \gtrsim 3.5$ keV [133].

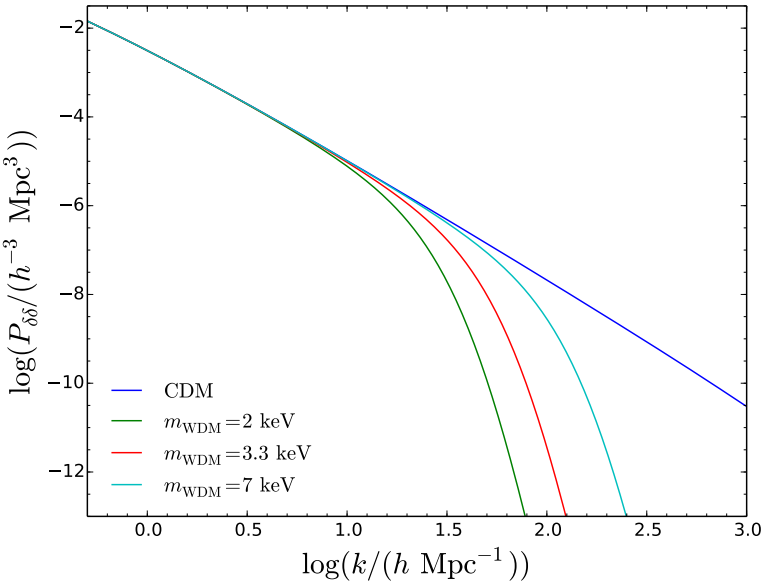

(a)

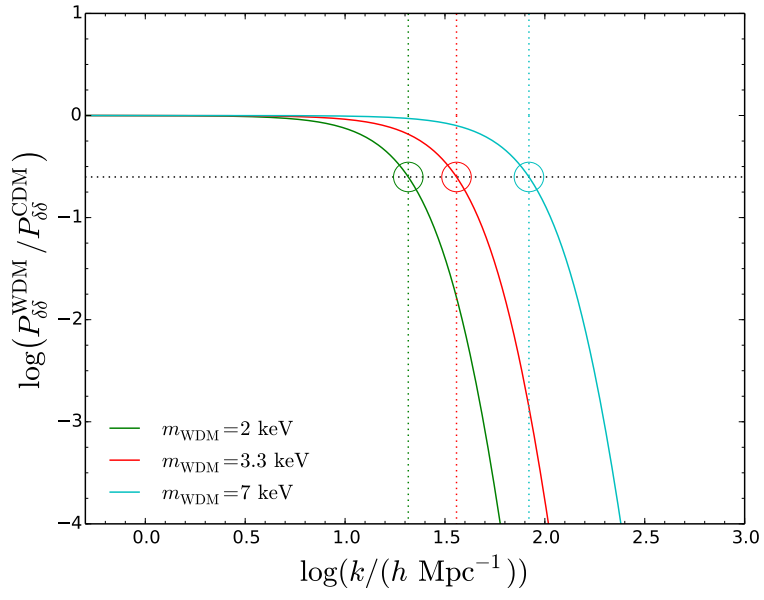

(b)

Figure 2.1: (a) Linear theory matter power spectra at redshift $z = 199$ for CDM and three WDM models with masses $m_{\mathrm{WDM}} = 2, 3.3, 7$ keV as labelled. (b) Squared transfer functions $T^2(k) \equiv P^{\mathrm{WDM}}/P^{\mathrm{CDM}}(k)$ for the three warm candidates. The dotted black horizontal line represents the scale at which the transfer function is suppressed by a factor of two. The intersection between the transfer function and the horizontal line defines the half-mode wavenumber $k_{1/2}$. The WDM spectra are generated using the parametrisation in Eq. (2.3.3).

In Figure 2.1(a), we plot the linear matter power spectra using the parametrisation in Eq. (2.3.3) for the three WDM masses chosen. The CDM power spectrum is also shown for comparison[6]. In Figure 2.1(b) we plot the square of the transfer function $T(k)$, together with the half-mode wavenumber $k_{1/2}$ (see Eq. (2.3.5)) for each of the WDM candidates.

2.3.3 The simulations

In order to take into account thermal velocities in the N-body simulations, the initial conditions (ICs) for running cosmological simulations have to be modified accordingly. We use the numerical code 2LPTic [112]. 2LPTic can generate the ICs for thermal WDM models, taking as input the thermal WDM mass $m_{\rm WDM}$ and computing the corresponding $T(k)$ from Eq. (2.3.3). The code also contains a module for adding thermal velocities, following the approximation used in [134, 149–157]. The thermal velocities for simulation particles are randomly picked such that their magnitudes obey a Fermi-Dirac distribution with a dispersion given by Eq. (2.3.2), while the directions satisfy a uniform distribution in the 4π solid angle. The addition of thermal velocities to peculiar velocities is done using a simple velocity addition law.

We run 2LPTic for the three WDM candidate masses mentioned above, $m_{\rm WDM} = 2, 3.3, 7$ keV. For each mass, we consider two types of WDM simulations, (i) WDM simulations without thermal velocities (which we call WDM-novth) and (ii) WDM simulations which take into account thermal velocities in the ICs (referred to as WDM-vth). Our analysis consists of generating ICs for these two types of simulations, varying the number of simulation particles N and the length of the box L. For each pair $\{N, L\}$, the Nyquist frequency of a simulation is $k_{Ny} \equiv \pi(N^{1/3}/L)$ (this specifies the value up to which we can trust the $P(k)$ estimate using an FFT and the scale down to which a clustering signal can be imposed due to the mean inter particle

[6]The CDM power spectrum is generated using the code CLASS [160]. The values of the cosmological parameters are given below. The DM contribution is $\Omega_{\rm m}^0 h^2 = 0.120$, the baryonic contribution is $\Omega_{\rm b} h^2 = 0.023$, the dimensionless Hubble constant is $h = 0.6726$, the spectral index of the primordial power spectrum is $n_s = 0.9652$ and the linear rms density fluctuation in a sphere of radius 8 h^{-1}Mpc at $z = 0$ is $\sigma_8 = 0.81$.

$m_{\rm WDM}$ (keV)	L (h^{-1}Mpc)	N	$k_{\rm Ny}$ (h Mpc^{-1})	WDM-novth	WDM-vth	$z_{\rm ini}$	Evolved	ϵ (h^{-1}kpc)
2	2	512^3	803.8	✓	✓	199	×	-
2	25	512^3	64.3	✓	✓	199	✓	1.22
3.3	2	64^3	100.5	✓	✓	199	×	-
3.3	2	128^3	201.0	✓	✓	199	×	-
3.3	2	256^3	401.9	✓	✓	199	×	-
3.3	2	512^3	803.8	✓	✓	199	×	-
3.3	10	512^3	160.8	✓	✓	199	×	-
3.3	25	512^3	64.3	✓	✓	199	✓	1.22
3.3	50	512^3	32.2	✓	✓	199	×	-
3.3	25	512^3	64.3	✓	✓	39	✓	1.22
7	2	512^3	803.8	✓	✓	199	×	-
7	12	512^3	134.0	✓	✓	199	✓	0.58
7	25	512^3	64.3	✓	✓	199	✓	1.22

Table 2.1: Summary of the simulations performed. $m_{\rm WDM}$ is the physical mass of the WDM candidate. L and N are the simulation box length and the number of simulation particles respectively. $k_{\rm Ny}$ is the Nyquist frequency. WDM-novth refers to simulations which ignore thermal velocities, while WDM-vth refers to simulations which include thermal velocities. $z_{\rm ini}$ is the redshift at which the ICs are generated. The checkmarks (✓) in the column "Evolved" indicate the simulations which have been evolved up to $z = 0$. For the ICs which have been evolved, we also show the gravitational softening length ϵ. Note that for $L = 25\,h\,{\rm Mpc}^{-1}$, the modes at the smallest wavenumbers probed by the simulations have entered the non-linear regime at $z = 0$. However this does not affect the results presented in this Chapter because (i) the CDM and WDM models (considered here) have identical linear power spectra at small wavenumbers and (ii) we are interested only in the ratio of power spectra between models (so this issue concerning small wavenumbers divides out when considering the ratios).

separation).

The ICs are generated at the initial redshift $z_{\rm ini} = 199$, when the thermal velocity dispersions are, see Eq. (2.3.2),

$$\sigma_{\rm therm} \simeq 3.4\,{\rm km/s} \quad \text{for} \;\; m_{\rm WDM} = 2\,{\rm keV},$$

$$\sigma_{\rm therm} \simeq 1.7\,{\rm km/s} \quad \text{for} \;\; m_{\rm WDM} = 3.3\,{\rm keV},$$

$$\sigma_{\rm therm} \simeq 0.6\,{\rm km/s} \quad \text{for} \;\; m_{\rm WDM} = 7\,{\rm keV}.$$

These are non-negligible with respect to the peculiar velocities, which are of the order of $v_{\rm pec} \sim 10$ km/s at $z = 199$. We have run an additional simulation with a lower initial redshift $z_{\rm ini} = 39$ to test the impact of the initial redshift on the results; we postpone a discussion of this to Section 2.4. In Section 2.4 we have also evolved some of the ICs up to $z = 0$, using the code Gadget-2 [113]. The gravitational

softening length ϵ is set to be 1/40-th of the mean interparticle separation, $L/N^{1/3}$. Further details of our simulations are listed in Table 2.1.

2.3.4 Velocity power spectra measurement

In order to quantify the effects of thermal velocities in WDM-vth, we measure the matter and velocity power spectra from the simulations. However, because in the initial conditions thermal velocities are implemented only in the velocity sector, by default the matter perturbations in the initial conditions are not affected. Instead, the effect of thermal velocities on the matter distribution only becomes apparent after at the first time step and through the subsequent evolution. As in this section we are interested only in the ICs, we shall focus on the velocity power spectra extracted from the ICs. The velocity (divergence) power spectra are defined as [164],

$$P_{\theta\theta}(z,k) = \frac{1}{(a(z)H(z)f(z))^2}\left\langle \theta^2_{\vec{k}}(z)\right\rangle, \tag{2.3.6}$$

where $\theta_{\vec{k}}(z)$ is the Fourier transform of the velocity divergence $\theta(\vec{x},z) \equiv \vec{\nabla}\cdot\vec{v}(\vec{x},z)$ and $f(z) = d\ln D_+/d\ln a$, with D_+ linear growth factor and a scale factor. Remember that the matter power spectrum is

$$P_{\delta\delta}(z,k) \equiv \left\langle \delta^2_{\vec{k}}(z)\right\rangle, \tag{2.3.7}$$

where $\delta \equiv \delta\rho/\bar{\rho}$ is the matter overdensity. So the normalisation in Eq. (2.3.6) is useful since in the linear regime $\theta = -aHf\delta$ and the velocity power spectrum is equal to the matter power spectrum, $P_{\theta\theta} = P_{\delta\delta}$. For this reason, we can compare the velocity power spectra measured from simulations directly with the matter power spectra specified by the fitting formula in Eq. (2.3.3).

Extracting the velocity field from a N-body particle distribution is more challenging than constructing the matter density field, due to the non-additivity of the velocities[7]. Indeed, as pointed out in [164], applying the standard methods used

[7]The non-additivity of the velocities refers to the fact that the net (center-of-mass) velocity of a set of particles is not the sum of the particle velocities $\vec{v}_i$ in the set, but is instead the mass-weighted average, $\vec{v}_{\rm net} = \sum_i w_i\vec{v}_i$, with $w_i = m_i/M$, where m_i is the mass of the i-th particle and

to estimate matter power spectra will not always give the expected results when we consider velocity power spectra. This is mainly because the standard methods usually use a grid-based scheme, in which the simulation box is covered by a grid. At each vertex a value for the matter density (or momentum density), is calculated using some mass assignment scheme (e.g. nearest grid point, cloud in cell, triangular shaped cloud), in the form of a weighted sum of the masses (or momenta) of the particles near each grid vertex (see e.g. [165]). Usually, the velocity field is obtained by averaging the particle velocities near each corresponding grid vertex. Thus, in order to assign a velocity field value at each vertex, we need first to assign the momenta and then divide it by the mass density at the same vertex. The limitation of the method is clearly due to the 0/0 divergence caused by empty grid cells, in which there could be no particles at all and then the momenta and mass density both add to zero.

As suggested in [164], an alternative way to measure the velocity power spectra is to use the Delaunay Tessellation methodology [166]. The Delaunay Tessellation for a set of points p distributed in a 3D space is the set of tetrahedrons (where each vertex is a point of the set) whose circumscribed sphere contains no points other than the four that generate the tetrahedron (and that lie on its surface). This construction is unique. The velocity at the general coordinate $\vec{r} = (x, y, z)$ inside a tetrahedron can then be inferred using a linear interpolation between the velocity values at the 4 vertices of the tetrahedron. In this case when we split the box into cells, we avoid the singularities, since the cell will be contained in at least one tetrahedron. The velocity associated with each grid vertex is computed as the average (in volume) given by all Delaunay tetrahedra contained in the grid cell corresponding to such a point [164]. In this way, the only way to have zero velocity field in a given grid point is a zero mean among all the tetrahedrons contained within the corresponding cell. Throughout we will use the publicly available DTFE code to estimate velocity power spectra, which implements the Delaunay tessellation approach [167].

$M = \sum_i m_i$.

2.3.5 Results and discussion

Figure 2.2 shows the velocity power spectra measured from some of the simulations in Table 2.1. In the first panel (Figure 2.2(a)) we show the results for simulations with box length $L = \{50, 25, 10, 2\}$ h^{-1}Mpc, whilst fixing the number of particles at $N = 512^3$ for $m_{\rm WDM} = 3.3$ keV. On one hand, we see that all the velocity power spectra from WDM-novth agree well with the linear theory power spectra. The agreement extends to higher wavenumbers when decreasing the box size as expected since the mean interparticle separation, $L/N^{1/3}$, goes down and consequently $k_{\rm Ny}$ acquires a higher value. On the other hand, the velocity power spectra extracted from WDM-vth deviate strongly from WDM-novth (and from linear theory predictions), and show an upturn at small scales. These deviations are numerical artefacts since they are pushed to higher wavenumbers for smaller boxes.

In Figure 2.2(b), we show the velocity power spectra for simulations with varying number of particles $N = \{64^3, 128^3, 256^3, 512^3\}$ in a fixed box of length $L = 2$ h^{-1}Mpc. As we can see also in this case WDM-vth deviates from WDM-novth at high wavenumbers. These deviations tend to appear at higher wavenumbers for larger N, confirming the previous statement that the deviations are due to numerical noise.

The thermal velocity dispersion depends on the mass of WDM (see Eq. (2.3.2)). So we expect that the impact of thermal velocities on the ICs will vary with $m_{\rm WDM}$. Figure 2.2(c) shows how the behaviour changes by varying $m_{\rm WDM}$, while fixing the number of simulated particles at $N = 512^3$ and the box length at $L = 2$ h^{-1}Mpc. As we can see, increasing the mass (reducing the thermal velocity dispersion) reduces the deviations due to the noise in WDM-vth and shifts the discrepancies to higher wavenumbers. For the most massive candidate ($m_{\rm WDM} = 7$ keV) there is agreement between WDM-vth and WDM-novth up to $k \approx 170$ h/Mpc, while for the lightest mass ($m_{\rm WDM} = 2$ keV) the power spectrum from simulations with thermal velocities starts to disagree at $k \gtrsim 40$ h/Mpc.

The deviations in the simulations with thermal velocities are due to numerical

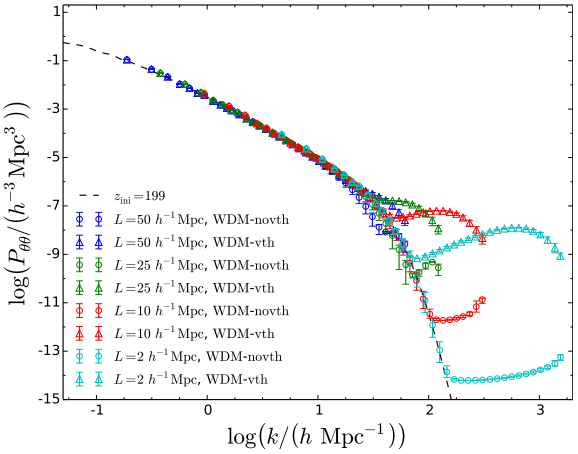

(a) $N = 512^3$, $m_{\rm WDM} = 3.3$ keV. Varying L.

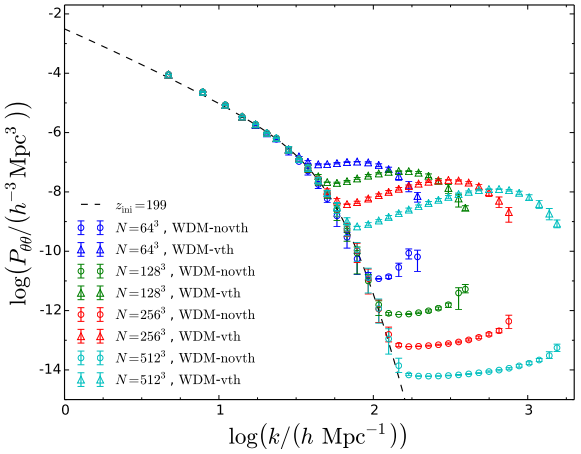

(b) $L = 2\ h^{-1}$Mpc, $m_{\rm WDM} = 3.3$ keV. Varying N.

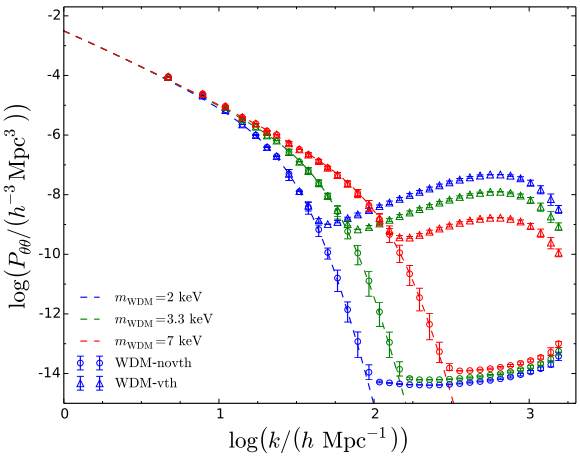

(c) $N = 512^3$, $L = 2\ h^{-1}$Mpc. Varying $m_{\rm WDM}$.

Figure 2.2: Velocity power spectra measured from ICs for WDM-vth (triangles) and WDM-novth (dots). The different panels show how the spectra change when varying (a) the box length L, (b) the number of particles N and (c) the mass of WDM $m_{\rm WDM}$, while fixing the other parameters. We normalise the velocity power spectra such that $P_{\theta\theta} = P_{\delta\delta}$ (see Eq. (2.3.6)), in this way they can be directly compared with the theoretical linear matter power spectra given by Eq. (2.3.3) (represented as black dashed lines in this figure). Note that the range of scales plotted on the x-axis and y-axis in each panel is different.

noise. The numerical noise originates in the way we assign a thermal velocity vector to a simulation particle. This can be understood by the following argument. The ICs are generated starting from a homogeneous grid of simulation particles and associating a velocity vector $\vec{v}$ at each particle on the grid. Simulation particles in CDM simulations (or in WDM simulations without thermal velocities) have no thermal velocities, so only peculiar velocities contribute to the velocity vector at each grid point, $\vec{v} = \vec{v}_{\rm pec}$. On the other hand, in WDM simulations with thermal velocities we add a random thermal velocity vector to each simulation particle, so the net velocity at each grid point is $\vec{v} = \vec{v}_{\rm pec} + \vec{v}_{\rm therm}$. The simulation particles are initially put onto a grid to suppress shot noise effects. This is sometimes referred to as a "quiet start". When the particles are displaced from a grid the measured matter power spectrum agrees with the target linear theory predictions down to smaller scales than is the case if the particles have a random distribution before they are displaced (see e.g. the discussion on initial particle arrangements in [168]). However, when thermal velocities are included the particles move, on average, a greater distance away from their initial grid positions after the first time step, and effectively "lose memory" of where they started from. Thus, the net effect on the matter power spectrum after the simulation has been evolved for one time step is almost the same as perturbing a random initial particle distribution rather than a "quiet" grid. Therefore, including thermal velocities in the simulation introduces more shot noise compared to that in simulations without thermal velocities. It is well known that the shot noise level is reduced when increasing the simulation resolution (i.e. increasing the number density of the simulation particles); indeed in our results the noise effect is pushed to smaller scales as the resolution improves for simulations with thermal velocities (see figures 2.2(a) and 2.2(b)).

Another way to reduce the noise in the ICs is to choose a lower initial redshift. This is because the impact of thermal velocities decreases linearly with redshift (see Eq. (2.3.2)). However, we cannot make the initial redshift arbitrarily low since at very low redshifts nonlinear corrections to the power spectrum, especially at small

scales, are no longer negligible. In the next section we will discuss how the noise is reduced if we start at a lower redshift.

2.4 Structure formation: evolved matter and velocity spectra

This section is devoted to a study of the nonlinear evolution of the ICs. We consider two sets of ICs, one generated at $z_{\rm ini} = 199$ and the other at a lower redshift, $z_{\rm ini} = 39$, which is chosen because at this redshift the thermal velocities are negligible with respect to peculiar velocities, so we expect that the numerical noise does not affect the ICs. All simulations are performed in a cubic box of length $L = 25\ h^{-1}$Mpc using $N = 512^3$ particles. We choose this pair of $\{N, L\}$ in our simulations since we want to resolve the structures at scales near the half-mode wavenumber (see Eq. (2.3.5)) of our warmer candidates[8] ($m_{\rm WDM} = 2$ keV and 3.3 keV).

We evolve the ICs up to $z = 0$, showing how the noise in the ICs affects the matter and velocity power spectra at intermediate redshifts.

2.4.1 Results for initial conditions generated at $z_{\rm ini} = 199$

Before presenting the quantitative results of our study, let us first show two snapshots of the matter density field to qualitatively appreciate the effects introduced by including thermal velocities in the simulations. In Figure 2.3 we select the same region of the simulation box at $z = 0$ from WDM-novth (upper panel) and from WDM-vth (lower panel) for the WDM candidate with mass $m_{\rm WDM} = 2$ keV. It is well known that WDM simulations - due to the cut-off in the initial power spectrum - display the effects of artificial fragmentation, with regularly-spaced clumps (*spurious*

[8]For $m_{\rm WDM} = 2$ keV and 3.3 keV, the half-mode wavenumbers are within the scales probed accurately by a simulation with $\{N = 512^3, L = 25h^{-1}{\rm Mpc}\}$. However, for $m_{\rm WDM} = 7$ keV the half-mode wavenumber is larger than the Nyquist frequency of the simulation, $k_{\rm Ny} \sim 64\ h/{\rm Mpc}$. In Section 2.5 (when analysing halo properties) we will show some results from a high-resolution simulation, which resolves the half-mode scale for WDM with $m_{\rm WDM} = 7$ keV.

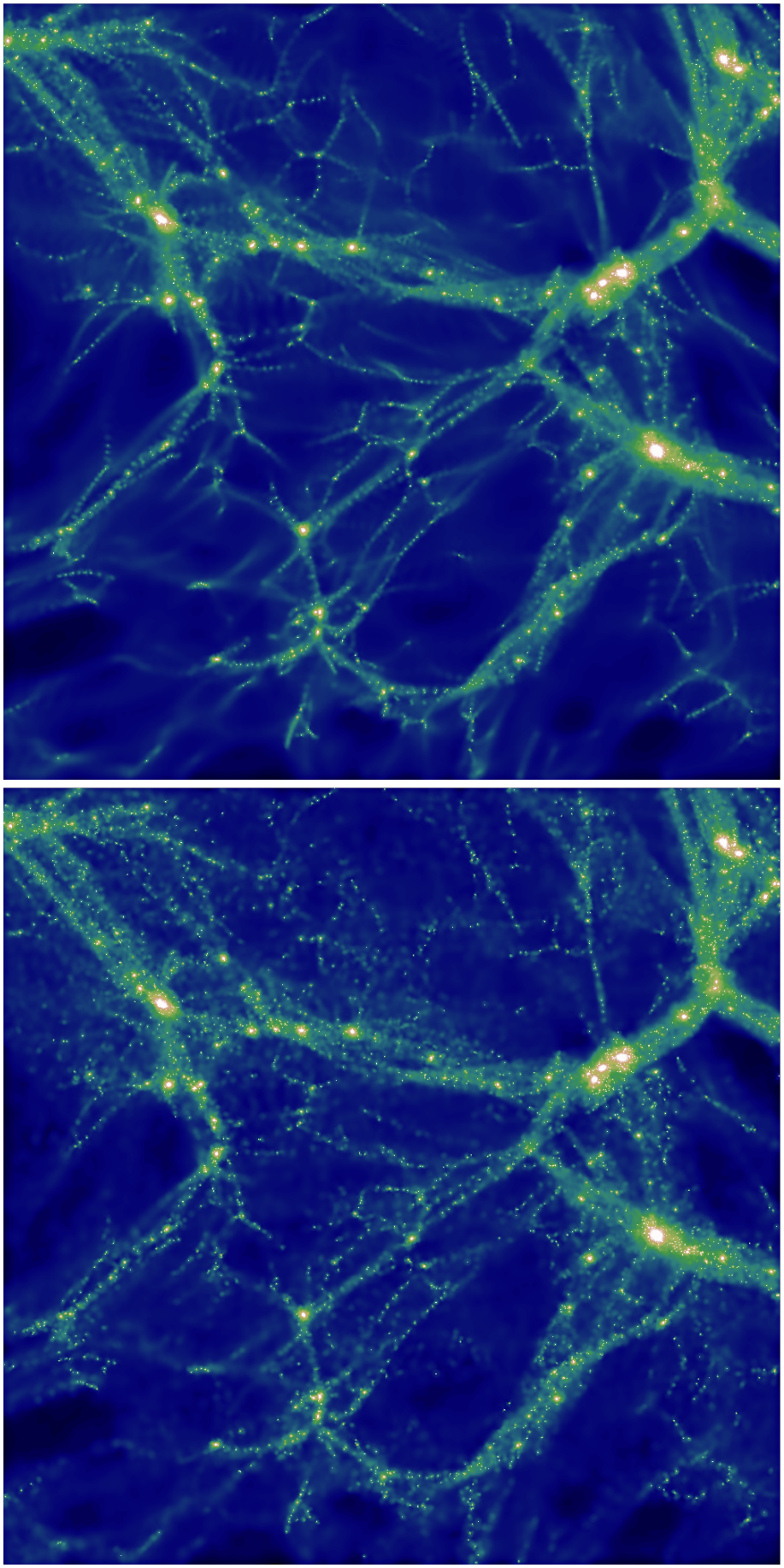

Figure 2.3: Logarithm of the projected mass density field of a region of $(12.5 \times 12.5 \times 2)$ $h^{-3}\mathrm{Mpc}^3$ at $z = 0$ considering a WDM candidate with mass $m_w = 2$ keV. The upper panel is from WDM-novth, while the lower is from WDM-vth. The images are generated using the code Py-SPHViewer [170].

haloes) along filaments, the distance between which reflects the initial inter-particle distance [76, 92, 142, 144–146, 169]. Such spurious haloes are numerical artefacts and can be removed in an attempt to obtain clean, physical, halo catalogues [144, 169]. We find that this artificial effect becomes more prominent when thermal velocities are included in the simulations, due to the extra noise they introduce. In the case of 2 keV WDM particles, we find (see Section 2.5 for more details) that such spurious structures dominate for haloes with mass $M < 10^9 h^{-1}\mathrm{M}_\odot$, which are shown as white dots in Figure 2.3. A quick inspection of Figure 2.3 confirms that simulations with thermal velocities generally show more such structures. However, the spacing of the spurious haloes is less regular than in simulations without thermal velocities. This is because the regularity of the spurious haloes reflects the grid distribution of the simulation particles in the ICs. However, when adding thermal velocities the particles move further than without thermal velocities, and "lose memory" of the initial regular distribution (see the discussion in Section 2.3). This noise effect will also be reflected in terms of enhanced matter clustering on small scales, as we shall see below.

In order to quantify the effects of thermal velocities, in Figure 2.4 we show the matter power spectra from the evolved simulation outputs in the range of redshifts $z \in [199, 0]$. The matter power spectra are measured using the code POWMES [171]. We present the evolved matter power spectra by plotting the nonlinear growth $(P(z)/P(199))\,(D_+(199)/D_+(z))^2$, where $(D_+(199)/D_+(z))^2$ is the ratio between the ΛCDM growth factor at $z = 199$ and at redshift z. This rescaling highlights the changes in the shape of the power spectrum due to nonlinear growth, removing the much bigger change in the amplitude of the power spectrum due to linear growth over a large change in redshift. For comparison we have also displayed the non-linear growth for CDM matter power spectra.

At high redshifts ($z \in [199, 39]$), the wavenumbers probed by our simulations are well inside the linear regime, so the power spectrum ratio plotted is close to unity, which indicates that the power spectrum is evolving according to linear theory for

both the CDM and the three WDM-novth simulations, see Figure 2.4. However, the matter power spectra of WDM-vth deviate from those of WDM-novth at high wavenumbers, as a consequence of the noisier ICs. As expected from the discussion in Section 2.3, the effects of the numerical noise depend on the WDM mass. Defining the ratio between the WDM-vth and WDM-novth matter power spectrum as,

$$R(k,z) \equiv \frac{P^{\text{WDM-vth}}(k,z)}{P^{\text{WDM-novth}}(k,z)}, \tag{2.4.1}$$

R is of the order of ~ 700 at redshift $z = 99$ and at the Nyquist frequency $k_{\text{Ny}} \simeq 64$ h/Mpc for $m_{\text{WDM}} = 2$ keV. It decreases to $R(k_{\text{Ny}}, 99) \sim 30$ for $m_{\text{WDM}} = 3.3$ keV and to $R(k_{\text{Ny}}, 99) \sim 1.3$ for $m_{\text{WDM}} = 7$ keV.

At intermediate redshifts ($z = 9 - 5$), the situation changes. For CDM, the highest wavenumbers probed in our analysis start to enter the nonlinear regime and the ratio of the scaled power spectra starts to deviate from unity. The same effects can be observed in WDM-novth. Note that since the nonlinear evolution transfers power from large scales to small scales, the differences between CDM and the various WDM models are significantly reduced in the nonlinear matter power spectra [156]. Therefore, WDM displays more nonlinear growth than CDM since the WDM initial matter power spectra are highly-suppressed compared to CDM initial $P(k)$ at small scales. At such redshifts, the differences between WDM-vth and WDM-novth are also reduced. For example, simulations with $m_{\text{WDM}} = 2$ keV show the most dramatic deviations at high redshifts: $R(k_{\text{Ny}}, 99) \sim 700$, which become smaller at $z = 9$, $R(k_{\text{Ny}}, 9) \sim 1.5$, and further reduced to $R(k_{\text{Ny}}, 5) \sim 1.07$ at $z = 5$. This is because, being random, the noise effect does not significantly grow in size, and when the effect of gravitational collapse starts to grow it gradually dominates over the noise effect. Similar behaviour is found for the other WDM candidates.

At late times ($z \leq 2$), all the wavenumbers probed in our analysis have entered the nonlinear regime, where the nonlinear growth factors for WDM-vth and WDM-novth are indistinguishable for all three WDM masses. However, small deviations can be seen by looking at the ratio R, as shown in the bottom panels of figures

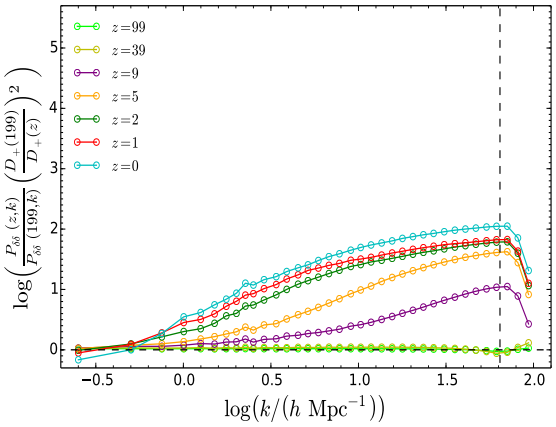

(a) CDM.

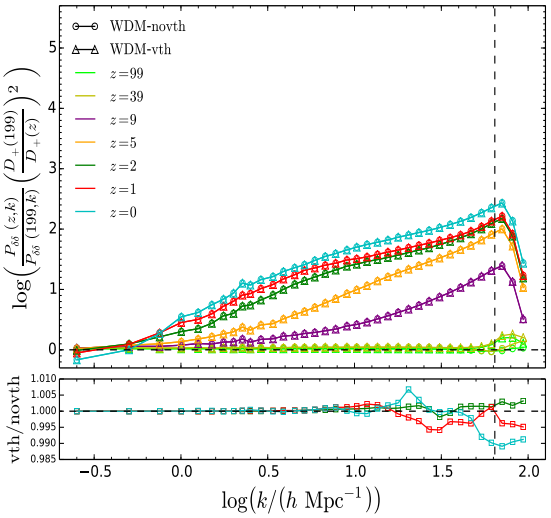

(b) $m_{\mathrm{WDM}} = 7$ keV.

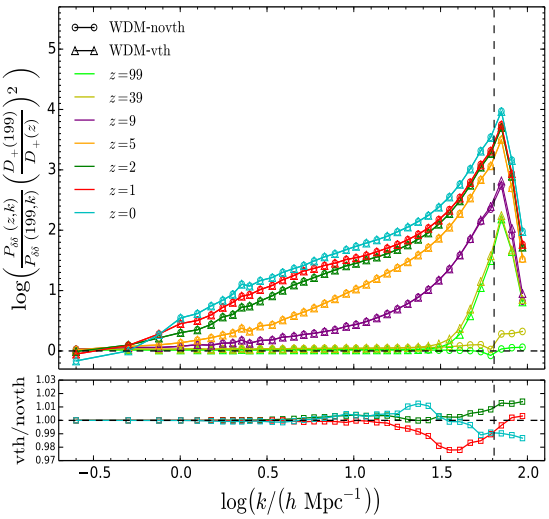

(c) $m_{\mathrm{WDM}} = 3.3$ keV.

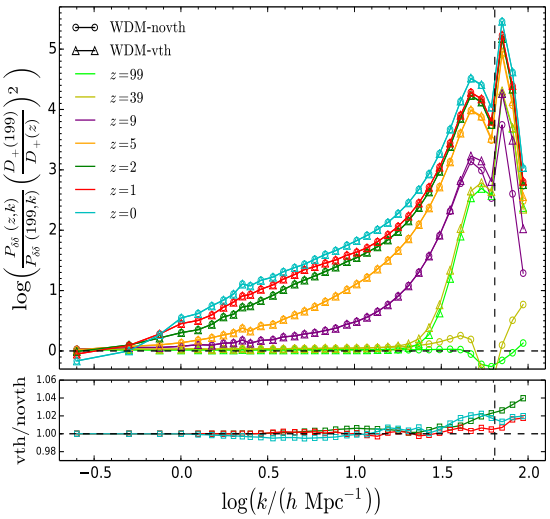

(d) $m_{\mathrm{WDM}} = 2$ keV.

Figure 2.4: Matter power spectra for (a) CDM and WDM with mass (b) $m_{\mathrm{WDM}} = 7$ keV, (c) $m_{\mathrm{WDM}} = 3.3$ keV and (d) $m_{\mathrm{WDM}} = 2$ keV, evolved with GADGET-2 up to redshift $z = 0$. Triangles represent WDM-vth, while dots are WDM-novth. The power spectra are plotted as ratios respect to the initial power spectrum at $z_{\mathrm{ini}} = 199$ scaled to take out the difference between the ΛCDM growth factor at $z = 199$ and the evolved simulation at redshift z. The bottom panels in figures (b-d) show the ratio between WDM-vth and WDM-novth at redshifts $z = 2$ (green), $z = 1$ (red), $z = 0$ (cyan). The dashed vertical line shows the Nyquist frequency.

2.4(b), 2.4(c), 2.4(d). As we can see, for all the WDM candidates studied here, the difference in the power spectra of WDM-vth with respect to WDM-novth is less than 2% below k_{Ny} for redshifts $z \leq 2$.

We have performed a similar analysis for the velocity power spectra. Since the thermal velocity noise also affects the initial redshift $z_{\rm ini} = 199$, in our plots we choose to take the nonlinear growth $(P(z)/P(199))\,(D_+(199)/D_+(z))^2$ by dividing all the power spectra (WDM-vth and WDM-novth) by the initial noiseless velocity power spectrum $P(z_{\rm ini} = 199)$. Figure 2.5 shows the results for CDM and the three WDM simulations. The noise effect in WDM-vth is dominant at high redshifts. For example, the ratio R for the velocity power spectrum is around $R(k_{\rm Ny}, 99) \sim 3000$ for $m_{\rm WDM} = 2$ keV. The impact of the noise depends on the mass and R is smaller for the two colder WDM candidates: $R(k_{\rm Ny}, 99) \sim 100$ for $m_{\rm WDM} = 3.3$ keV and $R(k_{\rm Ny}, 99) \sim 1.8$ for $m_{\rm WDM} = 7$ keV.

At intermediate ($z = 9 - 5$) and low redshifts ($z \leq 2$), the highest wavenumbers probed in our simulations have entered the non-linear regime. However, the transfer of power from large to small scales is more pronounced for the velocity $P(k)$, with the power transfer wavenumber moving to higher k. At these redshifts the effects due to the noise in the ICs of WDM-vth are strongly reduced. For the warmest candidate ($m_{\rm WDM} = 2$ keV) we find that $R(k_{\rm Ny}, 9) \sim 2.5$ at $z = 9$, which is further reduced to $R(k_{\rm Ny}, 5) \sim 1.2$ at $z = 5$. Similar behaviour is found for the other WDM candidates.

The values of the ratio R at the lowest redshifts $z = 2, 1, 0$ are plotted in the bottom panels of figures 2.5(b), 2.5(c), 2.5(d). As we can see, unlike the matter power spectra, in the velocity power spectra R does not decrease at $z \leq 2$, but rather its peak shifts to lower k when z decreases. For example, for the warmest candidate, R has a peak at $k \sim 50$ h/Mpc at $z = 2$ and it is shifted to small wavenumbers, $k \sim 32$ h/Mpc, at $z = 0$, while the magnitude of the peak does not change and is around 18% for all $z \leq 2$. For $m_{\rm WDM} = 3.3$ keV, we find the same result, but in this case the magnitude of the peak is around $R \sim 6\%$ for all $z \leq 2$. For $m_{\rm WDM} = 7$ keV,

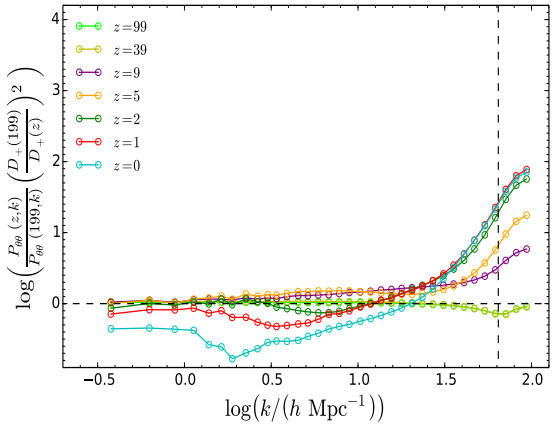

(a) CDM.

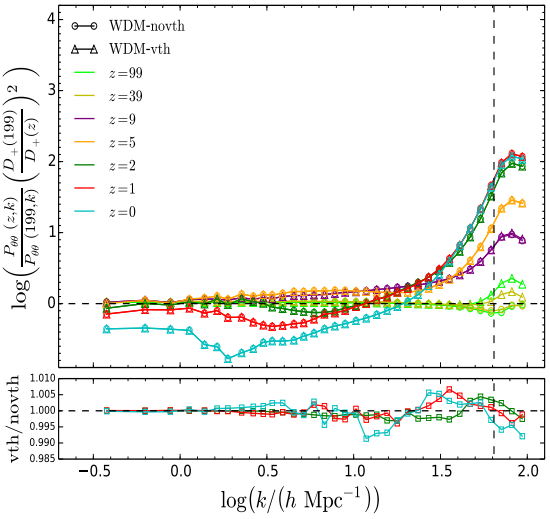

(b) $m_{\mathrm{WDM}} = 7$ keV.

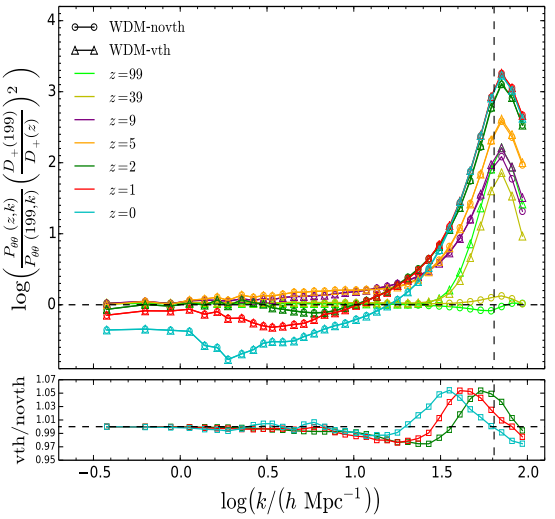

(c) $m_{\mathrm{WDM}} = 3.3$ keV.

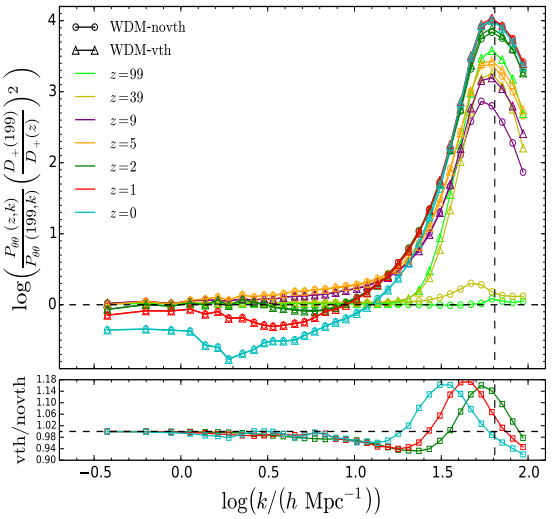

(d) $m_{\mathrm{WDM}} = 2$ keV.

Figure 2.5: The same as Figure 2.4, but for velocity power spectra. All spectra are divided by the initial noiseless spectrum at $z = 199$ (the velocity spectrum measured from the ICs for WDM-novth).

R is always well below 1% for redshifts $z \leq 2$.

In conclusion, the matter and velocity power spectra for WDM-vth are always affected by the noise. The importance of the noise is reduced when the system evolves and the nonlinear gravitational evolution starts to dominate. However, we note that in the warmest WDM scenario examined here ($m_{\rm WDM} = 2$ keV), the noise still affects appreciably the velocity power spectra at $z \leq 2$, causing deviations of the order of $\sim 18\%$. Therefore, adding thermal velocities reduces the range of validity of the simulation predictions.

2.4.2 Results for initial conditions generated at $z_{\rm ini} = 39$

It was suggested by [154] for WDM candidates and [151, 152] for active neutrinos that a useful way to suppress the effect of the thermal velocity noise in the matter power spectrum is to start the simulation at a lower redshift, when the thermal velocity contribution is smaller (see Eq. (2.3.2)). To check this, we have run another set of simulations with initial redshift $z_{\rm ini} = 39$. We have evolved the two sets of ICs (the one at $z_{\rm ini} = 199$ and the other at $z_{\rm ini} = 39$) to $z = 19$ and measured the matter power spectra from the snapshots at $z = 39$ and $z = 19$.

The results for $m_{\rm WDM} = 3.3$ keV are shown in Figure 2.6. The ratio R given in Eq. (2.4.1) is of the order of ~ 30 at $z = 39$ and at the Nyquist frequency $k_{\rm Ny} \sim 64$ h/Mpc for the first set of simulations with starting redshift at $z_{\rm ini} = 199$, while it is exactly 1 for all the wavenumbers probed in the simulations with the ICs at $z_{\rm ini} = 39$. This is because the $z = 39$ snapshots are the ICs for the second set of simulations and, as mentioned in Section 2.3, the matter power spectra measured from the ICs are not affected by the noise. On the other hand, the (evolved) matter power spectra at $z = 19$ are affected by the noise in both the two sets of WDM-vth simulations, but the choice of a lower starting redshift reduces the differences with respect to WDM-novth. Indeed, the matter power spectrum measured from WDM-vth with the ICs at $z_{\rm ini} = 199$ is affected by the noise and deviates significantly at high wavenumbers from the result measured from WDM-novth at $z = 19$. Quantitatively,

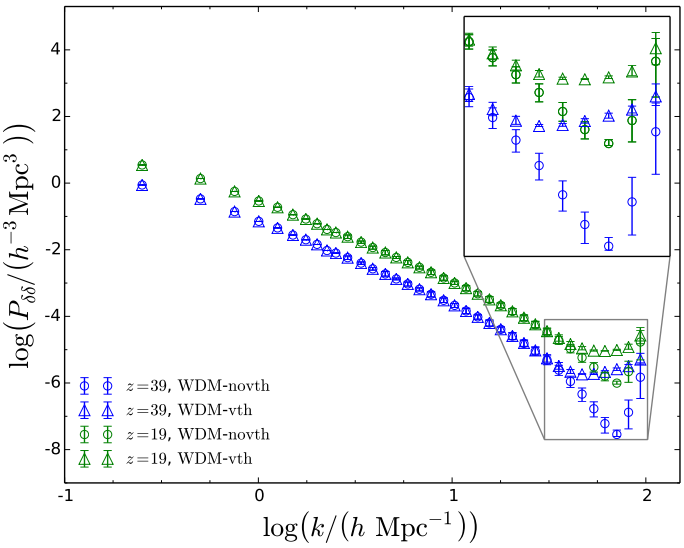

(a) ICs at $z = 199$.

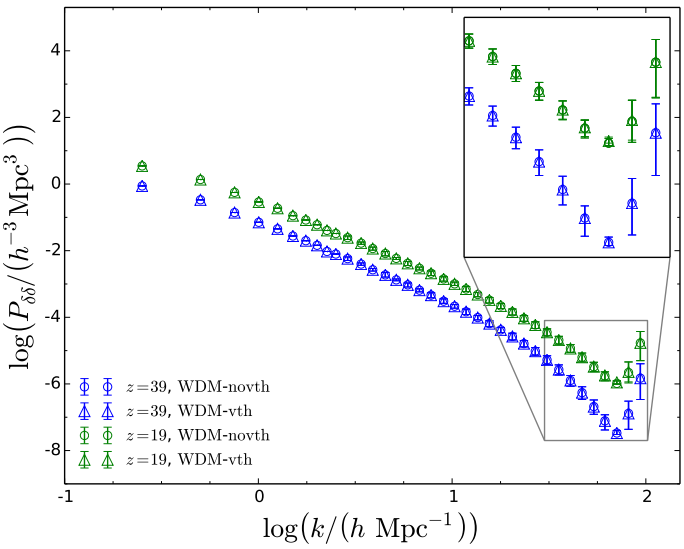

(b) ICs at $z = 39$.

Figure 2.6: (a) Matter power spectra at redshifts $z = 39, 19$ for WDM with $m_w = 3.3$ keV with the ICs at $z_{\rm ini} = 199$. (b) Matter power spectra at redshifts $z = 39, 19$ for WDM with $m_w = 3.3$ keV with the ICs at $z_{\rm ini} = 39$.

we have $R \sim 10$ at $z = 19$ and near $k_{\rm Ny}$ for simulations with the ICs at $z_{\rm ini} = 199$. However, in the case of ICs at $z_{\rm ini} = 39$ the differences in the matter power spectra when adding thermal velocities are negligible, e.g. at $z = 19$ we have $R \lesssim 1.04$ for $k < k_{\rm Ny}$. This test confirms that the enhanced power observed in simulations with thermal velocities is numerical and can be reduced by choosing a lower initial redshift.

By starting at a lower redshift we inevitably lose information about the high redshift evolution of the system and the accuracy of the simulations could be compromised. This is because we need to evolve the simulation over a large number of expansion factors away from ICs to get the proper gravitational evolution of the density field. However, using second-order Lagrangian perturbation theory (on which the code 2LPTic is based) the accuracy of the simulations without thermal velocities starting at low redshift ($z_{\rm ini} = 39$) is not seriously compromised for the scales resolved in our simulations. For example, considering the two power spectra at $z = 19$ displayed in Figure 2.6 (those measured from WDM-novth with ICs at $z_{\rm ini} = 199$ and from WDM-novth with ICs at $z_{\rm ini} = 39$ respectively), we find that they agree between each other up to $k \sim 10\,h/{\rm Mpc}$. Above such wavenumbers the $P(k)$ with ICs at $z_{\rm ini} = 39$ displays more power than that with ICs at $z_{\rm ini} = 199$, although the differences in the amplitudes between the two power spectra never exceed $\sim 10\%$. So, starting at low redshift does not affect the results significantly from simulations without thermal velocities, while it drastically reduces the extra numerical noise introduced when adding thermal velocities.

2.5 Halo properties

As found in the previous section, the numerical noise caused by including thermal velocities influences even the lowest redshifts. We expect that some halo properties can also be affected by this noise. In this section, we quantify how the WDM-vth simulations differ from WDM-novth in halo properties, such as the halo mass

function and halo density profiles.

2.5.1 Halo mass functions

It is well known that a reduction in power on small scales is reflected in the suppression of the number of low mass structures in the Universe (once spurious structures have been removed) [76, 92, 142, 144–146, 169]. This can be seen by counting the number of haloes as a function of mass (i.e. the halo mass function) in WDM simulations, and comparing with the result from a CDM simulation. As we saw in Section 2.4, the noise in the ICs due to thermal velocities propagates to late times and could influence the halo mass function. To study this we focus on simulation snapshots at $z = 0$. To extract the halo properties, we use the code ROCKSTAR, which is a phase-space friend-of-friends halo finder [172]. We use the virial mass ($M_{\rm vir}$) to characterise the haloes, which is defined as the mass enclosed in a sphere of radius $r_{\rm vir}$, where $r_{\rm vir}$ is the virial radius given in [173]. The (differential) halo mass function is presented as $F(M_{\rm vir}, z) = dn/d\log(M_{\rm vir})$, where n is the number density of haloes with virial mass $M_{\rm vir}$.

As mentioned in Section 2.4, WDM simulations (in which the initial power spectrum has a resolved cut-off) are affected by the artificial fragmentation of filaments, i.e. spurious haloes, which can be seen as an upturn in the halo mass function at small masses. A mass cut-off, $M_{\rm lim}$, was proposed in [169] below which haloes are likely to be spurious[9]:

$$M_{\rm lim} = 10.1\,\bar{\rho}\,d\,k_{\rm peak}^{-2}, \tag{2.5.1}$$

where $\bar{\rho}$ is the mean density of the Universe, d is the mean interparticle separation and $k_{\rm peak}$ is the wavenumber at which the dimensionless matter power spectrum, $\Delta(k) \equiv k^3P(k)/(2\pi^2)$, has its maximum. The simulations used by [169] did not

[9]This limit can be considered as an estimate. Not all of the haloes with masses below this limit are unphysical. Furthermore there could be some spurious haloes with masses above this limit. The common way to find the unphysical haloes is explained in [144]. Since our treatment is simply intended to show the effects of adding thermal velocities, here we will not go into a detailed study of how to eliminate spurious haloes. We postpone the discussion on how to remove unphysical haloes in WDM models in Chapter 4.

include thermal velocities.

In Figure 2.7 we plot the ratio between the halo mass functions measured from our WDM and CDM simulations. As we can see in the figure, at the largest masses probed by our simulations the WDM and CDM models predict the same number of haloes. However, the halo abundance in WDM is progressively reduced at smaller masses. The mass scales at which the damping of the structures appears depend on the WDM particle mass. Colder candidates shift the damping in the halo mass function towards smaller masses. However, all the WDM halo mass functions in Figure 2.7 show a clear upturn at low masses, which is evidence of spurious haloes. For WDM-novth, the mass scale at which the upturn appears is well described by Eq. (2.5.1) (see the red vertical dashed line in figures 2.7(a) and 2.7(b); the results for the candidate with $m_{\rm WDM} = 7$ keV will be treated separately). However, Eq. (2.5.1) fails to reproduce the position of the upturn seen in our WDM-vth simulations. As we can see, there are more (spurious) substructures at low masses in WDM-vth and these spurious haloes appear at larger masses than in WDM-novth. These differences are caused by the additional noise present in WDM-vth. We have found a revised mass cut-off for WDM-vth (see the cyan vertical dashed line in Figure 2.7),

$$M_{\rm lim} = 32.2\,\bar{\rho}\,d\,k_{\rm peak}^{-2}. \tag{2.5.2}$$

Eq. (2.5.1) (for WDM-novth) and our result (2.5.2) (for WDM-vth) reproduce quite well the cut-off scales for WDM candidates with masses $m_{\rm WDM} = 2$ keV and 3.3 keV. However, both formulae fail to reproduce the predicted mass cut-off for the coldest candidate ($m_{\rm WDM} = 7$ keV) in a simulation with a box length of 25 h^{-1}Mpc and 512^3 particles (see Figure 2.7(c)). The reason is that this simulation has a Nyquist frequency $k_{\rm Ny} \sim 64\ h$/Mpc, which is below the half-mode wavenumber $k_{1/2} \sim 83\ h$/Mpc (see Figure 2.1(b)) for the case of $m_{\rm WDM} = 7$ keV. The simulation does not fully resolve the power spectrum cut-off for such heavy WDM masses, and consequently only produces deviations from CDM at very small mass scales, as shown in Figure 2.7(c). To study the effects on the halo mass function for

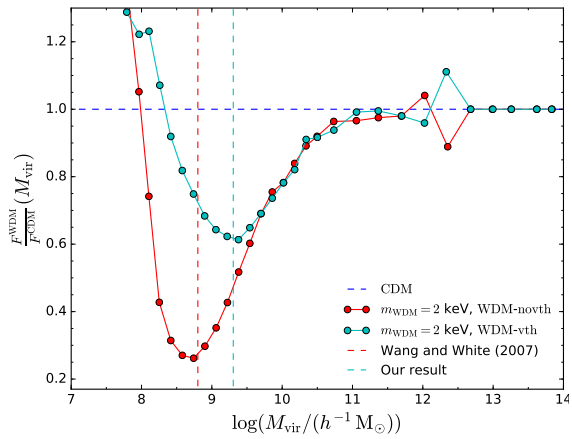

(a) $m_{\rm WDM} = 2$ keV, $L = 25\ h^{-1}$Mpc

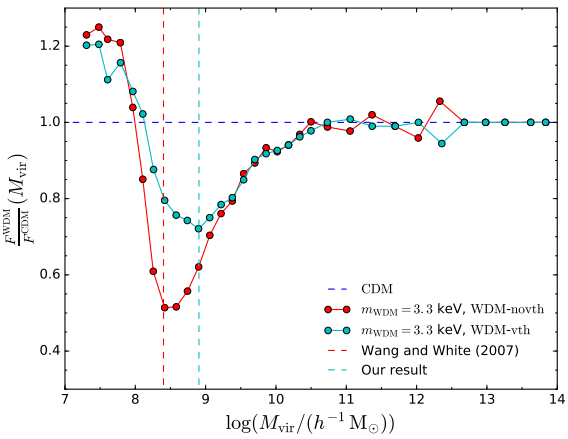

(b) $m_{\rm WDM} = 3.3$ keV, $L = 25\ h^{-1}$Mpc

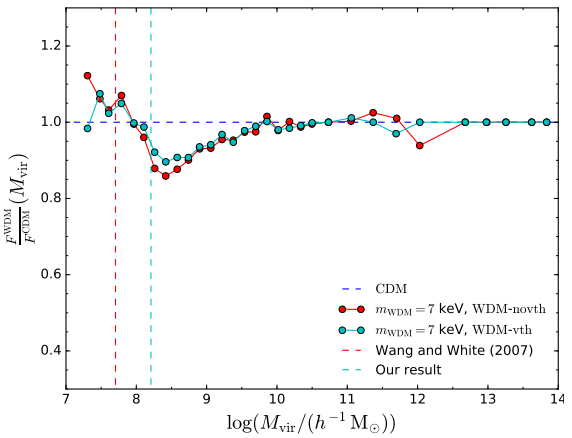

(c) $m_{\rm WDM} = 7$ keV, $L = 25\ h^{-1}$Mpc

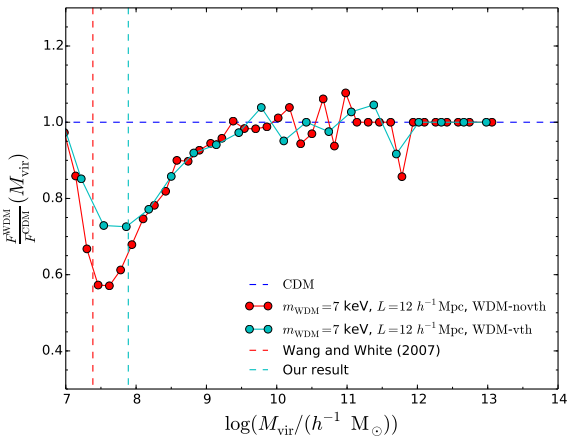

(d) $m_{\rm WDM} = 7$ keV, $L = 12\ h^{-1}$Mpc

Figure 2.7: Halo mass function for WDM plotted as a ratio with respect to CDM. WDM-vth are in cyan, while WDM-novth are in red. The red vertical dashed line is the mass cut-off suggested in [169] (see Eq. (2.5.1)) to take care of the spurious haloes. The cyan vertical dashed line is our limit for simulations with thermal velocities (see Eq. (2.5.2)). The halo mass functions are measured from the simulations at redshift $z = 0$. For (a) (b) (c) the simulation box size is $L = 25\ h^{-1}$Mpc. For the $m_{\rm WDM} = 7$ keV candidate we ran an extra simulation (d) with a smaller box size, $L = 12\ h^{-1}$Mpc.

$m_{\rm WDM} = 7$ keV we ran an additional simulation with a box length of 12 h^{-1}Mpc and 512^3 particles, which has a Nyquist frequency $k_{\rm Ny} \sim 134$ h/Mpc. The results are shown in Figure 2.7(d), where we can see that the two formulae (2.5.1) and (2.5.2) describe the mass cut-off in the high simulation run very well.

Although the results are presented for $z = 0$, we have found that the mass below which spurious haloes become important is the same at higher redshifts, i.e. the spurious haloes appear at roughly the same mass independently of the redshift considered. This is true for simulations with and without thermal velocities.

2.5.2 Radial density profiles

In addition to the halo mass function, we investigate if the radial density profile of haloes in WDM simulations is affected by numerical noise. It is well known that CDM haloes exhibit cuspy profiles [53–55], described by the NFW fitting formula [55],

$$\frac{\rho_{\rm fit}(r)}{\rho_c} = \frac{\delta_c}{\frac{r}{r_s}\left(1+\frac{r}{r_s}\right)^2}, \tag{2.5.3}$$

where δ_c is the characteristic overdensity and r_s is the scale radius.

In [147] it was found that WDM radial density profiles also follow a NFW form in the outer parts of the halo. We examine this feature in Figure 2.8, where we display some examples of radial density profiles measured from simulations at $z = 0$, stacking haloes in mass bins centred on $\log(M_{\rm vir}^{\rm central}/h^{-1}{\rm M}_\odot) = 10, 11.8$ with width 0.2 dex. We plot the median density for the haloes in each radial bin. The radial bins are chosen such that the logarithmic difference between the central radius values (r_i) for two near bins is $|\log(r_i/r_{\rm vir}) - \log(r_{i+1}/r_{\rm vir})| = 0.2$ with $i \in \{1, N_{\rm bin}\}$ and $N_{\rm bin}$ is the total number of bins. We fit the NFW formula using each of these dark matter profiles between the convergence radius[10] $r_{\rm conv}$ and the virial radius $r_{\rm vir}$. The

[10]The convergence radius is defined to be the radius within which the relaxation time is of the order of the age of the Universe [174] and it is intended as the radius beyond which the halo mass density profile is reliably modelled for a given halo mass for a given simulation set-up.

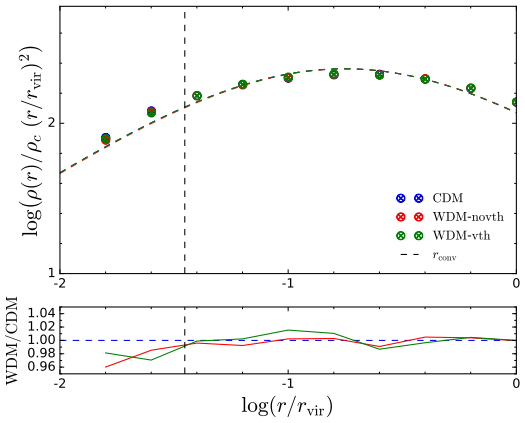

(a) $\log_{10}(M_{halo}/h^{-1}\mathrm{M}_\odot) = (11.8 \pm 0.2)$, averaged over 101 haloes for CDM, 102 for WDM-novth and 100 for WDM-vth.

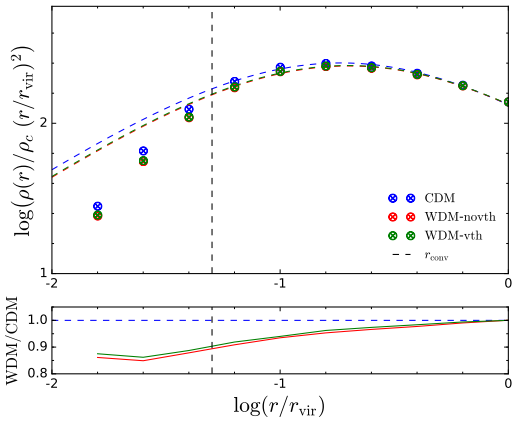

(b) $\log_{10}(M_{halo}/h^{-1}\mathrm{M}_\odot) = (10 \pm 0.2)$, averaged over 4104 haloes for CDM, 3867 for WDM-novth and 3862 for WDM-vth.

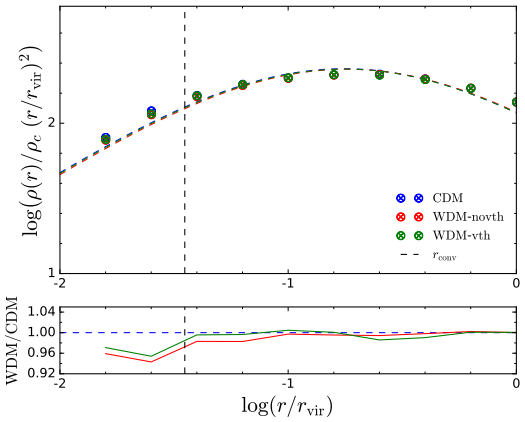

(c) $\log_{10}(M_{halo}/h^{-1}\mathrm{M}_\odot) = (11.8 \pm 0.2)$, averaged over 101 haloes for CDM, 103 for WDM-novth and 103 for WDM-vth.

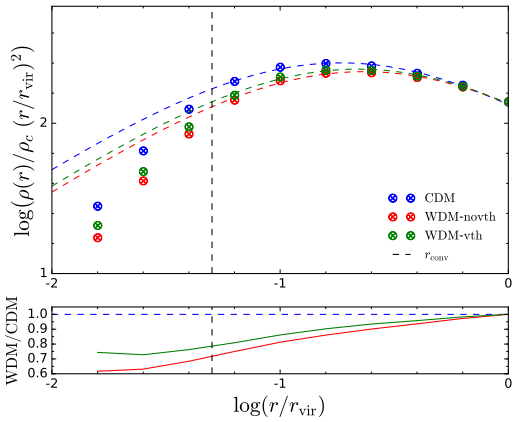

(d) $\log_{10}(M_{halo}/h^{-1}\mathrm{M}_\odot) = (10 \pm 0.2)$, averaged over 4104 haloes for CDM, 3256 for WDM-novth and 3201 for WDM-vth.

Figure 2.8: Some halo radial density profiles extracted from CDM (blue), WDM-vth (green) and WDM-novth (red) simulations at $z = 0$. (a-b) WDM with mass $m_{\rm WDM} = 3.3$ keV. (c-d) WDM with mass $m_{\rm WDM} = 2$ keV. The coloured dashed curves represent the NFW fits of the radial density profiles measured from simulations. The black dashed line displays the position of the convergence radius $r_{\rm conv}$. The bottom panel of each figure shows the ratio between the WDM and CDM radial profiles measured from our simulations.

best fit is found by minimising the following sum of squares:

$$Q_{N_{\rm bin}}(\delta_c, r_s) = \frac{1}{N_{\rm bin}} \sum_{i=1}^{N_{\rm bin}} \left[\log\left(\frac{\rho_i}{\rho_c} \left(\frac{r_i}{r_{\rm vir}} \right)^2 \right) - \log\left(\frac{\rho_{\rm fit}(r_i, \delta_c, r_s)}{\rho_c} \left(\frac{r_i}{r_{\rm vir}} \right)^2 \right) \right]^2 , \quad (2.5.4)$$

where ρ_i is the value of the radial density profile extracted from our simulations at the radius r_i, while $\rho_{\rm fit}(r_i, \delta_c, r_s)$ is the value of the NFW fit in Eq. (2.5.3) at the same radius r_i. As we can see from Figure 2.8, the halo radial density profiles extracted from our simulations of CDM and WDM both agree quite well with the NFW fits. Moreover, in the larger halo mass bin, the density profiles in the WDM simulations are not significantly affected by the small scale cut-off in the initial power spectrum, so they do not present significant differences with respect to those measured from CDM. This is true for both the WDM candidates with $m_{\rm WDM} = 3.3$ and 2 keV, as can be seen from figures 2.8(a) and 2.8(c) respectively. The effect of adding thermal velocities to the initial conditions is also very small for high mass haloes. In the smaller halo mass bin, on the other hand, the density profiles in WDM simulations are clearly shallower than in CDM towards the halo centres – $\sim 10\%$ for the case of 3.3 keV WDM particles and $\sim 30\%$ for the 2 keV case near the convergence radius. The effect is more prominent in WDM-novth than in WDM-vth. This means that the numerical noise caused by including thermal velocities modifies the slope of the radial density profiles for the small halo masses probed in our analysis.

The concentration parameter, $c_{\rm vir} \equiv r_{\rm vir}/r_s$, is usually used to quantify the steepness of the inner density profiles of NFW haloes. Figure 2.9 shows the values of this parameter at redshift $z = 0$ for our CDM and WDM simulations. At large halo masses, the concentrations measured from WDM and CDM simulations agree well between each other. However, there are differences at lower masses. While the concentration parameter continues to increase in CDM, it turns over and decreases in WDM-novth simulations at small masses (this is well known in the literature, see e.g. [142, 147]). The mass scale at which the downturn appears depends on the WDM candidate mass. For example, the downturn appears at masses $\lesssim 10^{11}\ h^{-1}{\rm M}_\odot$ for the WDM candidate with mass $m_{\rm WDM} = 2$ keV (see Figure 2.9(a)), while it is

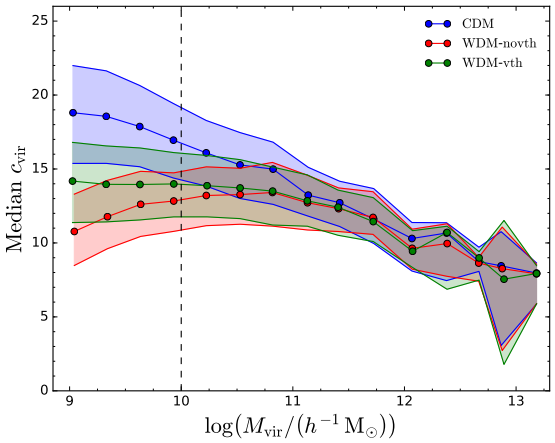

(a) $m_{\rm WDM} = 2$ keV, $L = 25\ h^{-1}$Mpc

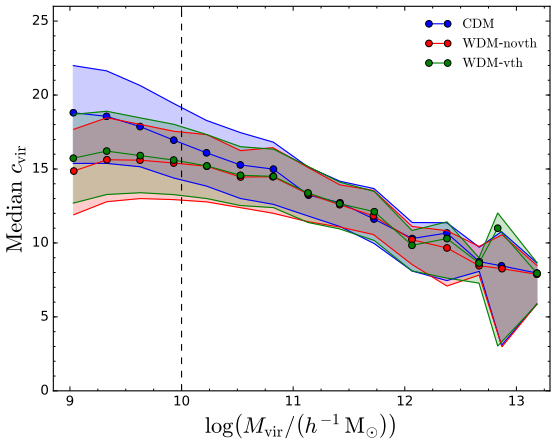

(b) $m_{\rm WDM} = 3.3$ keV, $L = 25\ h^{-1}$Mpc

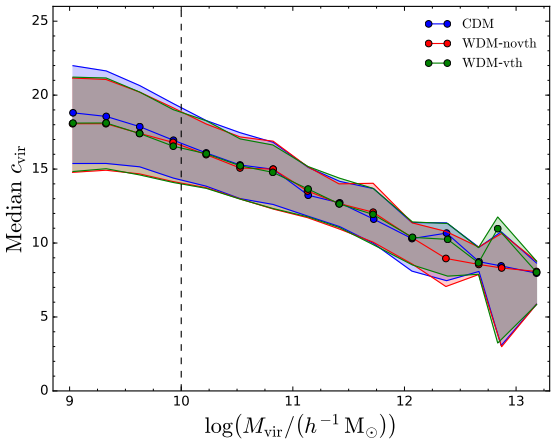

(c) $m_{\rm WDM} = 7$ keV, $L = 25\ h^{-1}$Mpc

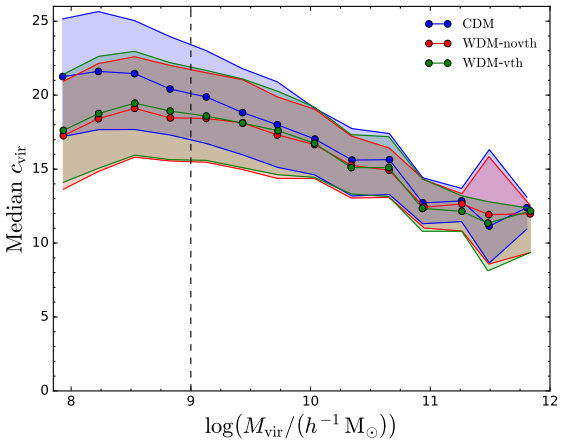

(d) $m_{\rm WDM} = 7$ keV, $L = 12\ h^{-1}$Mpc

Figure 2.9: Median concentration parameter $c_{\rm vir}$ for CDM and WDM with $m_{\rm WDM} = 2, 3.3, 7$ keV at redshift $z = 0$. For the WDM candidate mass $m_{\rm WDM} = 7$ keV we present also the results from the high resolution simulation with $L = 12\ h^{-1}$Mpc. The bands show the 68%-ile range around the median. The black vertical dashed line indicates haloes with mass ~ 1000 times the mass of our simulation particles, which is $M_{\rm sim} = 1.01 \times 10^7 h^{-1}{\rm M}_\odot$ for $L = 25\ h^{-1}$Mpc and $M_{\rm sim} = 1.11 \times 10^6 h^{-1}{\rm M}_\odot$ for $L = 12\ h^{-1}$Mpc.

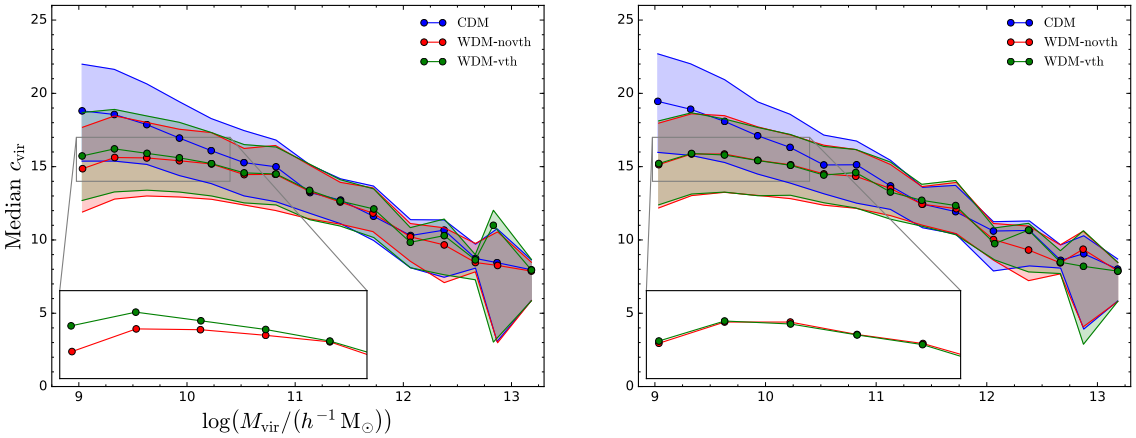

(a) ICs at $z_{\rm ini} = 199$. (b) ICs at $z_{\rm ini} = 39$.

Figure 2.10: Median concentration parameter $c_{\rm vir}$ at $z = 0$ for CDM and WDM with $m_{\rm WDM} = 3.3$ keV for simulations with (a) ICs at $z_{\rm ini} = 199$ and (b) ICs at $z_{\rm ini} = 39$. The bands show the 68%-ile range around the median.

shifted to smaller masses, $\lesssim 3 \times 10^8\ h^{-1}{\rm M}_\odot$, for the case of $m_{\rm WDM} = 7$ keV (see Figure 2.9(d)).

In WDM-vth the reduction in the concentration is less pronounced than in WDM-novth; indeed the median values extracted from WDM-vth are in general larger than those measured from WDM-novth at small halo masses. As expected the magnitude of these differences depends on the mass of the WDM candidate. For instance, for masses around $m_{\rm WDM} = 2$ keV, $c_{\rm vir} \simeq 13.9 \pm 2.2$ (the 68%-ile range around the median) in WDM-vth for haloes with masses of $10^{10}\ h^{-1}{\rm M}_\odot$, while the value predicted from WDM-novth is $c_{\rm vir} \simeq 12.8$. For colder WDM candidates the effect is weaker at the mass scales probed by our simulations; indeed for the case of particle mass $m_{\rm WDM} = 7$ keV the effect is negligible for simulations with $L = 25$ h^{-1}Mpc (see Figure 2.9(c)), while some differences can be noticed at the very small masses in simulation with $L = 12\ h^{-1}$Mpc (see Figure 2.9(d)), however the values of $c_{\rm vir}$ measured from WDM-novth and WDM-vth simulations are always compatible between each other within the 68%-ile range around the median.

For completeness, we have compared the halo concentration-mass relations for WDM and CDM simulations starting at different initial redshifts ($z_{\rm ini} = 199$ on

the left and 39 on the right), for the case of $m_{\rm WDM} = 3.3$ keV, in Figure 2.10. The differences between WDM-vth and WDM-novth seen in simulations with initial redshift $z_{\rm ini} = 199$ are not present in those starting at $z_{\rm ini} = 39$. This confirms that the observed deviations in the halo properties of simulations with thermal velocities are due to numerical artefacts.

As studied in [148–150], imprinting primordial thermal velocities on the particles ensures a "phase-packing" limit, which prevents the density in the central region of the haloes from increasing arbitrarily, producing a central core. However, for values of WDM candidate masses compatible with the upper limits from the Ly-α forest [132, 133], the cores are only a few parsecs in size and not astrophysically relevant [149, 150]. This explains why we do not expect to find such new physical features in halo properties when adding thermal velocities.

2.6 Summary and Conclusions

Thermal WDM candidates are characterised by Fermi-Dirac distributions for the thermal velocities. However, apart from the induced free-streaming effect, the role of thermal velocities in structure formation remains unclear. We have investigated the effect of thermal velocities in N-body simulations of structure formation in WDM cosmologies when the thermal velocities are imposed on the simulation particles.

At high redshift, $z = 199$, thermal velocity dispersions are non-negligible with respect to the peculiar velocities and they must be taken into account in the initial conditions. However, when this is done, a new source of numerical noise affects the simulations. We have improved upon the results presented in [154] by increasing the simulation resolution to reach the scales relevant to free-streaming. The results in [154] are based on a WDM candidate (a non-thermal sterile neutrino with mass 0.5 keV), which is now ruled out by the current Ly-α constraints [132, 133]. Here, we have focused on more realistic WDM masses, $m_{\rm WDM} \geq 2$ keV, which can be compatible with the limits from the Ly-α forest. Moreover, we have extended the

analysis of [154] by measuring the velocity power spectra, spanning a vast range of redshifts, from early times ($z = 199$) to the present day and we have estimated the impact of the noise at different times. The initial velocity power spectrum in simulations with thermal velocities is always affected by the noise caused by adding thermal velocities to the peculiar velocities of simulation particles. The noise propagates to all subsequent times, influencing the matter and velocity power spectra. These numerical artefacts dramatically affect the simulation predictions at early times, when all the modes are in the linear regime, producing enhancements in the velocity power of ~ 100 (for WDM candidates with masses of 3.3 keV) and of ~ 3000 (for masses of 2 keV) at the Nyquist frequency $k_{Ny} \sim 64\ h/\mathrm{Mpc}$. At late times, these effects are less pronounced because the non-linear growth of structure gradually dominates over the noise. Indeed, at $z \leq 2$ the deviations do not exceed 6% in the velocity spectrum and 2% in the matter spectrum for scales $10 < k < 64$ h/Mpc for masses of 3.3 keV. However, for the masses around 2 keV there are still appreciable deviations in the velocity power spectrum at $z \leq 2$ around 18%.

Looking at halo properties at late times, such as the halo mass function and the radial density profile of haloes, we found some differences in simulations with thermal velocities with respect to those without. These deviations are due to the noisy initial conditions of the simulations which include thermal velocities. Due to this new source of noise, more spurious substructures appear and the cut-off mass proposed by [169] fails to reproduce the mass at which the upturn in the halo mass function appears due to spurious haloes. We find a new mass cut-off, $M_{\mathrm{lim}} = 32.2\,\bar{\rho}\,d\,k_{\mathrm{peak}}^{-2}$, which works better at reproducing the mass scale below which spurious haloes start to be important in simulations with thermal velocities. However, we note that the amount of numerical noise introduced in simulations with thermal velocities depends also on the starting redshift of the simulations. This new mass cut-off is then expected to reproduce the mass upturn for simulations with ICs at $z = 199$ only. To assess the impact of the numerical noise on the halo mass function measured from simulations with a starting initial redshift, it is necessary to carry out a similar analysis as done

here for the case of ICs at $z = 199$.

The standard practice of imposing thermal velocities in N-body simulations by adding them to the peculiar velocities in the initial conditions then reduces the range of validity of simulation predictions with respect to simulations without thermal velocities because of the noise introduced in the initial conditions. The noise can be reduced by increasing the number of simulation particles or starting at a lower redshift. Obviously, both of the options introduce side effects: increasing the number of particles increases the computational time needed to evolve the simulations, while by starting at very low redshifts, we inevitably lose information about the high redshift behaviour of the system and the accuracy of the calculation could also be reduced. Our results help to determine the range of applicability of simulations of WDM.

Chapter 3

Nonlinear growth of structure in damped models

3.1 Introduction

Damped models such as WDM introduce a characteristic scale below which the density fluctuations are erased resulting in a cut-off appearing in the linear matter power spectrum. As we saw in Chapter 2, N-body simulations can be a powerful tool to model the nonlinear evolution of cosmic structure and can also be used to study the effects of the damping on small scales. In the previous chapter, we focused on the thermal WDM model, we now move to study other power spectra with damped matter fluctuations on small scales. Different damped models (coming from different particle physics models, see Section 1.2) display different forms for the linear power spectrum, whose shape and cut-off position depend on the particular model. This implies that, in principle, one needs to analyse the entire plethora of power spectra (each coming from a specific scenario and a specific set of particle physics parameters) to study the impact of every single damped model on structure formation. In [75], the authors found a general parametrisation of the power spectrum with three free parameters, which is flexible enough to reproduce accurately the linear power spectra of a large class of nCDM models.

However, the nonlinear evolution of structure transfers power from large scales to small scales, so the differences at small scales between standard ΛCDM and the damped models can be significantly reduced in the nonlinear matter power spectra (c.f. Figure 2.4, but see also [156]). It is therefore interesting to understand how well different damped models can be distinguished from the point of view of cosmological structure measurements and if there is a limit to how much simulations can tell us about different models. In other words, if two damped linear spectra are very similar to one another on large scales and they only differ appreciably at small scales (say, below the half-mode wavelength defined in Subsection 2.3.1), we can ask if such differences survive the nonlinear growth of structure and what imprint, if any, they leave behind. If gravitational instability erases these differences, the two spectra (although coming from two different theories) give the same results in terms of cosmological observables at late times and, as a consequence, this limits what we can learn about the nature of dark matter from large-scale structure[1].

In this chapter, we show to what extent the full shape of a linear damped power spectrum influences structure formation. We run a series of N-body simulations starting from different initial linear matter power spectra which are identical on large scales but differ substantially on small scales. One of our aims is to establish down to which scale does the shape of the linear power spectrum matter as regards the nonlinear growth of structure. We measure the nonlinear matter power spectra from simulations at low redshifts and compare between one another and with standard CDM results. Moreover, we analyse halo catalogues extracted from the simulations, with particular attention to how the halo mass function is influenced by the initial power spectrum. Based on our results, we propose a 2-parameter model for the initial power spectrum (which we compare against the 3-parameter model found in [75]) and show that two parameters are sufficient to capture the interesting features of the power spectrum from the point of view of structure formation.

[1]Indeed, large scale structure cannot distinguish if the cut-off in the matter power spectrum is due to a primordial damping or a late time DM mechanism. Other observables could be more sensitive to the physics of the early Universe [72].

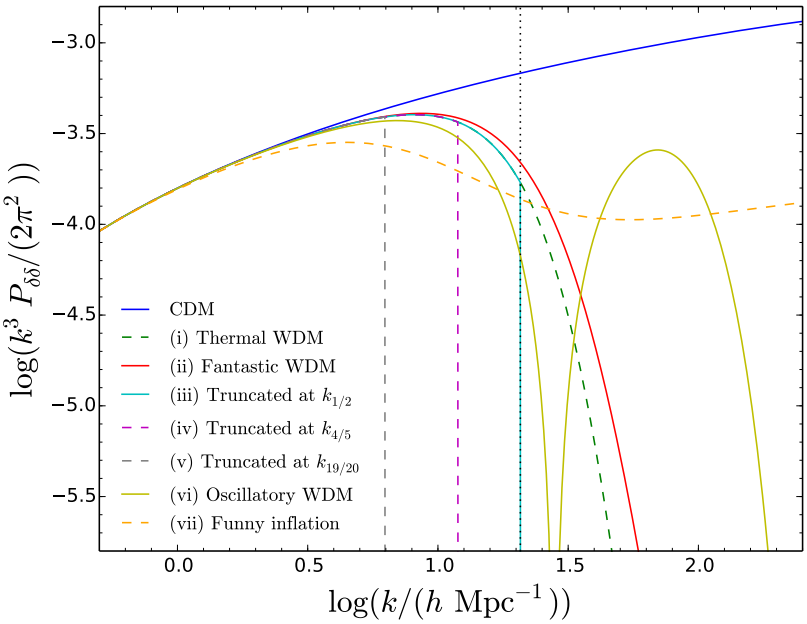

Figure 3.1: Initial linear perturbation theory matter power spectra at $z = 199$ for different models as labelled. The black vertical dotted line represents the half-mode wavenumber $k_{1/2}$ for the thermal WDM power spectrum (green). Note that the power spectrum for the model (vii) is not considered in the analysis conducted in this chapter, it will be taken into account and defined in Chapter 4 when we will look at models from non-standard inflation.

In Section 3.2 of this chapter, we describe the initial power spectra used in our analysis and the set-up of the N-body simulations. In Section 3.3, we present the results from our simulations, measuring nonlinear power spectra and the halo mass function for several damped models. Finally, the description and the results from our 2-parameter fitting formula are presented in Section 3.4. We conclude and summarise in Section 3.5.

3.2 Initial linear-theory power spectra

We consider the following initial damped power spectra (some of these are phenomenological, i.e. specific linear power spectra which have no theoretical motivation, but are considered here as test cases).

i *Thermal WDM* – We consider the matter power spectrum from a thermal WDM candidate as described in Subsection 2.3.1. The WDM candidate is chosen to have

mass $m_{\rm WDM} = 2$ keV. We also introduce three characteristic scales: $k_{1/2}, k_{4/5}$ and $k_{19/20}$. $k_{1/2}$ is the half-mode wavenumber (see Eq. (2.3.5)), at which the thermal WDM transfer function (Eq. (2.3.3)) is suppressed by 50%. While $k_{4/5}$ and $k_{19/20}$ are the wavenumbers at which $T = 4/5$ and $T = 19/20$ respectively, i.e. at these wavenumbers the transfer function is suppressed by 20% and 5% with respect to CDM. Given the parametrisation in Eq. (2.3.3) for $T(k)$ and for a mass of $m_{\rm WDM} = 2$ keV, we have

$$k_{1/2} \simeq 21.2\, h\,{\rm Mpc}^{-1}, \tag{3.2.1}$$

$$k_{4/5} \simeq 12.2\, h\,{\rm Mpc}^{-1}, \tag{3.2.2}$$

$$k_{19/20} \simeq 6.4\, h\,{\rm Mpc}^{-1}, \tag{3.2.3}$$

so, $k_{1/2} > k_{4/5} > k_{19/20}$.

ii *Fantastic WDM* – We generate a second power spectrum from the parametrisation given in Eq. (2.3.3), by fixing the parameters at $\alpha = 0.0233$, $\beta = 2.128$ and $\gamma = -2.946$. We choose this power spectrum because it is identical to the power spectrum for thermal WDM in case (i) at small wavenumbers, while it starts to differ at scales beyond $k \sim k_{4/5}$ (the differences in shape of these two power spectra are very similar to those between a resonantly-produced sterile neutrino and a thermal WDM with candidate mass $m_{\rm WDM} = 3.3$ keV, e.g. see Figure 1 in [147]).

iii *Truncated at* $k_{1/2}$ – The third initial linear power spectrum is obtained by truncating the power spectrum in (i) at $k = k_{1/2}$ such that for $k \leq k_{1/2}$ the $P(k)$ for cases (i) and (iii) are identical, while for $k > k_{1/2}$ the (iii) power spectrum is $P(k > k_{1/2}) = 0$,

$$P_{\rm (iii)}(k) = \begin{cases} P_{\rm (i)}(k) & \text{if} \quad k \leq k_{1/2} \\ 0 & \text{if} \quad k > k_{1/2}. \end{cases} \tag{3.2.4}$$

iv *Truncated at* $k_{4/5}$ – The fourth power spectrum is obtained by truncating the power spectrum in (i) at $k = k_{4/5}$ such that for $k \leq k_{4/5}$ the $P(k)$ for cases (i) and (iv) are identical, while for $k > k_{4/5}$ the (iv) power spectrum is $P(k > k_{4/5}) = 0$,

$$P_{(\mathrm{iv})}(k) = \begin{cases} P_{(\mathrm{i})}(k) & \text{if} \quad k \leq k_{4/5} \\ 0 & \text{if} \quad k > k_{4/5}. \end{cases} \tag{3.2.5}$$

v *Truncated at* $k_{19/20}$ – The fifth power spectrum is obtained by truncating the power spectrum in (i) at $k = k_{19/20}$ such that for $k \leq k_{19/20}$ the $P(k)$ for cases (i) and (v) are identical, while for $k > k_{19/20}$ the (v) power spectrum is $P(k > k_{19/20}) = 0$,

$$P_{(\mathrm{v})}(k) = \begin{cases} P_{(\mathrm{i})}(k) & \text{if} \quad k \leq k_{19/20} \\ 0 & \text{if} \quad k > k_{19/20}. \end{cases} \tag{3.2.6}$$

vi *Oscillatory WDM* – Our last power spectrum is an oscillatory one. This spectrum is inspired by interacting DM [90–92], but we have artificially enhanced the amplitude of the first peak to see if there are any signatures of the oscillation after the nonlinear growth of structure.

All the linear power spectra are shown in Figure 3.1, together with that for standard CDM. Here, we present the matter power spectra at $z = 199$ plotted as $\Delta(k) \equiv k^3 P(k)/(2\pi^2)$. We stress that the power spectra in cases (ii-vi) are not physically motivated but instead are intended to test how changing the shape of the initial linear power spectrum influences the nonlinear evolution of structure.

The linear matter power spectra in Figure 3.1 are used to generate the initial conditions for N-body simulations. As in Chapter 2 we use the 2LPTic code [112] for the ICs at initial redshift $z_{\mathrm{ini}} = 199$. The simulations are performed in a cubic box of comoving length $L = 25\ h^{-1}$Mpc and with $N = 512^3$ particles, using Gadget-2 [113] to evolve the initial perturbations. In this case, we do not include thermal velocities in these simulations because their physical effects are negligible for our choice of WDM candidate masses and N-body parameters (the models satisfy the Jeans mass [143]

and the free-streaming length criteria [141] defined in Section 2.2), and also because including them we introduce extra numerical noise in the simulations, reducing the range of scales we can trust (according to the results in Chapter 2).

3.3 Results from N-body simulations

3.3.1 Matter power spectra

We measure the matter power spectrum from simulations using the code in [175] based on the cloud-in-cell mass assignment scheme and the work [176]. The matter power spectra measured from the ICs are shown in Figure 3.2(a) as symbols, while the lines show the theoretical power spectra. In Figure 3.2(b) we show the ratio,

$$R(k) = \frac{P_{\rm damped}(k)}{P_{\rm CDM}(k)}, \tag{3.3.1}$$

where $P_{\rm damped}(k)$ is the matter power spectrum measured from a simulation of a particular damped model, while $P_{\rm CDM}(k)$ is that measured from the ΛCDM simulation. As we can see, the measured matter power spectra are in good agreement with the theoretical expectations up to the Nyquist frequency. We also note that although the power spectra are very similar at small wavenumbers, they differ appreciably from one another at high wavenumbers, e.g. the ratio between thermal and fantastic WDM at $k \sim k_{1/2}$ is ~ 0.75 and reaches ~ 6 between thermal WDM and the truncated at $k_{1/2}$ power spectra. For the cases of spectra truncated at $k_{4/5}$ and $k_{19/20}$ the deviations start at even smaller wavenumbers.

The situation changes when the ICs are evolved and the system undergoes nonlinear evolution. In Figure 3.3 we plot the matter power spectra ratios (see Eq. (3.3.1)) for (evolved) simulations at redshifts $z = 9, 5, 3, 1, 0$. We can see that the transfer of power from large to small scales progressively reduces the differences between CDM and the various damped scenarios and the difference between the $P(k)$ in the different damped models themselves decreases in time. Indeed, at $z = 0$ for all the spectra, except for the most extreme truncation at $k_{19/20}$, the relative difference

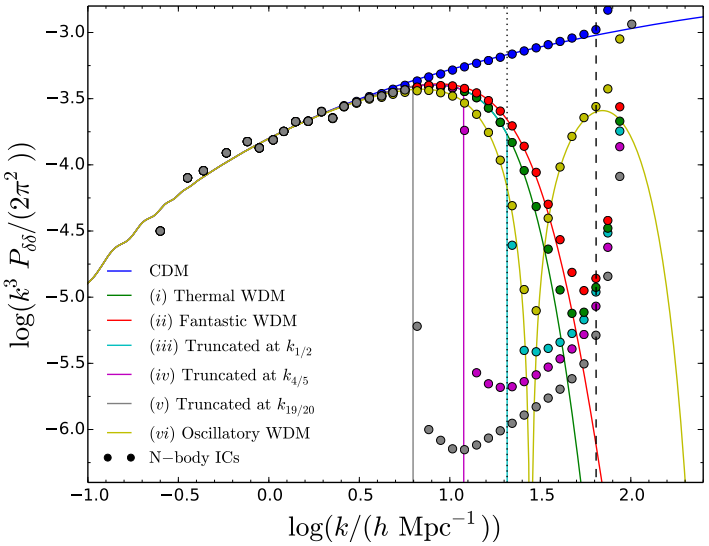

(a)

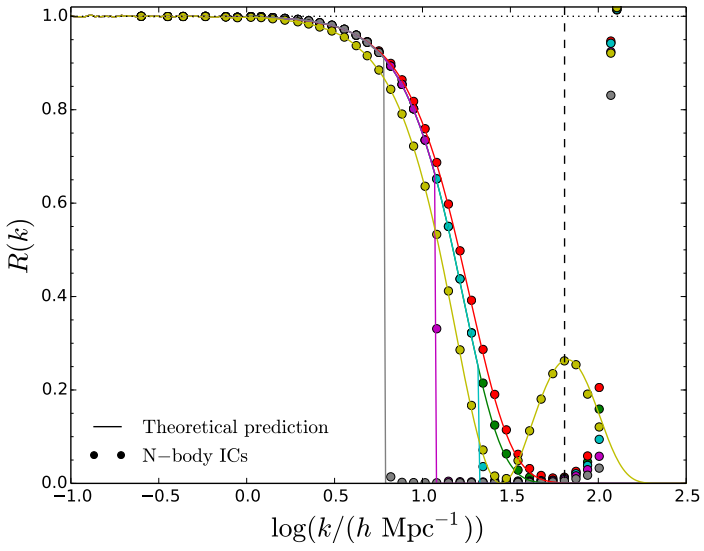

(b)

Figure 3.2: (a) Initial linear matter power spectra generated at $z = 199$. The symbols represent the matter power spectra measured from the ICs. The black vertical dotted line represents the half-mode wavenumber $k_{1/2}$ for the thermal WDM power spectrum (green curve). (b) Ratios of damped power spectra at $z = 199$ relative to that from CDM, see Eq. (3.3.1). The black dashed line in both panels indicates the Nyquist frequency of the simulations. The colour scheme is the same as used in Figure 3.1

between each damped spectrum respect to the thermal WDM one is always less than $\sim 1.2\%$ over all the scales resolved by the simulations. We find also that the differences between the power spectrum for the model truncated at $k_{19/20}$ and the other damped power spectra become progressively smaller at lower redshifts (they

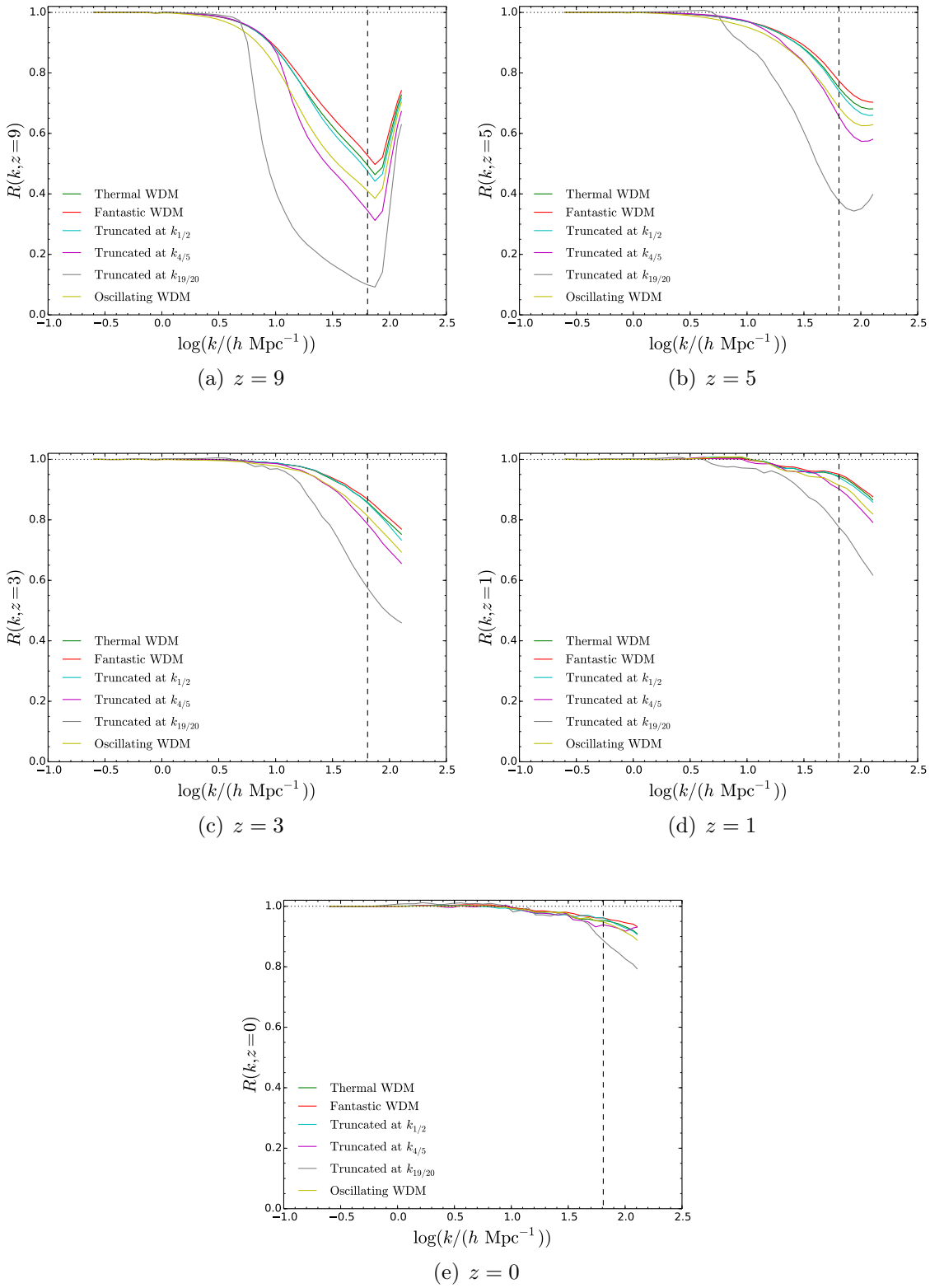

(a) $z = 9$ (b) $z = 5$

(c) $z = 3$ (d) $z = 1$

(e) $z = 0$

Figure 3.3: Ratios of matter power spectra measured from simulations with damped fluctuations with respect to those measured from a CDM simulation. Each panel shows a different redshift as labelled. The black vertical dashed line displays the Nyquist frequency of the simulations.

never exceed $\sim 8\%$ at $z = 0$) and the differences are pushed to higher wavenumbers.

The oscillatory pattern in the linear power spectrum of the oscillatory WDM, the first peak of which is well resolved in the N-body ICs (see Figure 3.2), is washed away during the nonlinear evolution; we can see in Figure 3.3 that no trace of it remains at late times. This suggests that the nonlinear power spectrum cannot be used to distinguish between models with damped fluctuation spectra, such as warm and interacting dark matter.

3.3.2 Halo mass function

The story is different when we look at the halo mass function. This quantity is more sensitive to the initial conditions and the form of the linear theory power spectrum than the evolved power spectrum at late times and, indeed, we find appreciable differences in the halo catalogues extracted from N-body simulations of different damped models. In this case, as a definition of the halo mass, we use the mass, M_{200}, contained in a sphere of radius r_{200}, within which the average density is 200 times the critical density of the universe at the specified redshift. As in Chapter 2, the (differential) halo mass function is presented as $F(M_{200}, z) = \mathrm{d}n/\mathrm{d}\log(M_{200})$.

In Figure 3.4 we show the ratios between the damped and CDM halo mass function at $z = 0$ extracted from the simulations. As we can see, the six damped spectra give rise to halo mass functions which are noticeably different from one another and from CDM. For example, the ratio between the measured halo mass function from a thermal WDM model and scenario in which the initial power spectrum is truncated at $k_{19/20}$ is around a factor of 8 at a halo mass of $M_{200} \sim 10^{10}\, h^{-1}\, \mathrm{M}_{\odot}$. This is remarkable as the ratio in the nonlinear matter power spectra between the two models at $z = 0$ never exceeds ~ 1.08 (see previous subsection). Similar conclusions are reached for the other damped models, although for them the differences in the halo mass function with respect to the thermal WDM case are less pronounced.

As final remark (and as found in Section 2.5), for $M_{200} < 10^{9}\, h^{-1}\, \mathrm{M}_{\odot}$, the halo catalogues measured from N-body simulations of damped models are dominated by

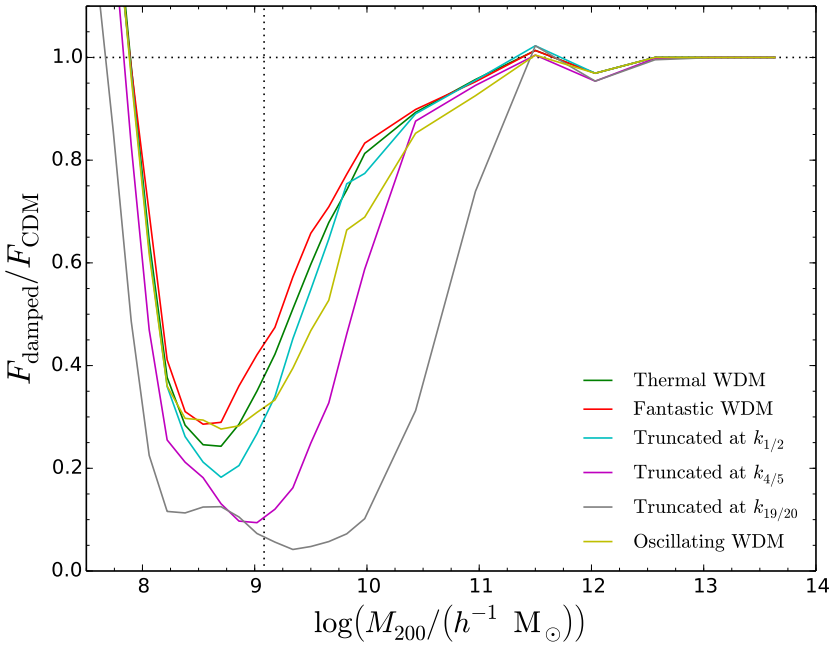

Figure 3.4: Ratios of the halo mass function measured from N-body simulations at $z = 0$ for the various damped models (as labelled) respect to that of CDM. The black vertical dotted line represents the half-mode mass for the thermal WDM model, $M_{\rm hm} = (4\pi/3)\,\bar{\rho}\left(\pi/k_{1/2}\right)^3$, where $\bar{\rho}$ is the mean density of the universe and $k_{1/2}$ is the half-mode wavenumber of the thermal WDM $P(k)$.

spurious haloes. We will present the results for cleaned catalogues of these damped models in Chapter 4.

3.4 2-parameter transfer function

In [75], the authors proposed an analytical parametrisation for the power spectrum which is flexible enough to match the linear theory matter power spectra for a wide range of nCDM models discussed in the literature (e.g. non-resonantly and resonantly produced sterile neutrinos, sterile neutrinos from scalar decay, ultra-light axions, etc). The mathematical form of this parametrization is identical to that used for thermal WDM (see Eq. (2.3.3)). However, unlike the thermal WDM case, the three parameters $\{\alpha, \beta, \gamma\}$ are not related to one another and are left free (hereafter we call the parametrization introduced by [75] the 3-parameter transfer function).

In the previous section we saw that after the nonlinear evolution of structure the

shape of the linear power spectrum for $k > k_{1/2}$ becomes unimportant in determining the nonlinear power spectrum at intermediate and low redshifts. Moreover, if two linear spectra differ minimally at $k \gtrsim k_{1/2}$, we find no appreciable deviation in the halo mass function predicted by the models (as will be confirmed below). So, since the full shape of the linear matter power spectrum is irrelevant from the point of view of structure formation[2], we can ask if the number of free parameters in the parametrisation found in [75] can be reduced if we are interested only in the form of the power spectrum for $k \leq k_{1/2}$. Indeed, out of the three parameters γ is the one which controls the slope of $T(k)$ for $k > k_{1/2}$ [75], so it seems reasonable to reduce the number of parameters by fixing the value of γ. Here, we fix γ such that it is equal to the value in the case of thermal WDM, i.e. $\gamma = -5/\nu$ with $\nu = 1.12$. Our parametrisation will then read

$$T(k) = \left(1 + (\tilde{\alpha}k)^{\tilde{\beta}}\right)^{-5/\nu}, \tag{3.4.1}$$

where $\{\tilde{\alpha}, \tilde{\beta}\}$ are the new free parameters. This new parametrisation has only two free parameters (hereafter we call it the 2-parameter transfer function). The two new parameters $\{\tilde{\alpha}, \tilde{\beta}\}$ are in general different from the old ones $\{\alpha, \beta\}$. This is because although γ is mostly responsible for the shape of the transfer function at $k > k_{1/2}$, it also makes some contribution to $T(k)$ at $k \leq k_{1/2}$. So, in order to capture the slope of the 3-parameter transfer function at small wavenumbers, the free parameters in the new parametrisation need to be different from the old $\{\alpha, \beta\}$. We show below that this new parametrisation is able to match very well the 3-parameter fitting function for $k \leq k_{1/2}$.

We fit the 2-parameter transfer function against some of the 3-parameter transfer functions presented in [75] using a least-squares approach and requiring that the

[2]We agree that our results are strictly true only for linear theory $P(k)$ with $k_{1/2}$ around or larger than the values considered here. This means that our results may not apply in the case of linear $P(k)$ with half-mode wavenumbers smaller than those considered here. However, we note that e.g. a thermal WDM matter candidate with $m_{\rm WDM} < 2$ keV is strongly disfavoured by the current Lyman-α constraints [132, 133]. So, our results can be considered to be general in the sense that they can be applied to all the damped models which are not already ruled out by astrophysical constraints.

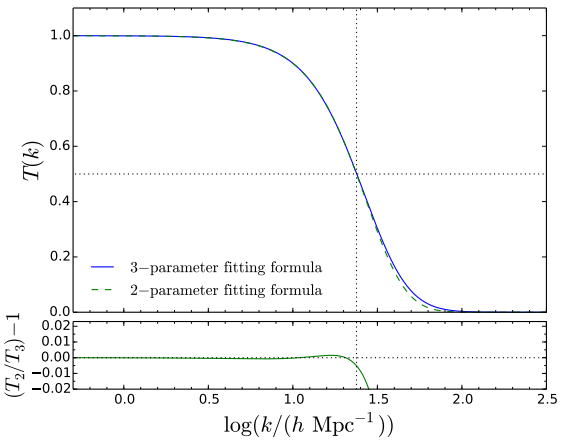

(a) Resonantly produced (I), transfer functions

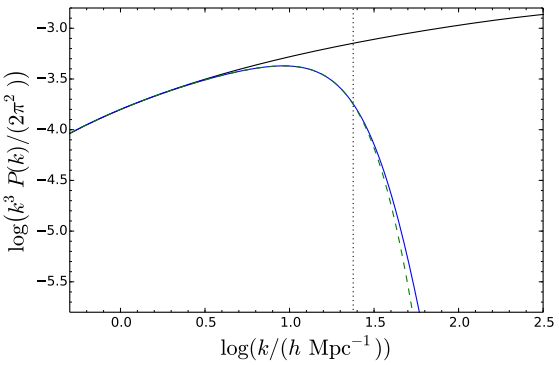

(b) Resonantly produced (I), power spectra

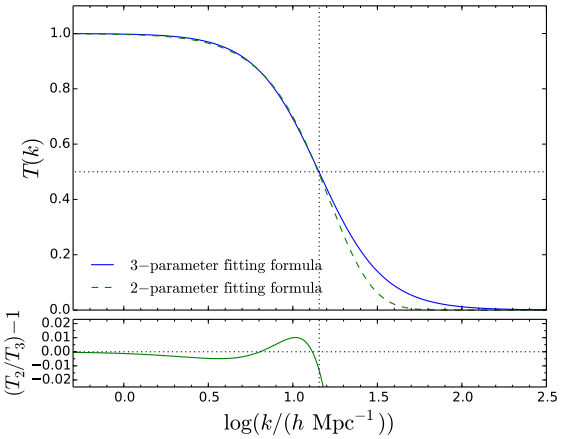

(c) Resonantly produced (II), transfer functions

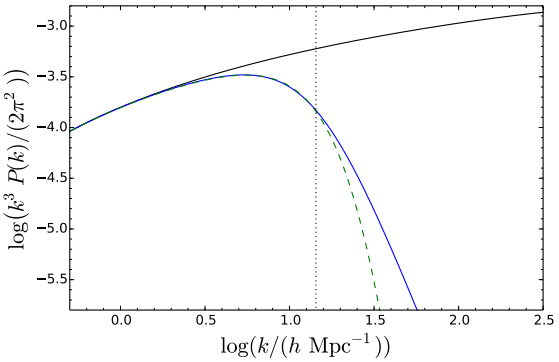

(d) Resonantly produced (II), power spectra

Figure 3.5: Transfer functions (left) and power spectra (right) generated using the values in Table 3.1 for the 3-parameter (solid blue) and 2-parameter (dashed green) transfer function. The bottom panels of the figures on the left show the relative differences between the two parametrisations. The vertical dotted line indicates the half-mode wavenumber $k_{1/2}$.

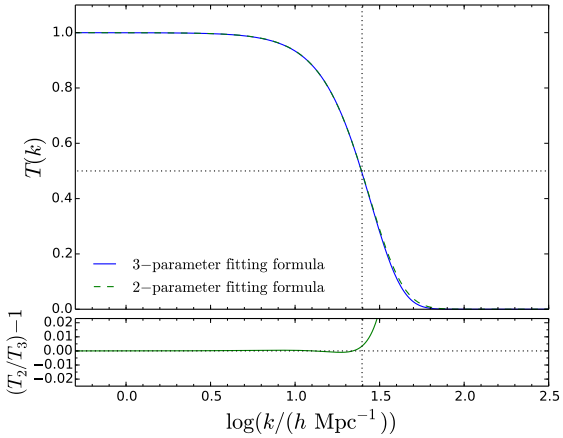

(a) Scalar decay, transfer functions

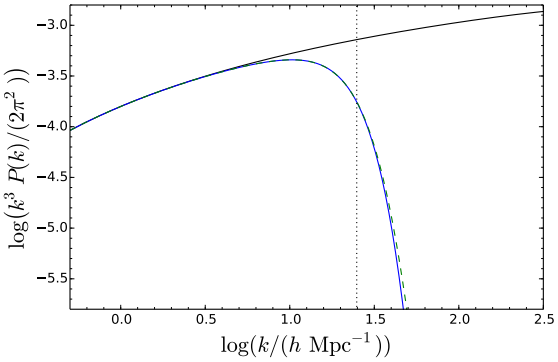

(b) Scalar decay, power spectra

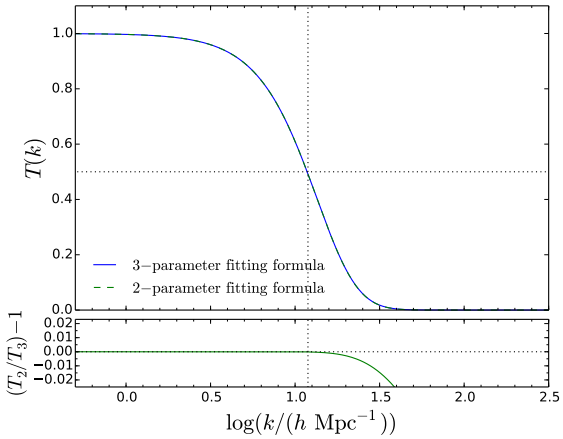

(c) Non-resonantly produced, transfer functions

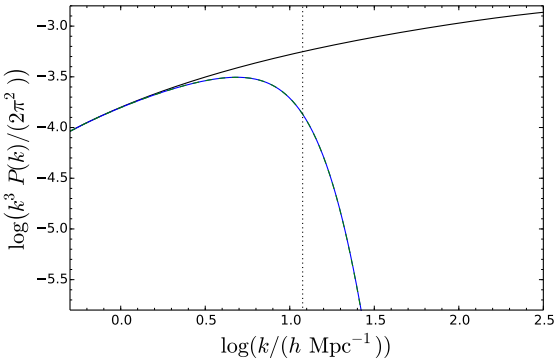

(d) Non-resonantly produced, power spectra

Figure 3.6: Transfer functions (left) and power spectra (right) generated using the values in Table 3.1 for the 3-parameter (solid blue) and 2-parameter (dashed green) transfer function. The bottom panels of the figures on the left show the relative differences between the two parametrisations. The vertical dotted line represents the position of the half-mode wavenumber $k_{1/2}$.

Model	3-param. transfer function α, β , γ	2-param. transfer function $\tilde{\alpha}$, $\tilde{\beta}$
Resonantly Produced (I)	0.025, 2.3, −2.6	0.019, 2.250
Resonantly Produced (II)	0.071, 2.3, −0.98	0.029, 2.029
Scalar Decay	0.016, 2.6, −8.1	0.021, 2.637
Non-resonantly produced	0.038, 2.2, −4.4	0.037, 2.199

Table 3.1: Values of the three parameters $\{\alpha, \beta, \gamma\}$ found in [75] and of our two parameters $\{\tilde{\alpha}, \tilde{\beta}\}$ for the transfer function of the models listed in the first column.

best-fit is obtained for $k \leq k_{1/2}$, while it does not matter if the two parametrisations diverge at higher wavenumbers. In Table 3.1, we show how the values of the parameters found in [75] for a 3-parameter transfer function change when using our 2-parameter function. The plots of the transfer functions for the models in Table 3.1 are shown in Figures 3.5 and 3.6. In these plots, we show the transfer functions on the left and the corresponding linear power spectra on the right. As shown in these figures, our parametrisation matches very well the parametrisation in [75] for $k \leq k_{1/2}$, and only at high wavenumbers do the two formulae diverge. Indeed, looking at the relative differences $T_2/T_3 - 1$ (bottom panels in Figures 3.5 and 3.6), where T_2 and T_3 refer to the 2- and 3-parameter transfer functions respectively, for $k \leq k_{1/2}$ the transfer functions agree to better than 1%.

To confirm that our parametrisation is sufficiently accurate to study DM models from the point of view of structure formation, we choose one of the above examples (the one called "resonantly produced (I)" in Table 3.1) and use N-body simulations to evolve the ICs generated at $z = 199$ generated using both the parametrisations. The simulations are performed in a cubic box of length $L = 25h^{-1}$ Mpc using $N = 512^3$ particles. The matter power spectra measured from the ICs are shown in Figure 3.7, which captures the small differences between the two parametrisations at $k > k_{1/2}$. However, when the system evolves, these differences are reduced and become negligible at late times. Indeed, in Figure 3.8(a), where we display the ratio P_2/P_3 between the evolved power spectra obtained from 2- and 3-parameter transfer functions, we see that e.g. at $z = 9$ the differences are washed out and the two power spectra are identical. This is true also for lower redshifts which are not shown here.

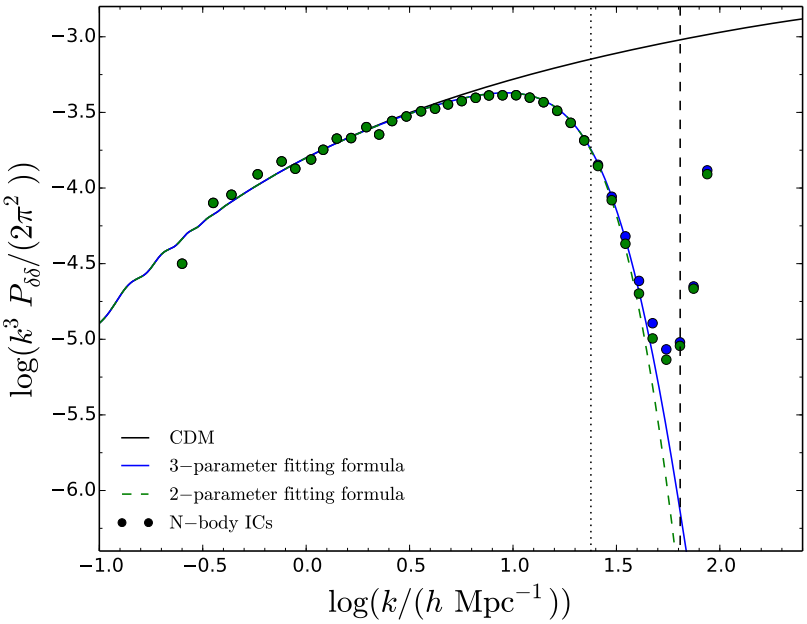

Figure 3.7: Initial linear matter power spectra generated at $z = 199$ for resonantly produced (I) (see Table 3.1) using 3-parameter (blue) and 2-parameter (green) transfer function. The symbols represent the matter power spectra measured from the ICs. The black vertical dotted line represents the half-mode wavenumber $k_{1/2}$, while the black vertical dashed line is the Nyquist frequency of the simulation.

In Figure 3.8(b), we show the ratio of the halo mass functions at $z = 0$ measured from the two simulations with respect to that from the CDM simulation. In this case also there are no appreciable differences between the two parametrisations.

In conclusion, reducing the number of free parameters required to describe the damped linear theory power spectra by neglecting the high wavenumber behaviour of the transfer function does not introduce any appreciable deviations in the nonlinear matter power spectrum and the halo mass function with respect to the results coming from the full 3-parameter transfer function (at least for linear $P(k)$ with $k_{1/2}$ similar or above those considered here). This means that our parametrisation is able to capture the interesting features of a linear matter power spectrum from the point of view of structure formation.

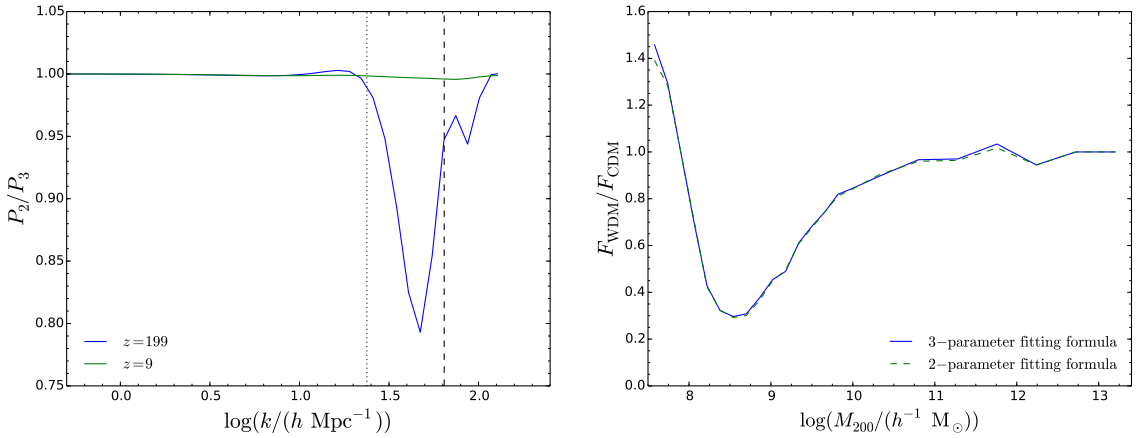

Figure 3.8: (a) Ratios between the matter power spectra coming from the 2- and 3-parameter transfer function (as labelled) measured from N-body simulations at redshift $z = 199$ and 9. (b) Ratios of the halo mass function measured from N-body simulations at $z = 0$ for both of the parametrisations (as labelled) with respect to that in CDM.

3.5 Summary and conclusions

In damped models, the slope of the linear power spectrum and the position of the cut-off strictly depend on the particular model considered. However, nonlinear evolution of structure transfers power from large to small scales, reducing the differences between different damped models at later times and power spectra with different slopes can yield the same cosmological structure.

We have investigated how much information is retained at late times from the initial linear power spectrum following the nonlinear growth of structure. We found that at late times when the system has undergone nonlinear evolution, the shape of the initial linear theory power spectrum above the half-mode wavenumber $k_{1/2}$ is irrelevant for determining the form of the nonlinear power spectrum. Two models, whose linear power spectra are identical at small wavenumbers and differ only for $k > k_{1/2}$, will produce identical evolved power spectra at late times. On the other hand, some differences can be still seen in the halo mass function even at $z = 0$. We found that this quantity is more sensitive to the linear matter power spectrum, so potentially it can be used to detect variations in the linear theory power at wavenumbers $k \gtrsim k_{1/2}$. However, if two linear power spectra are very similar to one

another around $k_{1/2}$ (so no big jumps near or above $k_{1/2}$), the deviations in the halo mass functions for such models are negligible.

Motivated by our results, we have reduced the number of free parameters in the 3-parameter analytic fitting formula given in [75] to parametrise a damped linear power spectrum. Indeed, we have shown that a 2-parameter transfer function (which matches extremely accurately the 3-parameter transfer function at $k \leq k_{1/2}$, but which gives rise to different linear spectra at higher wavenumbers) is capable of capturing the main features of a damped model (such as nCDM) in structure formation. In particular, the halo mass function (which is more sensitive to variations in the linear theory power) seems to be unaffected by this change in the parametrisation.

We conclude that although damped models come from very different underlying physical models, if two models are characterised by linear power spectra which are very similar below the half-mode wavenumber, the results in terms of structure formation are similar. This limits what we can hope to learn about the mechanisms that occurred in the early Universe by measuring cosmic large-scale structure. Nevertheless, this simplifies the work of finding constraints on the impact of damped models of structure formation, because results coming from a particular model can be easily generalised to other models with similar linear power spectra at small wavenumbers.

Chapter 4

A new smooth-k space filter

4.1 Introduction

A common impact of the models studied in the previous chapter on structure formation is a reduction in the halo abundance at low masses. Analytical approaches, such as Press-Schechter (PS) [177–180], that predict halo statistics, need to be modified from those used in standard ΛCDM, in order to predict the downturn in the halo mass function at low masses in damped scenarios. The common way to achieve this is to change the filter used to smooth the matter distribution from a spherical top-hat in real space (generally used in standard ΛCDM) to a sharp-k space filter [143, 181] (see also [178]).

In this chapter, we show that when applied to damped scenarios (especially those with abrupt truncations of the linear spectra above some wavenumber) the PS approach with a sharp-k space filter fails to reproduce the behaviour of the halo mass function measured in N-body simulations at low masses. We present a solution to this problem by introducing a new filter function which gives better agreement with the simulation results than the sharp-k space filter.

The linear damped power spectra considered in this analysis are those presented in Chapter 3 plus a new spectrum (which we call "funny inflation") and the seven power spectra are shown in Figure 3.1 of Chapter 3. The matter power spectrum

from the funny inflation model (see case (vii) in Figure 3.1) is generated using as input a primordial power spectrum that is damped on small scales. This damping can be achieved by considering particular inflaton models [66–72]. Here, we use the parametrisation adopted in [72] for a suppressed primordial spectrum,

$$P_{\rm damp}^{\rm prim} = P_{\rm st}^{\rm prim}\left[\frac{1+10^{-\alpha}}{2} - \frac{1-10^{-\alpha}}{2}\tanh\left(\log\frac{k}{k_s}\right)\right], \tag{4.1.1}$$

where $10^{-\alpha}$ describes the power suppression and k_s is the wavenumber at which the suppression appears. We choose $\alpha = 1$ and $k_s = 5\,{\rm Mpc}^{-1}$. We use CLASS to obtain the matter density fluctuations starting from this damped primordial spectrum. We note that the form of this power spectrum is similar to that of a mixed DM model [134], which means that the results obtained in the next sections for this spectrum are expected to be also valid for mixed DM models. The N-body simulations used to compare the results from the PS approach are those previously described in Section 3.2

The rest of the chapter is organised as follows. In Section 4.2 we introduce the standard PS approach together with a description of the sharp-k space filter. In Section 4.2 we also show how this filter is not accurate enough for some of the models studied here. Section 4.3 is devoted to the introduction of our new filter function (which we call the smooth-k space filter). Some results using our filter are presented in Section 4.4.

4.2 Press-Schechter analytical approach

Some aspects of the non-linear evolution of structure can be captured using analytical methods. The well known PS approach is used to predict some important characteristics of structure formation, such as the halo mass function [177–179]. This method is based on the simplified assumption that if the initial density contrast in a spatial region is larger than some threshold so that the region collapses to a singularity by redshift z, then this region corresponds to a halo that formed and virialised

at z [177] (for a review see [180]). The threshold can be calculated using a spherical or elliptical collapse model [179].

In this approach, the starting point to calculate the differential halo mass function is given by

$$\frac{dn}{d\log(M)} = \frac{1}{2}\,\frac{\bar{\rho}}{M}\,f(\nu)\frac{d\log(\nu)}{d\log(M)}, \tag{4.2.1}$$

where n is the halo number density, M is the halo mass and $\bar{\rho}$ is the average density of the universe. $f(\nu)$ is the first-crossing distribution [178]. Assuming an ellipsoidal collapse model [179], $f(\nu)$ is well approximated by

$$f(\nu) = A\sqrt{\frac{2q\nu}{\pi}}\left(1+(q\nu)^{-p}\right)e^{-q\nu/2}, \tag{4.2.2}$$

with $A = 0.3222$, $p = 0.3$ and[1] $q = 1$. In the above formula, ν is defined to be

$$\nu = \frac{\delta_{c,0}^2}{\sigma^2(R)D^2(z)}, \tag{4.2.3}$$

where $\delta_{c,0} = 1.686$ and $D(z)$ is the linear growth factor normalised such that $D(z = 0) = 1$. $\sigma^2(R)$ is the variance of the density perturbations on a given scale R,

$$\sigma^2(R) = \int \frac{d^3\mathbf{k}}{(2\pi)^3}P(k)\tilde{W}^2(k|R), \tag{4.2.4}$$

where $P(k)$ is the linear matter power spectrum at $z = 0$ and $\tilde{W}(k|R)$ is a filter function in Fourier space. The filter function is not fixed a priori, so it could be chosen to suit the particular cosmological model and power spectrum. In CDM, it is generally chosen to be a top-hat function in real space,

$$W_{\mathrm{Top-Hat}}(x|R) = \begin{cases} \frac{3}{4\pi R^3} & \text{if} \quad x \le R \\ 0 & \text{if} \quad x > R \end{cases}, \tag{4.2.5}$$

[1] We note that although $q = 1$ is expected from a standard ellipsoidal collapse, the authors in [179] observed that the number of the haloes with masses $M > 10^{13}\,\mathrm{M}_\odot/h$ in CDM is underpredicted, so they artificially calibrated the value to $q = 0.707$ to match N-body simulation results. Here we will maintain the standard parametrisation where q is set to unity for two reasons: (1) the volume of our simulations is too small to contain a statistically relevant sample of such massive haloes and (2) when using a sharp-k filter it was shown in [143, 182] that $q = 1$ gives a better match with simulations.

which in Fourier space becomes (see Figure 4.1(a)),

$$\tilde{W}_{\rm Top-Hat}(k|R) = \frac{3\left(\sin(kR) - kR\cos(kR)\right)}{(kR)^3}. \tag{4.2.6}$$

Other choices made in the literature include the Gaussian function and the sharp-k filter (see e.g. [178, 180]). In general, the filter function is associated with a volume, V_W. In the case of a real space top-hat function, the filter in real space describes a sphere of radius R, so the filter volume is $V_W = 4\pi R^3/3$, leading to a straightforward relation between the scale radius R and the enclosed mass $M(R)$ of the virialised object, $M(R) = 4\pi\bar{\rho}R^3/3$. For other filters, there is either no fixed radius in real space (e.g. for the case of a Gaussian filter) or there is a divergent integral (for a sharp-k space filter) [183], so the mass-radius relation is calibrated using N-body simulations [178].

4.2.1 Sharp-k space filter

The PS approach with a real space top-hat filter function works very well for standard ΛCDM (see e.g. [143,147,180–182]), but it predicts an excess of low-mass haloes when applied to models with a cut-off in the power spectrum at small scales [143, 181, 182]. This can be understood using the following argument. If the linear power spectrum $P(k)$ has a cut-off at high wavenumbers, its amplitude decreases faster than that of CDM (i.e. faster than $\sim k^{-3}$). In the limit of small radii R, the variance (see Eq. (4.2.4)) becomes constant (irrespective of the filter used) because the cut-off in the linear power spectrum ensures negligible contributions to the integral from high wavenumbers. However at small radii, the halo mass function predicted by Eq. (4.2.1) varies according to the derivative of the variance [143],

$$\lim_{R\to 0}\frac{dn}{d\log(M)} \propto \lim_{R\to 0}\left(\frac{1}{R^3}\left|\frac{d\sigma^2}{d\log(M)}\right|\right), \tag{4.2.7}$$

whose behaviour strongly depends on the filter used. For a real space top-hat filter function, we find (see also [143]) that $d\sigma^2/d\log(M) \propto R^2$ for $R \to 0$, so Eq. (4.2.7)

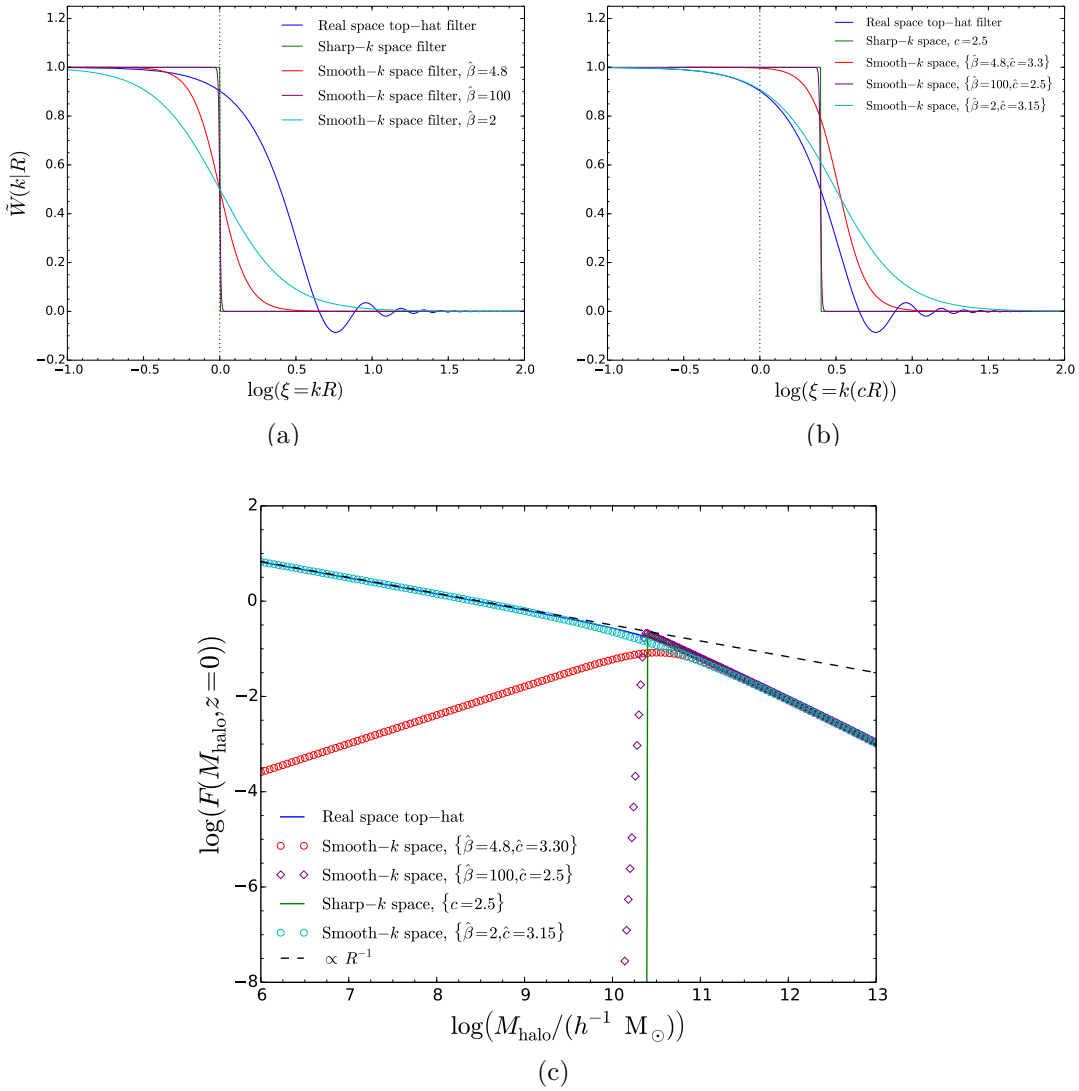

Figure 4.1: (a) Some filters in Fourier space described in Section 4.2 and 4.3 (as labelled by the key). (b) The same as (a) but we have multiplied R by c (or $\hat{c}$) to take into account the differences in the mass definitions for the filters (discussed in Section 4.3). (c) The associated predictions for the halo mass function for the linear power spectrum truncated at $k_{19/20}$ (see case (v) in Figure 3.1). The black dashed line shows the asymptotic behaviour ($\propto R^{-1}$) of the real space top-hat filter at small radii.

goes as

$$\lim_{R\to 0}\left(\frac{dn}{d\log(M)}\right)_{\rm Top-Hat} \propto \frac{1}{R}, \tag{4.2.8}$$

irrespective of the linear $P(k)$ considered. This behaviour is shown in Figure 4.1(c) (note we discuss 4.1(a) and 4.1(b) later), where we show the halo mass function predicted by a top-hat filter for the linear power spectrum truncated at $k_{19/20}$ (case (v) in Figure 3.1), and we also display the asymptotic behaviour of this halo mass function at small radii, i.e. $\propto R^{-1}$. This means that the halo mass function with a top-hat filter diverges at small radii, while it should decrease and become negligible for damped models.

To solve this issue at small masses it was proposed e.g. in [143,181] (see also [178]) to use a sharp-k space filter,

$$\tilde{W}_{\rm Sharp-k}(k|R) = \Theta\left(1 - kR\right), \tag{4.2.9}$$

where Θ is the Heaviside step function (see Figure 4.1(a)). With this filter, Eq. (4.2.1) can be simplified to

$$\left(\frac{dn}{d\log(M)}\right)_{\rm Sharp-k} = \frac{1}{12\pi^2}\,\frac{\bar{\rho}}{M}\,f(\nu)\frac{P(1/R)}{R^3\,\sigma^2(R)}, \tag{4.2.10}$$

and it is interesting to see that for small radii,

$$\lim_{R\to 0}\left(\frac{dn}{d\log(M)}\right)_{\rm Sharp-k} \propto \frac{1}{R^6}P(1/R), \tag{4.2.11}$$

so the halo mass function remains dependent on the linear power spectrum. If $P(1/R)$ goes to zero more rapidly than R^6 for $R \to 0$, the halo mass function becomes negligible at small radii. This is true in general for a damped spectrum, e.g. the linear power spectrum of a thermal WDM candidate at small radii displays the approximate behaviour

$$P_{\rm WDM}(1/R) \sim R^{4-n_s-2\beta\gamma} = R^{24-n_s}, \tag{4.2.12}$$

since $P_{\rm WDM}(k) = P_{\rm CDM}(k)\,T^2(k)$, where $T(k)$ is the transfer function given in Eq. (2.3.3). n_s is the primordial spectral index. For this WDM model, Eq. (4.2.11)

goes as $\sim R^{18-n_s}$ for $R \to 0$. This example can be found in [143]. The sharp-k space filter in real space reads

$$W_{\text{Sharp}-k}(x|R) = \frac{1}{2\pi^2 R^3} \frac{(\sin(x/R) - (x/R)\cos(x/R))}{(x/R)^3}, \tag{4.2.13}$$

and the integral of $W_{\text{Sharp}-k}$ over all space (which defines the volume of W) diverges logarithmically. This means that there is not a well-defined volume in the case of the sharp-k filter, and thus no well-defined mass M associated with the scale R. However, by dimensional analysis M should be proportional to R^3, and so we can write

$$M(R) = \frac{4\pi}{3}\bar{\rho}(cR)^3, \tag{4.2.14}$$

where c is a free parameter to be calibrated using N-body simulations. In [182], it was found that $c = 2.5$ gives the best match between the analytical and the numerical results.

We have compared the analytical predictions at $z = 0$ using PS for the models shown in Figure 3.1 with the (differential) halo mass functions extracted from the N-body simulations (see Section 4.4 for details on how the halo catalogues have been cleaned). The results are summarised in Figure 4.2. The pink lines show the analytical predictions using a sharp-k filter. As we can see, the sharp-k space filter gives reasonably good agreement with N-body results for the four smooth linear power spectra (thermal, fantastic, oscillatory WDM and funny inflation). On the other hand, it fails to reproduce the low-mass behaviour of the halo mass functions extracted from simulations for the three sharply-truncated power spectra. Indeed, the PS approach in the case of a truncated $P(k)$ predicts a step-like transition to zero below some mass scale, while N-body results show a smoother behaviour at small masses.

We can understand why for initial truncated power spectra a sharp-k filter predicts a sharp transition to zero below a certain mass in the halo mass function, by looking at the general behaviour of this filter for small R (see Eq. (4.2.11)). We have constructed a given truncated power spectrum, $P_{\text{trunc}}(k)$, by truncating the

linear thermal WDM spectrum, $P_{\rm therm}(k)$ (case (i) in Figure 3.1), above a certain wavenumber k_t (for the cases analysed here k_t takes the values $\{k_{1/2}, k_{4/5}, k_{19/20}\}$, see Section 3.2 for details). Following this construction, $P_{\rm trunc}(k)$ can be written in general as

$$P_{\rm trunc}(k) = P_{\rm therm}(k)\,\Theta\left(1-\frac{k}{k_t}\right), \tag{4.2.15}$$

so that at $k = k_t$ there is a step-like transition and $P_{\rm trunc}(k) = 0$ for $k > k_t$. Plugging Eq. (4.2.15) in Eq. (4.2.11), we obtain that, for a truncated power spectrum, the analytical halo mass function at small radii behaves as

$$\left(\frac{dn}{d\log(M)}\right)_{{\rm Sharp}-k} \propto \frac{1}{R^6}\,P_{\rm therm}(1/R)\,\Theta\left(1-(R\,k_t)^{-1}\right), \tag{4.2.16}$$

so it has a step-like transition to zero below $R = 1/k_t$, and then for haloes with $R < 1/k_t$ (see Eq. (4.2.14) for the radius-mass relation) the above function is exactly zero.

We note that the above discussion is strictly true only when using linear truncated power spectra (see Eq. (4.2.15)) in Eq. (4.2.11). If, instead of using the linear perturbation theory power spectrum to compute the halo mass function, as is standard practice, we used the non-linear power spectrum (calculated e.g. by using higher-order perturbation theories [184]), the resulting halo mass function with a sharp-k filter could give non-zero values also for haloes with $R < 1/k_t$. However, it is well known that cosmological high-order perturbation approaches are not accurate at wavenumbers larger than $k \sim 0.1\,h\,{\rm Mpc}^{-1}$ and low redshifts, see e.g. [184]. These scales are well below the power spectrum truncation scale considered here, e.g. for the truncated at $k_{19/20}$ power spectrum we have $k_{19/20} \sim 6\,h\,{\rm Mpc}^{-1}$ (see Figure 3.1). Furthermore, in Chapter 3 we found that the non-linear power spectra are remarkably similar to one another at low redshift, see e.g. Figure 3.3, whereas there are clear differences in the halo mass functions (which can be identified with the differences in the linear theory power spectra). Hence, here we will always compute the PS halo mass function by using linear power spectra.

4.3 Smooth-k space filter

Given the above failure to reproduce the halo mass function of a truncated power spectrum, it is interesting to ask if there is some other filter which gives better agreement with N-body simulations. In this section, we show the results of using a new filter function W, which we call the smooth-k space filter. We show below that this new filter gives competitive and, for truncated $P(k)$, better matches to the N-body results than the sharp-k filter.

We start by looking at the general behaviour of the filter functions in Fourier space (see Figure 4.1(a)). As we can see, the asymptotic behaviour of the top-hat and sharp-k filters is $\tilde{W}(\xi \to 0) = 1$ and $\tilde{W}(\xi \to \infty) = 0$, where $\xi \equiv kR$. Moreover, the sharp-k filter has a sudden transition at $\xi = 1$. We smooth this discontinuity (hence the filter name of "smooth-k" space) by replacing the Heaviside step function with a function which is continuous around $\xi = 1$,

$$\tilde{W}_{\mathrm{smooth}-k}(k|R) = \left(1 + (kR)^{\hat{\beta}}\right)^{-1}, \tag{4.3.1}$$

where $\hat{\beta} > 0$ is a free parameter. Two examples of this filter are shown in Figure 4.1(a) corresponding to different choices for the value of the parameter $\hat{\beta}$. Finally, as with the sharp-k filter, we need to find the mass-radius relation for our filter using N-body simulations, so that $M(R) = \frac{4\pi}{3}\bar{\rho}(\hat{c}R)^3$, and $\hat{c}$ is the other free parameter of our model.

This new filter introduces two free parameters, which will be fitted against the results of N-body simulations. The interesting feature of this new filter is that depending on the set of the parameters used, the shape of the new filter can be made to match closely that of other standard filters. For example, in Figure 4.1(c), we show how different filters predict the halo mass function in the truncated at $k_{19/20}$ model (case (v) in Figure 3.1). We can see that if $\{\hat{\beta} = 2, \hat{c} = 3.15\}$, the halo mass function predicted by our filter matches very well that from the real-space top-hat filter (i.e. it goes as R^{-1} at small masses). On the other hand, if $\{\hat{\beta} = 100, \hat{c} = 2.5\}$, the smooth-$k$ space filter prediction displays (almost) the same sharp truncation

predicted by the sharp-k space filter. This characteristic behaviour of the smooth-k space filter can be understood by looking at Figure 4.1(a), where the shape of the filter for different parameter sets is displayed. Indeed, when $\hat{\beta} \to \infty$, the smooth-k space filter becomes a sharp-k space filter, while for smaller $\hat{\beta}$, the width of the step (i.e. the range of ξ where the function is different from zero or unity) in the filter function becomes broader. However, since the smooth-k space with $\{\hat{\beta} = 2, \hat{c} = 3.15\}$ and the top-hat filter are characterised by different mass definitions, in figure 4.1(a) it is not clear why they give the same halo mass function predictions. In figure 4.1(b), we have rescaled the radius R such that for the smooth-k space and sharp-k space filters the new variable $\tilde{R}$ is $\tilde{R} = \hat{c}R$ and $\tilde{R} = cR$ respectively, while maintaining $\tilde{R} = R$ for the top-hat filter. In this way the definition of the enclosed mass for all the filters will be the same, $M(\tilde{R}) = 4\pi/3\,\bar{\rho}\,\tilde{R}^3$. After this rescaling, it is clear that at low ξ the smooth-k filter with $\{\hat{\beta} = 2, \hat{c} = 3.15\}$ and the top-hat filter are very similar to one another, and so they predict similar halo mass functions at low masses.

Concluding this section, we discuss why we expect results from our new filter to be in better agreement with N-body simulations of truncated power spectra than those from using the sharp-k space filter. As we did for the sharp-k space filter, we analyse the behaviour of the analytical halo mass function at small radii for a truncated power spectrum. To do so, we use the asymptotic expression (see Eq. (4.2.7)) for $R \to 0$, which depends on the derivative of the variance $\sigma^2(R)$. For a truncated power spectrum, $P_{\rm trunc}(k)$ (see Eq. (4.2.15)), the derivative of the variance takes the form,

$$\frac{d\sigma^2}{d\log(M)} \propto R \int_0^{k_t} k^2 dk\, P_{\rm therm}(k)\, \tilde{W}_{{\rm Smooth}-k}(k|R) \left| \frac{d\tilde{W}_{{\rm Smooth}-k}(k|R)}{dR} \right|, \qquad (4.3.2)$$

The integral depends on the derivative of the filter function, i.e. on how fast is the transition of the filter function from zero to unity. The width of the region of wavenumbers for which the derivative of $\tilde{W}$ is non-zero depends on the width of the step in $\tilde{W}$, which, in turn, depends on $\hat{\beta}$. The larger the value of $\hat{\beta}$ the steeper the

step is, and so the interval of k where the derivative is non-null is smaller. As long as $R > 1/k_t$ the interval of wavenumbers for which the derivative of $\tilde{W}$ is non-zero always overlaps with the interval of integration, $k \in [0, k_t]$, so that the above integral will always be non-zero no matter how large $\hat{\beta}$ is chosen. On the other hand, when $R < 1/k_t$ (at small masses), the width of the interval of k for which $d\tilde{W}/dR$ is non-null matters. This is because for $R < 1/k_t$ the center of this interval is at high wavenumbers ($k > k_t$). So, if it is not sufficiently broad, the interval of k for which the derivative is non-null possibly has no overlap with the integration interval, and then the above integral would be zero. Indeed, for $\hat{\beta} \to \infty$ the integral is equivalently zero for $R < 1/k_t$, as we found for the sharp-k space filter. On the other hand, if the range of values for which the derivative is non-zero is broader, more wavenumbers in $k \in [0, k_t]$ will contribute to the above integral, enhancing the value of the halo mass function at low masses ($R < 1/k_t$) with respect to the case of the sharp-k space filter. In the next section we will show which parameters of the smooth-k space filter give a sufficient enhancement of the analytical halo mass function at low masses to match the results from N-body simulations.

4.4 Results with the new filter

Before showing the results from our new filter, we briefly discuss the cleaning process adopted here to remove spurious haloes from the halo catalogues extracted from the simulations. We saw in the previous chapters that N-body simulations of damped models display the effects of artificial fragmentation and then some of the haloes at low masses are unphysical, and need to be identified and removed.

An estimate of the mass below which spurious haloes are likely to be found was given in Section 2.5 (see Eq. (2.5.1)). However, not all haloes with masses below this limit are unphysical, and there could be some spurious haloes with masses above this limit. In order to identify haloes which are unphysical, we use the method in [144] to clean the halo catalogues. This method refines the criterion in [169] by

excluding possible unphysical haloes also using the shape of the initial Lagrangian region (proto-halo) from which the simulation particles have evolved to form a given halo at late times. To decide if a halo is genuine or not, this method uses the sphericity of the proto-halo, defined as the ratio between the minor and major axes of the proto-halo region, $s \equiv c/a$. Haloes with sphericity below $s_{\rm lim} = 0.165$ are considered to be spurious [144]. We clean the halo catalogues in our simulations by considering a halo to be spurious (and then removed) if one of these conditions is satisfied:

- the sphericity of the proto-halo is $s < s_{\rm lim}$, or
- the halo mass is $M_{\rm halo} < 0.5\, M_{\rm lim}$.

The results from N-body simulations are displayed in Figure 4.2, where we show the N-body results as symbols: circles are from uncleaned halo catalogues, while crosses represent results after the cleaning. We note that Eq. (2.5.1) depends on the damped $P(k)$ via $k_{\rm peak}$, which is different for different models. So, the lowest mass displayed in the various cleaned catalogues ($0.5\, M_{\rm lim}$) is expected to be different for different initial linear power spectra. The results of using this new filter are shown as black lines in Figure 4.2. We find that the smooth-k space filter with $\{\hat{\beta} = 4.8, \hat{c} = 3.30\}$ consistently gives better matches to the N-body results than the sharp-k space for the models studied here. In the case of truncated spectra, replacing the sharp-k filter with a smoother function smooths the step-like behaviour in the analytical halo mass function and gives much better matches to the simulations as we expect from the discussion in the previous section.

To reinforce our statement that our filter works better in the case of truncated $P(k)$, we have also run simulations with higher resolution for the thermal WDM and truncated at $k_{19/20}$ power spectra. We choose $L = 10\, h^{-1}\,$Mpc and $N = 512^3$ as parameters for the high resolution simulations. The halo mass functions measured at $z = 0$ from these simulations are shown in Figure 4.3. As can be seen from this figure, there is no appreciable difference between the sharp-k and the smooth-k

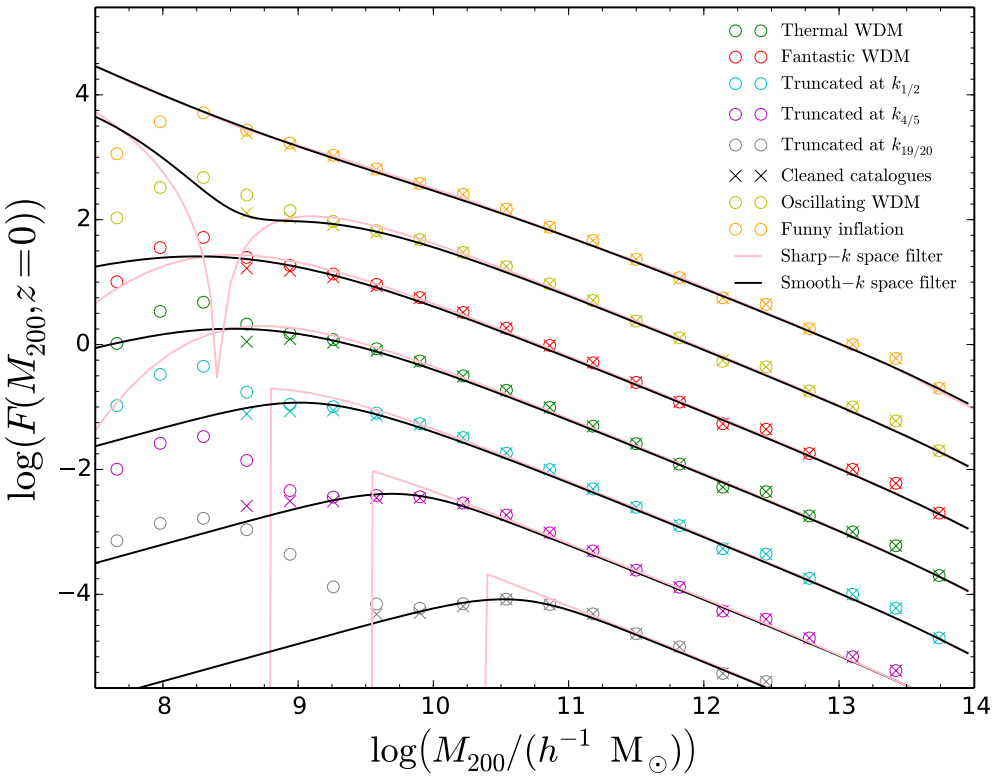

Figure 4.2: Halo mass function at $z = 0$ for various models with damped initial power spectra (as labelled). Circles are results from N-body simulations in a cubic box of length $L = 25\ h^{-1}$Mpc using $N = 512^3$ particles. The lines are the theoretical predictions using two filters: sharp-k space filter (pink) and smooth-k space filter with $\{\hat{\beta} = 4.8, \hat{c} = 3.30\}$ (black). Note that in this Figure all the halo mass functions are shifted above or below the one for the thermal WDM (which is the only one in the right position) to make the results clearer.

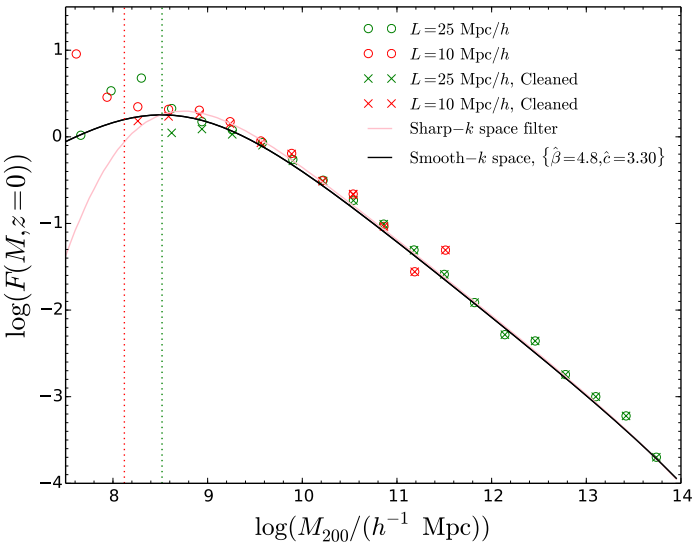

(a) Thermal WDM

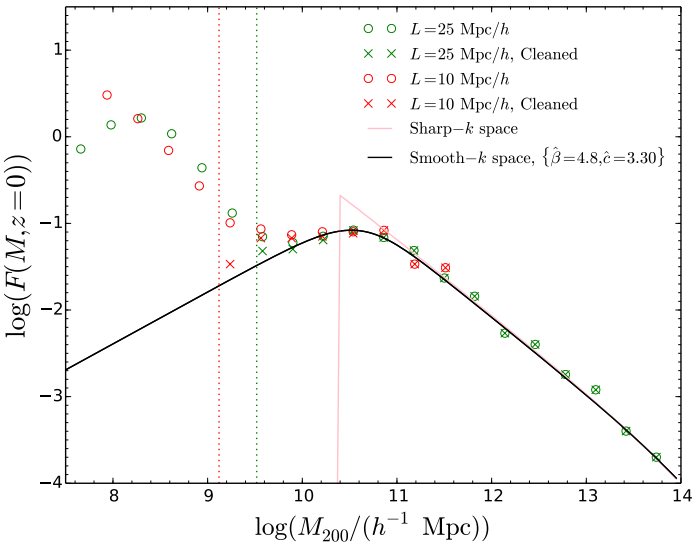

(b) Truncated at $k_{19/20}$

Figure 4.3: Halo mass function at $z = 0$ for (a) thermal WDM and (b) the truncated at $k_{19/20}$ power spectrum model. Circles are uncleaned results from uncleaned catalogues measured from N-body simulations for a cubic box of length $L = 25$ (low resolution, in green) and 10 h^{-1}Mpc (high resolution, in red) respectively, with $N = 512^3$ particles. Crosses represents results from cleaned catalogues. The lines are the theoretical predictions using: sharp-k space filter (pink) and smooth-k space filter with $\{\hat{\beta} = 4.8, \hat{c} = 3.30\}$ (black). The vertical dotted lines show $M_{\rm lim}/2$, with $M_{\rm lim}$ given by Eq. (2.5.1), for the two simulation resolutions (green for the low and red for the high resolution)

.

space filters for the thermal WDM, both filters are in agreement with the N-body results (at least for the masses resolved in our analysis). However, in the case of the truncated at $k_{19/20}$ power spectrum there is an appreciable difference in the halo mass function predicted by the smooth-k space filter with respect to that obtained with the sharp-k space filter, and the former gives a better match to the N-body results. We note also that the high resolution simulation result in the case of the truncated spectrum agrees with the low resolution simulation, i.e. that there are some structures below $R < 1/k_{19/20}$. These structures are clearly physical and not due to numerical noise.

4.5 Summary and conclusions

We have shown that the sharp-k space filter is not accurate enough to reproduce results coming from initial damped power spectra with a sharp truncation at small scales. Indeed, when using the linear power spectrum to calculate halo abundances, the PS approach with a sharp-k space filter predicts no structure at all below some mass scale for these models, while the N-body simulations clearly display some structures. We have presented a solution to this problem via the identification of a new filter function (which we call the smooth-k space filter), which gives always good agreement with the N-body simulations. This new filter has two free parameters, $\{\hat{\beta}, \hat{c}\}$, that have been tuned to give the best match with simulations. Once the halo catalogues have been cleaned, we have found that $\{\hat{\beta} = 4.8, \hat{c} = 3.30\}$ give the best predictions for the halo mass function, and it works very well in predicting the halo mass function for the seven $P(k)$ in Figure 3.1. However, we note that in the case of thermal WDM there are no appreciable differences between the predictions using the smooth-k space and the sharp-k space filter. Both filters predict halo mass functions that are in agreement with N-body results at the mass scales probed by our analysis.

Chapter 5

Thermal inflation and damped matter fluctuations

5.1 Introduction

In the previous chapters, we focused mainly on phenomenological nCDM-like models such as the thermal WDM. In this chapter, we focus instead on the class of non-standard inflation scenarios that introduces a cut-off on small scales in the linear theory power spectrum, with particular attention on models of thermal inflation. Thermal inflation (which feature two inflationary stages) can display damped primordial curvature fluctuations on small scales, producing damped dark matter fluctuations. For a reasonable choice of parameters, thermal inflation models naturally predict a suppression of the matter power spectrum on galactic and sub-galactic scales, mimicking the effect of warm or interacting dark matter.

Historically, thermal inflation was introduced to solve the moduli problem [185, 186]. The moduli are long-lived scalar fields generally present in supersymmetric models. Due to their properties, moduli can dominate the energy density of the Universe for a sufficiently long time to interfere with the epoch of Big Bang Nucleosynthesis (BBN) (this is referred to as the cosmological moduli problem) [187, 188]. Thermal inflation solves this problem by introducing a second, low-energy inflation-

ary period that dilutes the moduli density to harmless values. The second inflation period is induced by a new field (the so-called *flaton*) trapped at its origin by coupling with the thermal bath [185, 186]. Thermal inflation ends when the temperature is no longer sufficiently high to maintain the flaton at $\phi = 0$, so the field rolls toward its minimum and starts to oscillate, giving rise to a flaton matter dominated period. Finally, the flaton decays, ensuring the standard radiation-domination period before BBN.

It was recently pointed out that models of thermal inflation can produce interesting effects on the matter density perturbations [73]. Indeed, in thermal inflation the standard inflationary stage is followed by additional periods that can modify the nearly scale-invariant curvature power spectrum characteristic of the standard ΛCDM paradigm by introducing a damping scale k_b. Modes with $k > k_b$ enter the horizon before (and may exit during) thermal inflation, so they are strongly influenced by the intermediate stages between the first inflation and the radiation dominated period after the flaton decay. It was shown in [73] that the perturbations for $k > k_b$ are strongly suppressed compared with those predicted in the standard ΛCDM paradigm, so the primordial curvature power spectrum for these models presents a damping at high wavenumbers (small scales). In turn, the matter density perturbations are affected, showing a suppression in the CDM power spectrum at $k > k_b$. Thus, these thermal inflation scenarios belong to the class of non-standard inflation models introduced in Section 1.2. We stress that in non-standard inflation models, the matter power spectrum is naturally suppressed at small scales, without requiring modifications of the standard cold dark matter sector. So, in thermal inflation, DM particles are still massive and non-interacting. Thermal inflation can also produce interesting signatures in CMB observables [189] and in the physics of primordial gravitational waves (see e.g. the discussion in [190]). However, here we will focus only on the effects on the matter fluctuations.

As found in [73] the linear matter power spectrum from models of thermal inflation differs from that expected in the standard ΛCDM by the presence of

an enhanced peak in the transfer function at $k \sim k_b$ followed by a damping and oscillations at $k > k_b$. The damping is very similar to that seen in nCDM scenarios. For nCDM models, we have seen in Chapter 3 that the nonlinear evolution of the Universe at low redshifts transfers power from low to high wavenumbers. The non-linear power spectrum is then less affected by the damping, while the halo mass function is more sensitive to the form of the linear power spectrum. We expect that this behaviour is true also for thermal inflation. However, the presence of an enhanced peak and oscillations for $k > k_b$ (which are in general not present in simple thermal WDM scenarios, see e.g. [76,79]) can potentially introduce new features into structure formation that deserve to be investigated in detail, and which could potentially leave signatures of thermal inflation in the large-scale structure of the Universe. In this chapter, we investigate the non-linear evolution of structure formation in the thermal inflation scenario described in [73] by using N-body simulations, highlighting the main differences with respect to the results found in nCDM, other non-standard inflation models and standard ΛCDM. We note that the impact of thermal inflation on structure formation was addressed recently in [190], by e.g. using semi-analytical techniques to calculate dark matter halo abundances. However, we show here that a full study using N-body simulations is necessary to model accurately the non-linear evolution of structure (and to find accurate estimations of the non-linear power spectra and halo abundances at late times). As a second step we compare the N-body results with the Press-Schechter (PS) semi-analytical techniques introduced in Chapter 4 showing the degree of accuracy of these approaches.

This chapter is structured as follows. In Section 5.2 we briefly describe the theoretical model of thermal inflation considered here. In Section 5.3 we show our main results for the non-linear power spectra. Section 5.4 is devoted to the study of halo statistics at $z = 0$, while in Section 5.5 we show the results for halo abundances at higher redshifts. In these sections, we measure the halo mass function from N-body simulations and compare with analytical predictions from the version of the PS approach discussed in Chapter 4. Finally, our conclusions are given in Section 5.6.

5.2 Theoretical model of thermal inflation

In this section we briefly describe the model of thermal inflation and we compare the linear-theory matter power spectrum from this model with two other damped scenarios: the thermal WDM model introduced in Subsection 2.3.1 and a broken scale invariance inflation model. The latter two models are considered because we are interested in quantifying if the results (in terms of structure growth and clustering) from thermal inflation are, in some way, different from those found in other damped models. The linear power spectra for all the models considered here are shown in Figure 5.1(a), while the ratios with respect to ΛCDM are shown in Figure 5.1(b) (in these figures we show also the power spectra measured from the N-body initial conditions at $z = 199$).

5.2.1 Thermal inflation

We consider the model of thermal inflation proposed in [185, 186] and studied in [73] from the point of view of the effects on density perturbations. This model predicts (at least) two inflationary stages. The universe starts as usual with a standard first (or primordial) inflationary period, which produces nearly scale-invariant perturbations and ends at $t = t_e$. However, since moduli acquire non-null vacuum expectation values (VEV) during the first inflation, this stage is followed by a moduli dominated period (moduli are non-relativistic, so in this stage the Universe is matter dominated), starting at $t = t_a$. In this period a sub-dominant standard radiation component is also present. The moduli dominated era ends when their energy density drops below the constant value $V_0 = V(\phi = 0)$ of the flaton potential, maintained at the origin by thermal effects. At this stage, $t = t_b$, the Universe undergoes a second low-energy inflationary expansion, which dilutes the moduli. Thermal inflation finishes when the thermal bath temperature is not sufficient to hold the flaton at $\phi = 0$. The flaton rapidly rolls to its true minimum, starting to oscillate. At $t = t_c$ a flaton matter dominated period begins and a first-order phase transition converts the flaton energy

into standard radiation at $t = t_d$, before BBN. The universe, from this point on, follows the standard history.

Following the convention in [73], we define the characteristic wavenumbers, $k_x \equiv a(t_x)H(t_x)$, with $x = \{a, b, c, d\}$ (where the various times t_x have been introduced in the above paragraph). The numerical values are given e.g. in [190]. In some thermal inflation scenarios (e.g. multiple thermal inflation [186]), the values of k_a and k_b are sufficiently small to be in the range of wavenumbers that are interesting for structure formation. In particular, there are cases when $k_b \ll k_a, k_d$, so the impact of thermal inflation on the curvature power spectrum comes effectively from one parameter, k_b, [73]. In such cases the curvature power spectrum for thermal inflation can be written as [73],

$$\mathcal{P}_{\mathcal{R}}^{\rm TI}(k) = \mathcal{P}_{\mathcal{R}}^{\rm prim}(k)\, T_{\rm TI}^2(k), \tag{5.2.1}$$

where $\mathcal{P}_{\mathcal{R}}^{\rm prim}(k)$ is the (dimensionless) curvature power spectrum from the first inflationary stage, while $T_{\rm TI}(k)$ is the transfer function which contains information about the effects of thermal inflation on the modes with wavenumbers $k > k_b$. The matter power spectrum at a given redshift z is then calculated from the primordial curvature perturbations as $P(k, z) = \mathcal{P}_{\mathcal{R}}^{\rm TI}(k)\mathcal{T}^2(k, z)$, where $\mathcal{T}(k, z)$ is the transfer function that characterises the evolution after the flaton decay.

$\mathcal{P}_{\mathcal{R}}^{\rm prim}$ takes the approximate form (as calculated in [189]),

$$\mathcal{P}_{\mathcal{R}}^{\rm prim} \simeq A_* \left(1 - \frac{1}{N_*} \ln\left(\frac{k}{k_*}\right)\right)^{(1-n_*)N_*}, \tag{5.2.2}$$

where A_* is the amplitude at the pivotal scale k_* and N_* is

$$N_* \equiv \ln\left(\frac{k_e}{k_*}\right). \tag{5.2.3}$$

N_* is uncertain mainly because of the unknown phases before the moduli domination epoch (see [189] for the interval of possible values that can be taken by N_*).

The thermal inflation transfer function $T_{\rm TI}(k)$, takes the analytical form [73],

$$T_{\rm TI}(k) = \cos\left[\left(\frac{k}{k_b}\right)\int_0^\infty \frac{d\alpha}{\sqrt{\alpha(2+\alpha^3)}}\right] + 6\left(\frac{k}{k_b}\right)\int_0^\infty \frac{d\gamma}{\gamma^3}\int_0^\infty d\beta\left(\frac{\beta}{2+\beta^3}\right)^{3/2}\sin\left[\left(\frac{k}{k_b}\right)\int_\gamma^\infty \frac{d\alpha}{\sqrt{\alpha(2+\alpha^3)}}\right]. \tag{5.2.4}$$

The above expression is unity for $k \ll k_b$, and corresponds to an enhancement of $\sim 20\%$ around $k \simeq 1.13\, k_b$, while for $k \gg k_b$ the transfer function oscillates around zero as $T_{\rm TI}(k) \simeq -\cos(2.23\, k/k_b)/5$.

The primordial curvature power spectrum for the standard ΛCDM paradigm is

$$\mathcal{P}_{\mathcal{R}}^{\rm prim,s}(k) = A_*\left(\frac{k}{k_*}\right)^{n_*-1}, \tag{5.2.5}$$

where the pivotal wavenumber is $k_* = 0.05\,{\rm Mpc}^{-1}$. Three differences arise when comparing the power spectrum from thermal inflation (Eq. (5.2.1)) with that from the standard paradigm (Eq. (5.2.5)):

- a small change in the $\mathcal{P}_{\mathcal{R}}^{\rm prim}$ with respect to $\mathcal{P}_{\mathcal{R}}^{\rm prim,s}$ due to N_* (this difference is k-dependent). However, as shown in [190] the difference due to the choice of N_* is negligible (if compared to the other effects listed below) at $k \lesssim k_b$ for $k_b \geq 1\,{\rm Mpc}^{-1}$, while the range of wavenumbers really affected by N_* are those ($k \gg k_b$, oscillation regime) which are already extremely damped by $T_{\rm TI}^2$ (see Figure 3 or 4 in [190]). So, instead of fixing a value of N_*, from here on we will consider $\mathcal{P}_{\mathcal{R}}^{\rm prim}(k) = \mathcal{P}_{\mathcal{R}}^{\rm prim,s}(k)$;

- an enhancement in the power amplitude at $k \sim k_b$, and

- a strong damping for $k > 3k_b$, with an oscillatory pattern in the power spectrum of thermal inflation ($T_{\rm TI}^2$ oscillates around 1/50 at large wavenumbers).

To calculate the matter power spectrum in thermal inflation, we have used the CLASS code [160,161], providing as input the primordial curvature power spectrum for thermal inflation. The matter power spectra $P(k)$ at $z = 199$ are shown in Figure 5.1 for the two values of the characteristic wavenumber $k_b = 5$ and $3\,{\rm Mpc}^{-1}$ considered

in this analysis, together with that from standard ΛCDM and two other damped models (see below) for comparison. We choose these two values of k_b because they produce a sufficient reduction of the number of haloes with mass $M_{\rm halo} < 10^9\,h^{-1}\,{\rm M}_\odot$ (as we will see in the next sections) to be considered as possible solutions to the missing satellite problem. Larger values of k_b give matter power spectra that are less suppressed and so are very similar to standard ΛCDM at the scales of interest in our analysis, and as pointed out in [73, 189] only $k_b \gtrsim 1\,{\rm Mpc}^{-1}$ is allowed by CMB constraints. As can be seen in Figure 5.1(b), the enhancement at $k \sim k_b$ and the damping at larger wavenumbers influence significantly the shape of the matter power spectrum of thermal inflation when comparing with that from standard ΛCDM, so we will focus on the effect of these two properties on structure formation. We also note that the matter power spectra from thermal inflation are significantly different, in general, from those expected from nCDM (see e.g. the thermal WDM power spectrum in Figure 5.1), because of this enhancement in power at $k \sim k_b$ and the presence of oscillations (although some nCDM scenarios such as axion-like DM [94] or interacting DM [90–93] also display oscillations in the matter $P(k)$).

The thermal WDM model shown in Figure 5.1 was introduced in Subsection 2.3.1. We choose the WDM particle mass $m_{\rm WDM} = 2\,{\rm keV}$ because the corresponding half-mode wavenumber ($k_{1/2,{\rm WDM2}}$) is roughly equal to the half-mode wavenumber ($k_{1/2,{\rm TI5}}$) for the thermal inflation model with $k_b = 5{\rm Mpc}^{-1}$ (see Figure 5.1(b)), so these two models are directly comparable.

5.2.2 BSI inflation

We also compare thermal inflation with another non-standard inflation model, which hereafter we call *broken scale invariance* inflation or BSI. Inspired by the scenario proposed in [74, 191] (which was studied as a viable solution of the small-scale crisis in [66]), we consider a model where the primordial curvature spectrum takes the form $\mathcal{P}_{\mathcal{R}}^{\rm prim}(k) = \mathcal{P}_{\mathcal{R}}^{\rm prim,s}(k)\,T_{\rm BSI}^2(k)$, where $\mathcal{P}_{\mathcal{R}}^{\rm prim,s}$ is the standard ΛCDM primordial

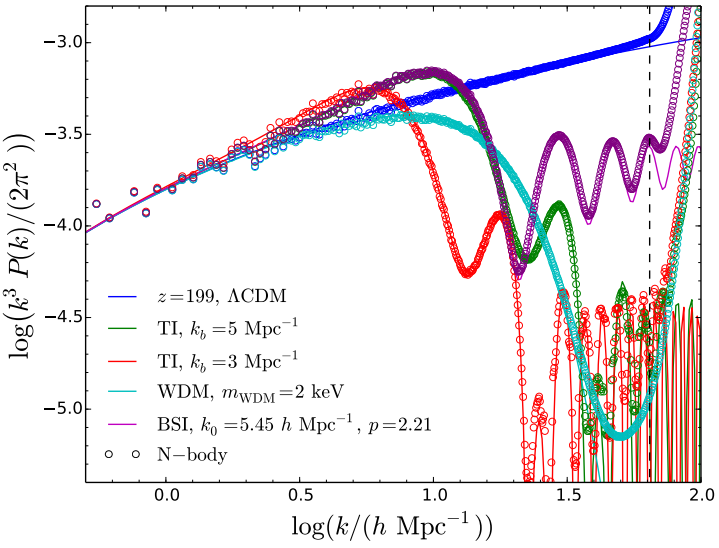

(a)

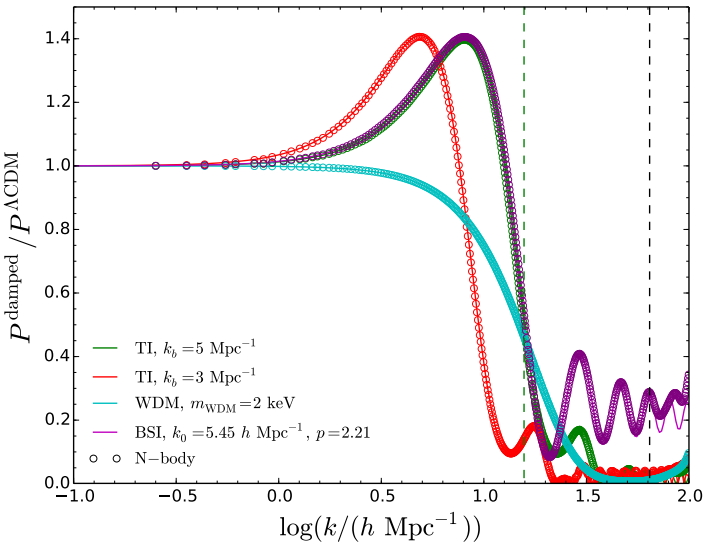

(b)

Figure 5.1: (a) Matter power spectra generated at $z = 199$ for different models as labelled. (b) Ratios of the linear damped power spectra relative to that from standard ΛCDM. Solid lines show the linear theory power spectra, while symbols represent the power spectra measured from the N-body ICs. The black vertical dashed line indicates the Nyquist frequency of the simulations. The green vertical dashed line in panel (b) shows the position of the half-mode wavenumber $k_{1/2,\,\mathrm{TI5}}$ for the thermal inflation matter power spectrum with $k_b = 5\,\mathrm{Mpc}^{-1}$.

spectrum (see Eq. (5.2.5)), while $T^2_{\rm BSI}$ is given by [74]

$$\frac{T^2_{\rm BSI}(k)}{\mathcal{N}_{\rm BSI}} = 1 - 3(p-1)\left(\frac{k_0}{k}\right)\left[\left(1-\frac{k_0^2}{k^2}\right)\sin\left(\frac{2\,k}{k_0}\right) + \left(\frac{2\,k_0}{k}\right)\cos\left(\frac{2\,k}{k_0}\right)\right]$$
$$+\ \frac{9}{2}(p-1)^2\left(\frac{k_0}{k}\right)^2\left(1+\frac{k_0^2}{k^2}\right)\left[\left(1+\frac{k_0^2}{k^2}\right) + \left(1+\frac{k_0^2}{k^2}\right)\cos\left(\frac{2\,k}{k_0}\right) - \left(\frac{2\,k_0}{k}\right)\sin\left(\frac{2\,k}{k_0}\right)\right], \tag{5.2.6}$$

where k_0 is the wavenumber above which the power spectrum breaks its scale-invariance, p quantifies the power suppression[1] and the normalisation $\mathcal{N}_{\rm BSI}$ is chosen such that $T^2_{\rm BSI}(k) = 1$ for $k \ll k_0$, so at small wavenumbers the BSI power spectrum is equal to that in the standard paradigm. We note that this transfer function has an enhanced peak at $k \sim k_0$, whose amplitude depends on p. As we did for the case of thermal inflation, we have modified CLASS providing the BSI primordial power spectrum as input. In this way, CLASS can calculate the linear theory matter power spectrum for BSI. We choose the free parameters, $\{k_0, p\}$, such that the linear matter power spectrum for BSI has the enhanced peak in the same position and with the same amplitude as the linear $P(k)$ for the case of thermal inflation with $k_b = 5\,{\rm Mpc}^{-1}$. We find that for $k_0 = 5.45\,h\,{\rm Mpc}^{-1}$ and $p = 2.21$, the enhanced peak in BSI linear matter power spectrum is roughly equal to that of thermal inflation with $k_b = 5\,{\rm Mpc}^{-1}$. The linear power spectrum for the BSI model is shown in Figure 5.1. From Figure 5.1(b) the choice of this BSI model to compare with thermal inflation with $k_b = 5\,{\rm Mpc}^{-1}$ is clear. Indeed, the linear matter power spectrum of BSI is very similar to that of thermal inflation with $k_b = 5\,{\rm Mpc}^{-1}$ up to $k \sim 20\,h\,{\rm Mpc}^{-1}$. For larger wavenumbers, the thermal inflation transfer function oscillates around zero, while the BSI $T_{\rm BSI}(k)$ oscillates around a constant non-zero value[2]. However, we note that the power spectrum depends on the squared transfer function. In the case of thermal inflation $T^2_{\rm TI}(k)$ oscillates around 1/50 at high wavenumbers (see Section 5.2) while for BSI $T^2_{\rm BSI}(k) \sim 0.22$. The thermal inflation linear power spectrum is then more suppressed at large wavenumbers than that from BSI.

The linear matter power spectra shown as solid lines in Figure 5.1 are used as input for the N-body simulations. The simulations are performed (using the Gadget-

[1]Note that if $p > 1$ the power is suppressed at high wavenumbers, while if $p < 1$ the power is enhanced at high wavenumbers.

[2]Apart from the enhanced peaks, the differences in the transfer functions at high wavenumbers between BSI and thermal inflation are very similar to those between mixed DM (see e.g. [134]) and pure WDM. Indeed, pure WDM models have vanishing transfer functions at high wavenumbers (see e.g. the thermal WDM power spectrum in Figure 5.1(b)). While, in mixed DM the transfer function reaches a constant non-zero value at high wavenumbers since CDM fluctuations are present on small scales [134].

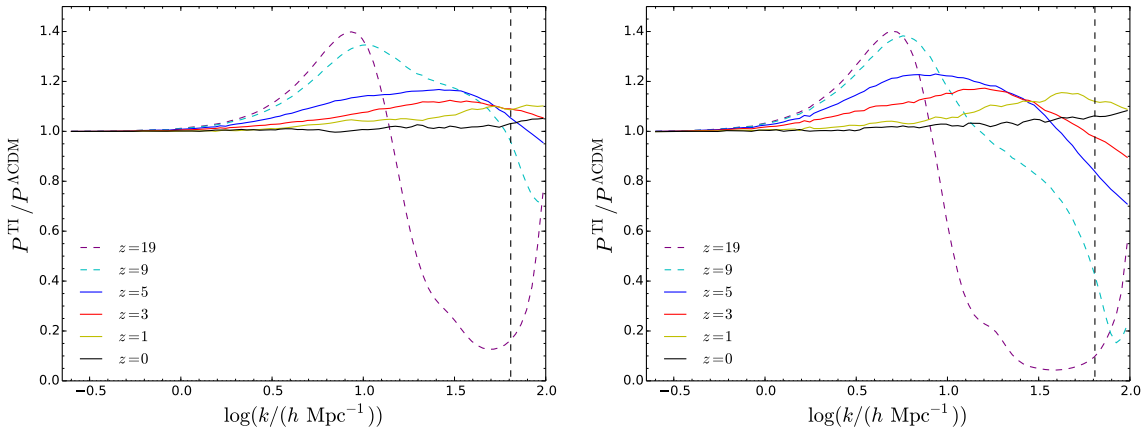

(a) $k_b = 5\,\mathrm{Mpc}^{-1}$ (b) $k_b = 3\,\mathrm{Mpc}^{-1}$

Figure 5.2: Ratios of the matter power spectra measured from N-body simulations of thermal inflation respect to those measured from standard ΛCDM simulations at various redshifts (as labelled). Panel (a) shows the results for thermal inflation with $k_b = 5\,\mathrm{Mpc}^{-1}$, while the results for $k_b = 3\,\mathrm{Mpc}^{-1}$ are shown in panel (b). The black vertical dashed line indicates the Nyquist frequency of the simulations.

2 code) in a cubic box of comoving length $L = 25\,h^{-1}\,\mathrm{Mpc}$ using $N = 512^3$ particles (the simulation particle mass is $\sim 10^7\,h^{-1}\,\mathrm{M}_\odot$). We choose this pair of $\{N, L\}$ because we want to resolve structures on scales near the cut-off of the thermal inflation linear power spectra (see Figure 5.1). We have tested the accuracy of simulations with this choice of parameters against possible numerical effects (see Appendix A).

5.3 Matter power spectra

Below we present our results for the matter power spectra measured from the simulations. We show our results for seven redshifts $z = 199$ (initial conditions) and $z = 19, 9, 5, 3, 1, 0$. As in Chapter 3 the matter power spectrum is measured using the code in [175].

Initial $P(k)$ – The matter power spectra measured from the ICs for all the models described in Section 5.2 are shown as symbols in Figure 5.1(a). These are presented normalised as $\Delta^2(k) \equiv k^3 P(k)/(2\pi^2)$. The ratios $P^{\rm damped}/P^{\Lambda{\rm CDM}}$ of the damped power spectra with respect to that from ΛCDM are displayed in Figure 5.1(b) instead. As shown in these figures, the ICs resolve well the cut-off region for all the power

spectra considered in our analysis. It is interesting to note how well the ICs capture the enhanced peak at $k \sim k_b$ and the oscillatory behaviour at $k > k_b$ in the case of the thermal inflation models. Below we will see how the enhancement in the thermal inflation $P(k)$ changes the non-linear power spectrum and if the oscillatory pattern at high wavenumbers survives non-linear evolution.

Evolved $P(k)$ – The matter power spectra at late times for the two thermal inflation models are shown in Figure 5.2. First, we note that the oscillations at high wavenumbers do not survive the non-linear evolution and they are erased at low redshifts, in agreement with what we have found in Chapter 3 for an oscillatory power spectrum. Second, the enhanced peak in the linear power spectra is progressively shifted to higher wavenumbers in the non-linear regime, while the peak height is reduced. By $z = 0$, the thermal inflation $P(k)$ are very similar to the $P(k)$ of the standard ΛCDM at all the wavenumbers probed by our simulations. We note that in the linear regime, the thermal inflation power spectra were extremely suppressed at $k > 3\,k_b$ (see Figure 5.1(b)). However, due to the shift of the peak position to large wavenumbers, the non-linear power spectra for these models show, in general, more power at $k > 3\,k_b$ with respect to ΛCDM. This is true for both the thermal inflation power spectra considered here. For example, at $z = 0$, for the model with $k_b = 5\,\mathrm{Mpc}^{-1}$ we have $P^{\mathrm{TI}}/P^{\Lambda\mathrm{CDM}} \simeq 1.02$, while for the thermal inflation with $k_b = 3\,\mathrm{Mpc}^{-1}$ $P^{\mathrm{TI}}/P^{\Lambda\mathrm{CDM}} \simeq 1.05$ at wavenumber $k \sim 32\,h\,\mathrm{Mpc}^{-1}$. In the linear regime, both thermal inflation power spectra where suppressed by $\sim 1/50$ at $k \sim 32\,h\,\mathrm{Mpc}^{-1}$ with respect to ΛCDM.

Comparison with WDM and BSI – We have also compared the results from thermal inflation with $k_b = 5\,\mathrm{Mpc}^{-1}$ with those from the WDM and BSI models described in Section 5.2. The non-linear power spectra measured from N-body simulations for these models (shown as ratios to standard ΛCDM) are given in Figure 5.3. For thermal WDM, although the non-linear evolution transfers the power from small to large scales, the non-linear power spectra at low z always have less power than the standard ΛCDM $P(k)$, in contrast with what we find for thermal

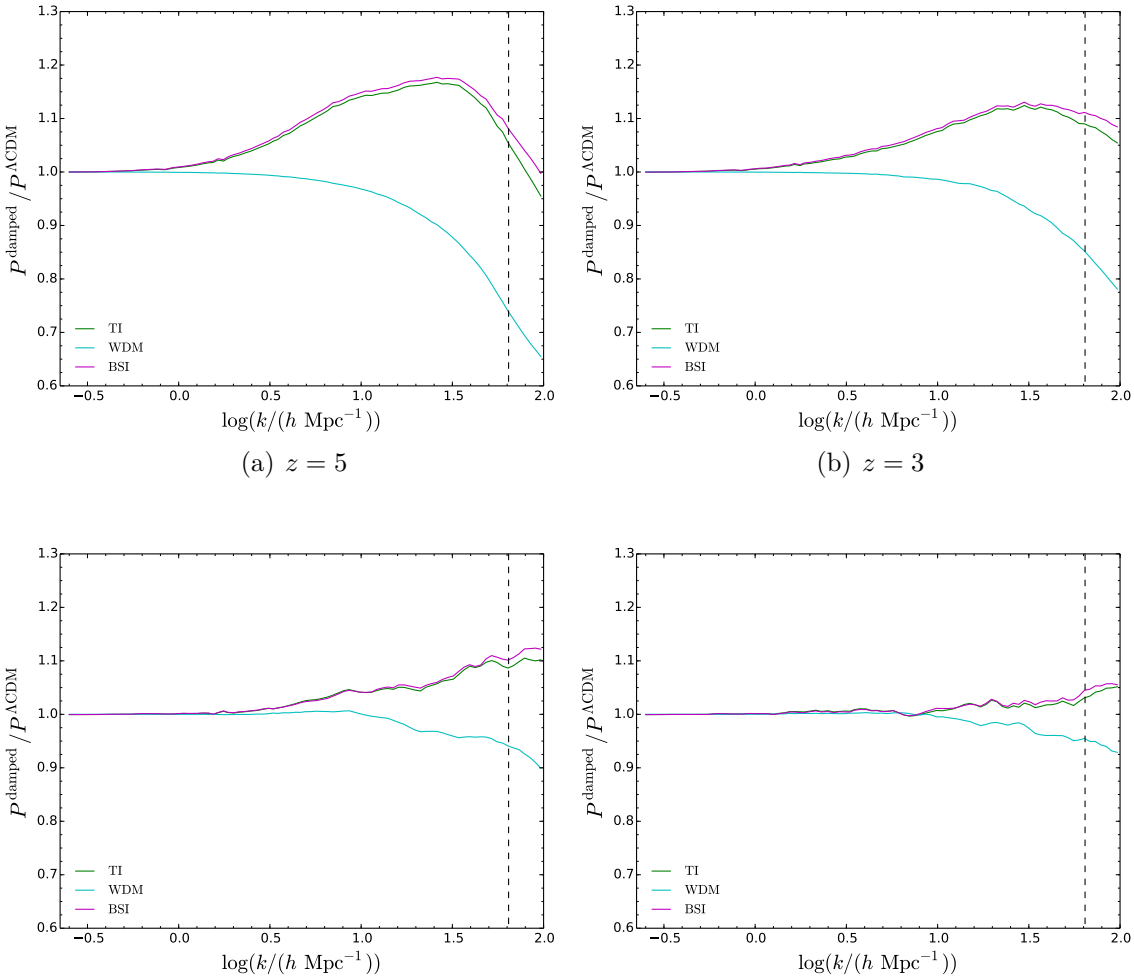

(a) $z = 5$ (b) $z = 3$

(c) $z = 1$ (d) $z = 0$

Figure 5.3: Ratios of the matter power spectra for thermal inflation with $k_b = 5\,\mathrm{Mpc}^{-1}$ (green), thermal WDM (cyan) and BSI (magenta) with respect to those from standard ΛCDM measured from N-body simulations at redshifts $z = 5, 3, 1, 0$ as labelled. The black vertical dashed line indicates the Nyquist frequency of the simulations.

inflationary models (see the discussion in *Evolved P(k)* above). In the case of the BSI model, the non-linear power spectrum behaviour follows that of thermal inflation. Indeed, as can be seen from Figure 5.3 the enhanced peak is reduced in magnitude and shifted by the same amounts for both thermal inflation and BSI. In general, the matter power spectra at low redshift from thermal inflation display less power than BSI. However, the differences in the non-linear matter power spectra at $k \gg k_0, k_b$ between thermal inflation and BSI are appreciably less than those in the linear theory power spectra on the same scales. For example, the ratio between thermal inflation and BSI power spectrum at $z = 199$ (linear theory) is small, ~ 0.09 at

$k \sim k_{\rm Ny}$, while the ratio between the two non-linear power spectra at $z = 0$ is ~ 0.98 for wavenumbers near the Nyquist frequency. The non-linear transfer of power from large to small scales has reduced the initial linear theory difference between these two models by a factor of 10.

In conclusion, non-linear matter power spectra are then a blunt tool to distinguish the effects of thermal inflation or BSI. We will see below that halo statistics are more sensitive to the shape of the linear $P(k)$. We stress, however, that the results regarding the non-linear $P(k)$ have not appeared in the literature before, since previous studies on damping models have always focused on the damping features of the matter power spectra. In thermal and BSI inflation, we find that the presence of an enhanced peak in the linear power spectrum affects substantially the behaviour of the non-linear power spectra at small scales. The non-linear power spectra in these models are then different from those found in nCDM scenarios, particularly at high redshifts.

5.4 Halo statistics at $z = 0$

In this section we explore whether counting the number of haloes of different masses can discriminate between thermal inflation and the standard paradigm. We will see also if the thermal inflation models predict a different halo mass function than thermal WDM and BSI. In this section we focus on results at $z = 0$, we discuss the halo mass function at high redshifts in the next section.

5.4.1 Measured halo mass function

As we saw in the previous chapters, one common impact of damped models on structure formation is a reduction in halo abundance at low masses, offering a possible solution to the missing satellite problem. Since thermal inflation models are characterised by damping in the linear matter power spectrum at high wavenumbers (as seen above), we expect a similar reduction in the number of low-mass haloes

with respect to standard ΛCDM. However, since thermal inflation power spectra are characterised by enhanced peaks, it is also possible to find such features imposed on the halo mass function[3]. In this subsection we show the halo mass function measured from the N-body simulations at $z = 0$ (for halo mass functions at high redshifts see Section 5.5). The (differential) halo mass function is always presented as $F(M_{200}, z) = dn/d\log(M_{200})$. We assume a minimum of 50 simulation particles in a halo, so the minimum halo mass is $\sim 5 \times 10^8\, h^{-1}\,\mathrm{M}_\odot$. We note also that the volume of our simulations is too small to provide a statistically robust sample of haloes with masses $M_{200} > 10^{12}\, h^{-1}\,\mathrm{M}_\odot$. This means that for the most massive haloes in our simulations the results are influenced by large Poisson fluctuations. To identify spurious haloes in thermal inflation, BSI and WDM simulations we adopt the method described in Chapter 4.

The halo mass functions at $z = 0$ extracted from the simulations are shown in Figure 5.4(a) for all the models considered in our analysis. The symbols show the results measured from the halo catalogues once the spurious haloes have been removed. In the lower panels of Figure 5.4 we display the measured halo mass functions (shown as ratios to the ΛCDM) for the damped models before (Figure 5.4(b)) and after (Figure 5.4(c)) the spurious structures have been removed. Comparing Figures 5.4(b) and 5.4(c) we can see that the spurious haloes affect only the low-mass end ($M_{200} < 4 \times 10^9\, h^{-1}\,\mathrm{M}_\odot$) of the halo mass function of the damped models. This is in line with what we found in Chapter 4. We now discuss the cleaned results in more detail starting from the thermal inflation models and then comparing with WDM and BSI.

Thermal inflation – As we can see from the plots of the ratios with respect to ΛCDM (lower panels in Figure 5.4), for both thermal inflation models the halo mass function has the following behaviour: (i) it approaches the ΛCDM predictions

[3]These features in thermal inflation cosmologies have been found in [190] by inferring the halo mass function by using the analytical PS approach. We review this approach in the next subsection by showing that using a spherical top-hat filter the PS analytical predictions over-estimate the small mass halo abundance when compared with N-body simulations.

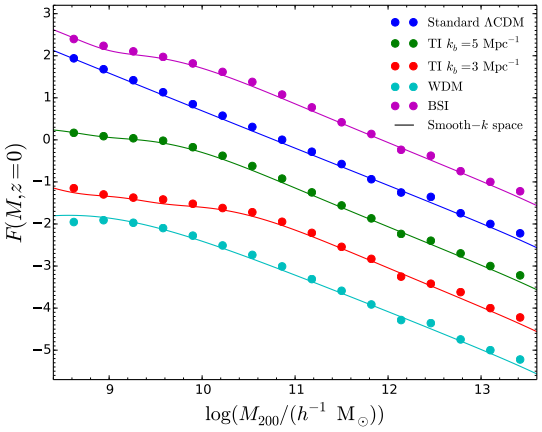

(a)

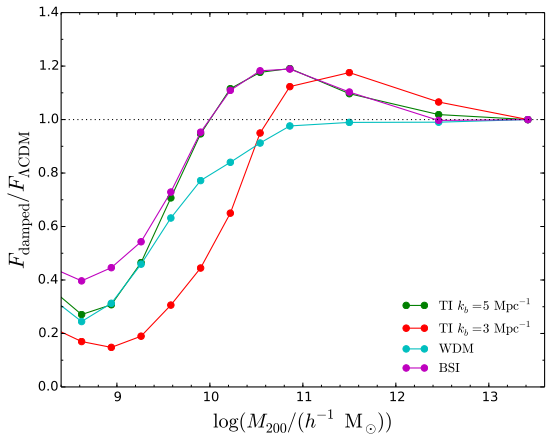

(b) Uncleaned catalogues

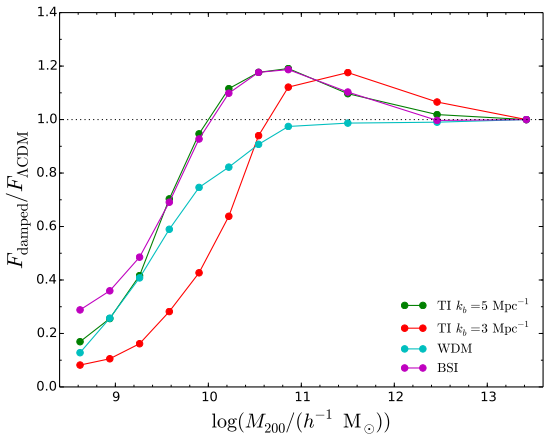

(c) Cleaned catalogues

Figure 5.4: (a) Halo mass function at $z = 0$ for all the models considered here (as labelled). Symbols show the results from cleaned catalogues extracted from N-body simulations and cleaned using the method explained in the text. Lines show the results obtained using the PS analytical approach with the smooth-k space filter. Note that in (a) all the halo mass functions are shifted above or below that for thermal inflation for presentation purposes. Lower panels: ratios of the halo mass function for the damped models with respect to that for ΛCDM from (b) uncleaned and (c) cleaned halo catalogues respectively. Note that in the lower panels we have reduced the number of bins in the mass range $\log(M/(h^{-1}\,\mathrm{M}_\odot)) \in [11.2, 13.8]$ to suppress fluctuations due to Poisson noise.

at large halo masses, (ii) has an enhancement ($\sim$ 17% larger than ΛCDM) at intermediate mass scales (i.e. $M_{200} \sim 3 \times 10^{10}\, h^{-1}\,\mathrm{M}_\odot$ for $k_b = 5\,\mathrm{Mpc}^{-1}$ and $M_{200} \sim 1.5 \times 10^{11}\, h^{-1}\,\mathrm{M}_\odot$ for $k_b = 3\,\mathrm{Mpc}^{-1}$) and (iii) becomes much smaller than the ΛCDM results for lower halo masses. This behaviour follows that of the linear matter power spectrum presented in the previous section (this can be seen more clearly when using analytical approaches to calculate the halo mass function, see next subsection).

Comparison with WDM and BSI – Here, we compare the halo mass function at $z = 0$ for thermal inflation with $k_b = 5\,\mathrm{Mpc}^{-1}$ with that from N-body simulations of thermal WDM and BSI inflation. As can be seen in Figure 5.4, the differences in the behaviour of the halo mass function among these three damped models follow those in the linear power spectrum (see Figure 5.1) than those in the non-linear spectrum. Indeed, at intermediate mass scales ($M_{200} \sim 10^{10}\,h^{-1}\,\mathrm{M}_\odot$) the thermal inflation and BSI halo mass functions have an enhancement with respect to ΛCDM while thermal WDM always displays halo abundances equal to or lower than standard ΛCDM. At lower masses, thermal inflation and WDM display roughly the same downturn. In the case of BSI, the halo mass function at $z = 0$ is very similar to that of thermal inflation for halo masses $M_{200} > 1.5 \times 10^9\,h^{-1}\,\mathrm{M}_\odot$. However, at low halo masses ($M_{200} < 1.5 \times 10^9\,h^{-1}\,\mathrm{M}_\odot$), the halo mass function for BSI is less suppressed than that measured in the thermal inflation model.

We note that from our N-body results (see Figure 5.4) it seems that the ratio between the BSI and ΛCDM halo mass function is close to a constant value (which is also confirmed by the analytical predictions, see next subsection) instead of decreasing further as in thermal inflation. However, we note that our simulations cannot resolve accurately mass scales $M_{200} < 5 \times 10^8\,h^{-1}\,\mathrm{M}_\odot$, so higher resolution simulations would be needed to confirm the existence of this plateau at small halo masses in the BSI model with respect to ΛCDM. This different behaviour of the halo mass function at small halo masses for BSI and thermal inflation is expected from the differences at large wavenumbers in the linear power spectra of these two models. Indeed the BSI transfer function follows that of thermal inflation up to $k \sim 20\,h\,\mathrm{Mpc}^{-1}$. However, at larger wavenumbers, the BSI transfer function does not decrease further and oscillates around a constant non-zero value, as discussed in Section 5.2 (see e.g. Figure 5.1).

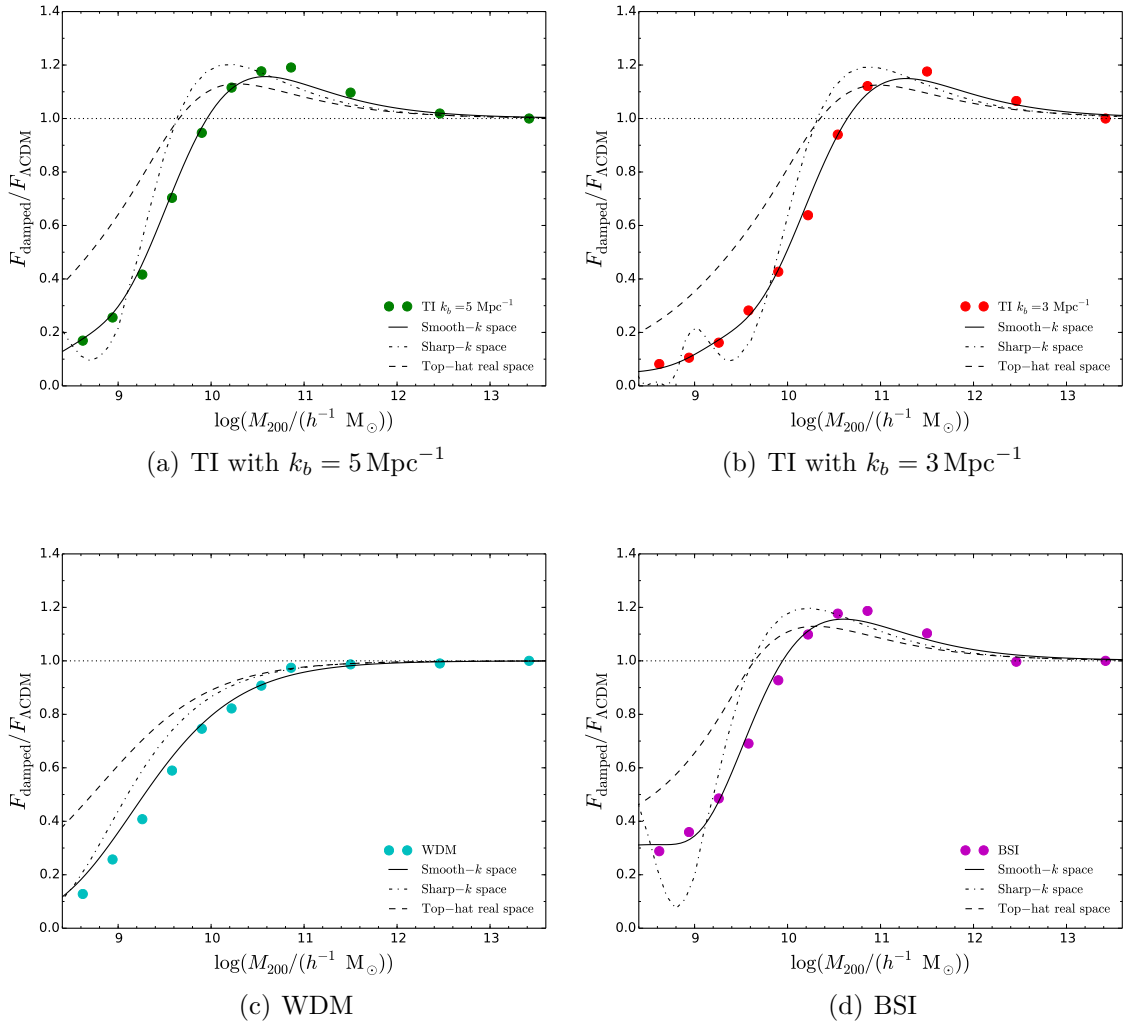

(a) TI with $k_b = 5\,{\rm Mpc}^{-1}$ (b) TI with $k_b = 3\,{\rm Mpc}^{-1}$

(c) WDM (d) BSI

Figure 5.5: Ratios of the halo mass function at $z = 0$ for the damped models with respect to that for ΛCDM. Symbols show the results from cleaned halo catalogues, while black lines show the results for the analytical PS approach with: smooth-k space (solid), sharp-k space (dashed-dotted) and top-hat real space (dashed) filter respectively.

5.4.2 Analytical predictions

As discussed in Chapter 4, some aspects of the non-linear evolution of structure can be captured using semi-analytical methods, such as the PS analytical approach. We test here which of the three filters (top-hat real space, sharp-k space and smooth-k space) introduced in Chapter 4 gives the best match to the halo abundances extracted from N-body simulations (note that we choose the same free-parameters as in Chapter 4 for the smooth-k and sharp-k space filters). In Figure 5.5, we display as lines the results using the three filters (symbols show the results from N-body simulations).

From all the panels in this figure we can see that the smooth-k space filter gives better matches than the other two filters for all the models considered here (in particular the top-hat real space filter predicts an excess in the halo abundance at small halo masses of a factor of ~ 4 larger than that actually measured from simulations). Moreover, the smooth-k space filter predicts reasonably well the position of the enhancement in the halo mass function of both thermal inflation models and BSI (with deviations $< 5\%$ in the ratios). In the case of BSI, we can also see that the ratio with respect to ΛCDM predicted by our filter reaches a constant non-zero value at small halo masses. However, as pointed out in the previous subsection, our simulations cannot resolve properly these mass scales, so high-resolution simulations are needed to confirm such behaviour. We can extend the conclusions found in Chapter 4 by noting that the smooth-k space filter is still a good choice when considering models of thermal inflation or BSI (at least for mass scales well resolved by our simulations). Here we have only considered two thermal inflation models. However, at least for all thermal inflation models with $k_b \geq 3\,\mathrm{Mpc}^{-1}$, our filter is expected to give good predictions. This is because such models are equally or less damped (more similar to ΛCDM) at the wavenumbers probed by our analysis than those considered here, so the halo abundances are less reduced at the scales relevant for structure formation.

5.5 Halo statistics at high redshifts

In the previous section we presented the halo abundances at $z = 0$. However, in [190] the authors show that the magnitude of the peak in the halo mass function for thermal inflation models increases at high redshifts. In this section we investigate this aspect by measuring the halo mass function from our N-body outputs at redshifts $z = 5, 3, 1$ and compare them with the analytical predictions from the PS approach with the smooth-k space filter.

As in the case of $z = 0$, halo catalogues from simulations at higher z need to be cleaned from spurious haloes. However, our method of cleaning (considered in

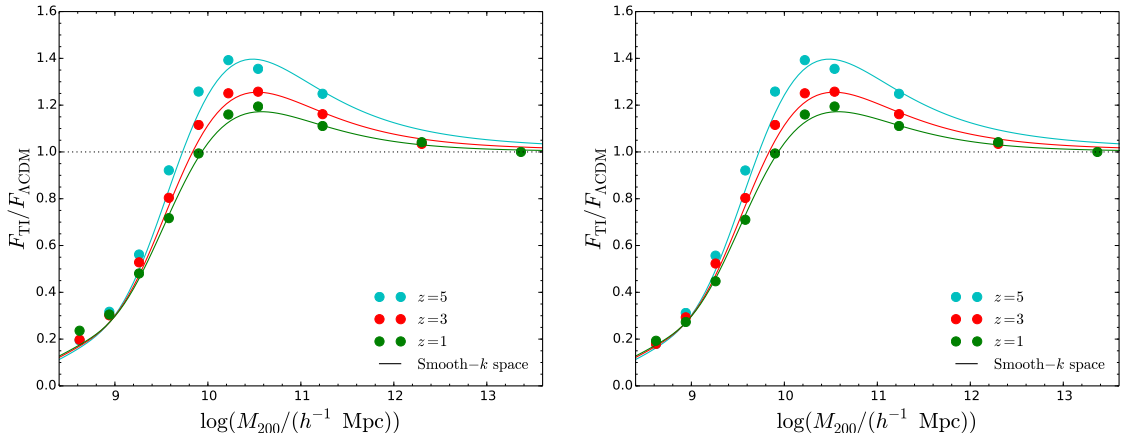

(a) Uncleaned catalogues (b) Cleaned catalogues

Figure 5.6: Ratios of the halo mass function for the thermal inflation with $k_b = 5\,\mathrm{Mpc}^{-1}$ with respect to that for ΛCDM at different redshifts as labelled. Symbols show the results from (a) uncleaned and (b) cleaned halo catalogues. Lines show the results for the analytical PS approach with the smooth-k space filter.

Chapter 4) uses the value in [144], $s_{\rm lim} = 0.165$, for the sphericity limit, which is valid only for halo catalogues at $z = 0$. For higher redshifts, one needs to find the appropriate sphericity limit (see e.g. the discussion in [147]). Since the purpose of this section is to understand the evolution of the enhanced peak with z, we will not undergo a thorough study on finding the sphericity limit at $z > 0$. Instead, we use a conservative estimation of the spurious haloes at high redshifts based on the haloes removed in catalogues at $z = 0$. This method is illustrated below.

For a given halo catalogue at $\tilde{z} \neq 0$, we first remove all the haloes with masses $M_{\rm halo} < 0.5\,M_{\rm lim}$. This is justified because we found in Chapter 2 that the upturn in the halo mass function due to the spurious haloes appears at roughly the same masses irrespective of the redshift. To remove further spurious haloes among those remaining after this first cleaning step, we proceed as follows. We identify all the simulation particles belonging to spurious haloes at redshift $z = 0$ (they are identified using the cleaning process explained in Chapter 4). We call these particles "spurious" particles, just because they are in spurious haloes at $z = 0$. We locate the position of the spurious particles at $\tilde{z}$ and find if these particles are bound in haloes at this redshift. If an halo at $\tilde{z}$ contains more than 70% of these spurious particles, we

consider this halo as spurious and we remove it from the catalogue.

In Figure 5.6 we show the halo mass function extracted from our simulations of thermal inflation with $k_b = 5\,\mathrm{Mpc}^{-1}$ at high redshifts (the uncleaned catalogue results are shown in Figure 5.6(a), while the cleaned ones are in Figure 5.6(b)). From this figure we see that although the position of the enhancement in the ratio with respect to the ΛCDM remains almost invariant with the redshift, its magnitude increases with z. Indeed, at $z = 1$ $F_{\rm TI}/F_{\Lambda\rm CDM} \simeq 1.19$ for masses $M_{200} \simeq 3\times10^{10}\,h^{-1}\,\mathrm{M}_\odot$, while it increases to $\simeq 1.25$ at $z = 3$ and reaches $\simeq 1.40$ at $z = 5$ and for the same mass bin. We note that the differences in the halo mass function near the peak between $z = 1$ and $z = 0$ (see Figure 5.5(a) for the results at $z = 0$) are instead smaller, with an enhancement in the latter of around $F_{\rm TI}/F_{\Lambda\rm CDM} \simeq 1.17$ at $M_{200} \sim 3 \times 10^{10}\,h^{-1}\,\mathrm{M}_\odot$ (to be compared with $F_{\rm TI}/F_{\Lambda\rm CDM} \simeq 1.19$ at $z = 1$). In Figure 5.6, we show also the predictions from the PS approach with the smooth-k space filter. Although the smooth-k space filter parameters were calibrated using halo statistics at $z = 0$ (see Chapter 4), we can see that this filter gives reasonably accurate predictions of the halo mass function at high redshifts.

5.6 Summary and conclusions

In this chapter, we have studied how structures grow in the thermal inflation models described in [73] by using N-body simulations. These models are characterised by a matter power spectrum which is damped on small scales but with a peak in the power (compared to ΛCDM) located at a wavenumber just below the damping scale. The N-body simulations used here were performed in a cubic box of length $L = 25\,h^{-1}\,\mathrm{Mpc}$ using 512^3 simulation particles, the simulation particle mass is around $10^7\,h^{-1}\,\mathrm{M}_\odot$. We have investigated two thermal inflation models with $k_b = 5\,\mathrm{Mpc}^{-1}$ and $k_b = 3\,\mathrm{Mpc}^{-1}$ respectively. The N-body results from such models have been compared with those from thermal WDM, BSI and standard ΛCDM model. The thermal WDM model has been chosen with the same half-mode wavenumber as

in thermal inflation with $k_b = 5\,\mathrm{Mpc}^{-1}$. In the case of the BSI inflation, we have constructed the model to have an enhanced peak at the same position and of the same magnitude as that in thermal inflation with $k_b = 5\,\mathrm{Mpc}^{-1}$. However, at large wavenumbers the linear $P(k)$ for BSI is less suppressed than that from thermal inflation.

For each model, we have measured the non-linear power spectrum and the halo mass function from the N-body simulation outputs at different redshifts. We summarise below the main results. Regarding the nonlinear power spectrum, our findings can be summarised as follows.

- The peak in the linear power spectrum for both thermal inflation models persists in the nonlinear regime, but is shifted to higher wavenumbers and has a reduced amplitude at progressively lower redshifts.

- Although the thermal inflation linear $P(k)$ for $k > 3\,k_b$ is suppressed by a factor $\sim 1/50$ with respect to ΛCDM, due to the peak shift, the non-linear power spectrum at low redshifts is enhanced at these wavenumbers with respect to that in ΛCDM. At $z = 0$, the ratio w.r.t. the ΛCDM is of the order of unity for all the wavenumbers $k < k_{\mathrm{Ny}}$, where k_{Ny} is the Nyquist frequency of our simulations. This is true for both thermal inflation models considered here.

- The WDM non-linear power spectrum behaves differently than that from thermal inflation. Indeed, we find that although the transfer of power enhances the power at small scales, the non-linear power spectra at low z always have less power than the standard ΛCDM $P(k)$.

- The BSI non-linear power spectrum shows similar behaviour to that in thermal inflation. Indeed, the peak in BSI is shifted to higher wavenumbers and has a reduced amplitude at low redhsifts as in the case of thermal inflation with $k_b = 5\,\mathrm{Mpc}^{-1}$. In the linear regime, $P_{\mathrm{TI}}/P_{\mathrm{BSI}} \sim 0.09$ at $k \gg k_b$. However, the non-liner evolution (almost completely) washes out the differences at large wavenumbers present in the two initial power spectra, so that at low redshifts

the two non-linear power spectra are very similar to each other, e.g. $P_{\rm TI}/P_{\rm BSI} \sim 0.98$ at $k \sim k_{\rm Ny}$.

Regarding the halo mass function, we find the following results.

- In general, the differences in the halo mass function between the different models studied here follow those in the linear matter power spectra (rather than those in the non-linear power spectrum). Indeed, in both the thermal inflation models we find that the halo mass function has an enhanced peak before dropping to negligible values at small masses (as in the case of the linear power spectrum). The BSI and thermal inflation with $k_b = 5\,{\rm Mpc}^{-1}$ halo mass functions are roughly the same for masses $M_{200} > 1.5 \times 10^9\,h^{-1}\,{\rm M}_\odot$. At lower masses, the BSI decreases slower than thermal inflation and eventually reaches a plateau. In the case of WDM, the halo mass function presents no enhancements and is always equal or less than that from the standard ΛCDM model.

- The enhancement in the halo mass function is around $M_{200} \sim 3 \times 10^{10}\,h^{-1}\,{\rm M}_\odot$ for thermal inflation with $k_b = 5\,{\rm Mpc}^{-1}$ and BSI models, while it appears at higher masses, $M_{200} \sim 1.5 \times 10^{11}\,h^{-1}\,{\rm M}_\odot$, for $k_b = 3\,{\rm Mpc}^{-1}$. The enhancement in all these models with respect to the ΛCDM is around $\sim 20\%$ at $z = 0$.

- At higher redshifts and in the case of thermal inflation, we find that the halo mass function has an enhancement at the same mass as $z = 0$. However, the magnitude of this enhancement with respect to ΛCDM increases from $\sim 20\%$ at $z = 0$ to $\sim 40\%$ at $z = 5$.

- We have used these numerical results to test the predictions from the PS approach with three filters: top-hat real space, sharp-k space and smooth-k space. From this analysis, we find that the predictions from a smooth-k space filter agree with the simulation results over the widest range of halo masses. This is true for all the models and at all the redshifts considered here.

We note that here we have considered the simplest WDM model, the so-called thermal WDM. However, as mentioned in Chapter 2 and 3, this model does not exhaust all the possibilities inside the nCDM scenarios. Other well-motivated models, such as sterile neutrinos [80–89], axion-like particles [94–96] or models suggested by effective theory of structure formation (ETHOS) [192, 193], can produce different effects on structure formation than those found in the case of thermal WDM (see e.g. [75, 95, 96, 194, 195] and Chapter 3 of this thesis). We note that our simulations do not take into account the effects of baryon physics that can modify the matter distribution and the properties of haloes measured from DM-only simulations, see e.g. [118, 127, 196–200].

As in nCDM models, the thermal inflation model predicts fewer low-mass haloes and sub-haloes than standard ΛCDM, but without involving any modification to the dark matter sector. However, differently from nCDM, the model presents an enhancement in the power spectrum at wavenumbers just shorter than the damping scale. This is a unique feature in the power spectrum which could leave an imprint on the large-scale structure of the Universe which can be used to distinguish this model from nCDM scenarios. For example, in [190] the authors have shown how future 21-cm observations could be able to distinguish between thermal inflation and WDM because of the different shapes of their power spectra. The recent results from the EDGES experiment [201], which claim a detection of a 21-cm absorption line at $z \sim 20$, could indicate that star formation was happening at high redshifts (an early onset of the so-called cosmic dawn). An early cosmic dawn can be used to constrain the suppression of the matter power spectrum in damped models (as was done e.g. for nCDM models in [202, 203]) and these constraints can be applied to thermal inflation power spectra. Moreover, Lyman-α observations could be used to constrain the values of k_b as was done for the mass of thermal WDM candidates in [132, 133]. Regarding halo abundances, the halo mass function in thermal inflation is characterised by an enhanced abundance at halo masses just above the suppression mass scale, so in principle, these models can be distinguished from nCDM using halo

statistics. Indeed, galaxy probes (see e.g. [204, 205]) at high redshift could be able to give some information on the massive objects near the peak (which is enhanced in magnitude for $z > 0$ as we have found here), while future strong lensing observations (see e.g. [206]) will be able to constrain the number of low-mass DM sub-haloes. Results from these future observations could shed some light on the shape of the underlying matter power spectrum and could indirectly constrain the nature of the processes that produce a damping in the matter fluctuation from very early epochs in the history of the Universe.

Chapter 6

Neutral hydrogen and modified gravity

6.1 Introduction

In the previous chapters, we looked at alternatives to ΛCDM that introduce a cut-off in the matter power spectrum at small scales. We investigated how these alternatives leave features in the non-linear DM structures by measuring e.g. the halo mass function from N-body simulations. In this chapter, we focus instead on the effects of modified gravity (MG) models on structure formation, with particular attention to how future 21 cm intensity mapping experiments in the post-reionisation epoch can be used to probe the nature of gravity.

In recent years, tests of general relativity (GR) on cosmological scales have become possible and commonplace [104] although until now these tests have primarily focused on comparatively high-mass objects and low redshift (see e.g. [207–216]). Nevertheless, due to the screening mechanisms (see below), which many MG models employ to pass stringent Solar System tests, it is challenging to detect deviations from GR in these objects.

In this chapter, we propose a novel test of gravity at intermediate scales and high redshifts using the distribution of neutral hydrogen in our Universe which is

observable in 21 cm experiments. Indeed, 21 cm mapping of neutral hydrogen can be used to trace the underlying matter distribution and clustering [217–220] (as suggested also in [221]). In order to determine how possible deviations from GR would affect the HI distribution, we employ a set of full-physics hydrodynamical simulations of chameleon $f(R)$ modified gravity. Comparing the $f(R)$ simulations to their ΛCDM counterparts allows us to quantify the size of the effects due to MG in the overall neutral hydrogen abundance and the HI power spectrum, and to assess if these effects can be observed with future 21 cm intensity mapping experiments such as SKA [102]. HI clustering has been proposed as a probe for a number of non-standard cosmological models, e.g. massive neutrinos, warm DM, dark energy and modified gravity [222–226], but this study reveals new features and promising constraining power thanks to the high resolution of our simulations.

The chapter is organised as follows. In Section 6.2 we review the MG models chosen for the analysis. In Section 6.3 we describe the hydrodynamical simulation set-up and how we extract information on the neutral hydrogen distribution from these simulations. In Section 6.4 we present the results for the overall neutral hydrogen energy density at different z. In Section 6.5 we show the neutral hydrogen power spectra measured from simulations together with some additional tests, which are aimed to better understand the features found in the MG HI power spectra. Finally, we discuss the implications of our study on HI in Section 6.6

6.2 Chameleon f(R) gravity

The chameleon $f(R)$ gravity is a popular family of MG models that modify the Einstein-Hilbert Lagrangian density by replacing the Ricci scalar R with some function $f(R)$ [105]. In these models, a cosmological constant is still implicitly needed to achieve the late-acceleration expansion [227–229], so they do not offer a real solution to the problems of the cosmological constant. Nevertheless, they represent an interesting opportunity to study the effects of deviations from GR on cosmological

and astrophysical scales.

The action in $f(R)$ gravity is

$$S = \int \mathrm{d}^4x \sqrt{-g} \left[\frac{R + f(R)}{16\pi G} + \mathcal{L}_m \right], \tag{6.2.1}$$

where G is the gravitational constant, g is the determinant of the metric $g_{\mu\nu}$ and $\mathcal{L}_m$ is the matter Lagrangian density. In the cosmological simulations used here (see [108]) all gravity force computations are performed within the Newtonian limit [230]. In this limit, the MG equations from the action (6.2.1) reduce to a modified Poisson equation and an equation for the scalar degree of freedom (the so-called *scalaron* field), $f_R \equiv df(R)/dR$,

$$\nabla^2\Phi = \frac{16\pi G}{3}\delta\rho - \frac{1}{6}\delta R, \quad \nabla^2 f_R = \frac{1}{3}\left(\delta R - 8\pi G\delta\rho\right), \tag{6.2.2}$$

where $\delta\rho \equiv \rho(\mathbf{x}) - \bar{\rho}$ is the matter density perturbation, while $\delta R \equiv R - \bar{R}$ is the Ricci scalar perturbation. These modifications to Newtonian gravity can be considered as a fifth force mediated by f_R. Here, we study the Hu-Sawicki variant [107] of this model, where

$$f(R) = -m^2 \frac{c_1 \left(\frac{R}{m^2}\right)^n}{c_2 \left(\frac{R}{m^2}\right)^n + 1}. \tag{6.2.3}$$

m is given by $m^2 \equiv \Omega_m H_0^2$ and we also choose $n = 1$. In the limit $c_2\, R/m^2 \gg 1$ and for $c_1/c_2 = 6\Omega_\Lambda/\Omega_m$ the scalar function (6.2.3) features an expansion history which is very close to that of a ΛCDM universe. In the above limit and for $n = 1$, we can simplify the expression for the background scalar field, $\bar{f}_R$, as (see e.g. [215])

$$\bar{f}_R = -\frac{c_1}{c_2^2} \frac{1}{\left[\left(\frac{\bar{R}}{m^2}\right) + 1\right]^2} \approx -\frac{c_1}{c_2^2} \left(\frac{m^2}{\bar{R}}\right)^2, \tag{6.2.4}$$

in which,

$$\bar{R} = 3m^2 \left(a^{-3} + 4\,\frac{\Omega_\Lambda}{\Omega_\mathrm{m}}\right) \approx 3m^2 \left(a^{-3} + \frac{2\,c_1}{3\,c_2}\right), \tag{6.2.5}$$

and

$$\frac{c_1}{c_2^2} = -\left[3\left(1 + 4\,\frac{\Omega_\Lambda}{\Omega_\mathrm{m}}\right)\right]^2 \bar{f}_{R0}, \tag{6.2.6}$$

where $\bar{f}_{R0}$ is the background value of the scalaron today. As can be seen from the above equations, the model is fully specified by the value of $\bar{f}_{R0}$.

In order to not violate the very stringent constraints on gravity in our local environment [231], the theory employs the so called *chameleon screening mechanism* [232,233], to suppress modifications to gravity in high density environments, restoring GR within these regions. The characteristic onset of the screening depends on the choice of the free parameter of the theory, $\bar{f}_{R0}$. In $f(R)$ gravity the speed of gravitational wave (GW) is equal to the speed of light and the model passes recent constraints from GW observations [234], making it one of the leading viable alternatives to GR. $f(R)$ gravity models have been widely studied using numerical simulations [213, 235–241], and their effects on structure and galaxy formation are representative for the wider class of chameleon-type MG models.

For our analysis, we consider what we call the F5 and F6 variants of $f(R)$ gravity, where the parameter $\bar{f}_{\rm R0}$ is equal to -10^{-5} and -10^{-6}, respectively. An interesting characteristic of the chameleon screening is that this mechanism becomes inefficient first for small structures and then moves to massive objects and dense environments. This suggests that we should look at low-mass objects, which are less screened and so deviate more from GR, in order to obtain strong constraints in cosmology. However, a major challenge here is the difficulty to accurately detect and trace such objects in observations even at low redshifts. As found in [221] for GR, 21-cm intensity mapping is sensitive to the abundance of haloes down to $10^8\,{\rm M}_\odot$, making it a very promising probe of differences in the low-mass end of the halo mass function (as we will show below in the case of $f(R)$ gravity), without requiring to detect individual haloes.

6.3 Modelling the neutral hydrogen

The 21-cm mapping is based on measuring the 21-cm flux emitted from the hyperfine splitting of the ground state of the neutral hydrogen. If an hydrogen atom is in

the upper energy state, it can decay to the lower state, emitting a photon of rest wavelength $\sim$ 21 cm. Since the neutral hydrogen distribution, which traces the matter distribution, is inhomogeneous due to the growth of the matter perturbations, it produces fluctuations in the 21-cm signal that can be used to constrain the underlying matter clustering. After re-ionisation, the majority of the hydrogen is in the ionised phase, but in the over-density regions self-shielding effects preserve neutral hydrogen, so the post-ionisation signal gives information on the clustering of collapsed haloes [217–221].

In order to understand how modifications to standard gravity affect the 21 cm signal, we analyse the SHYBONE simulations [108] (introduced in Subsection 1.3.2). They include roughly 2×512^3 resolution elements in $62\,h^{-1}$Mpc side-length simulation box for the F6, F5 and ΛCDM model, reaching a mass resolution of $m_{\rm DM} = 1.28 \times 10^8\,h^{-1}M_\odot$ for DM-particles and roughly $m_{\rm gas} = 2.5 \times 10^7\,h^{-1}M_\odot$ for gas cells. The simulation suite features also DM-only N-body counterparts for the runs, which will be used here to assess the differences in the halo mass function between hydrodynamical and N-body simulations.

To calculate the neutral hydrogen fraction in each simulated gas (Voronoi) cell, we follow the prescription in [221]. For non star-forming gas, we use the distinction between ionised and neutral hydrogen calculated on-the-fly in the simulations and that is included in the outputs. For star-forming gas, we instead post-process the outputs, recalculating the equilibrium neutral hydrogen fraction in each cell using the approach in [242] (and reviewed below).

We derive the total neutral fraction of hydrogen in ionisation equilibrium for each star-forming cell in post-processing by solving the equation,

$$n_{\rm NH}\,\Gamma_{\rm tot} = \alpha\,n_{\rm e}\,n_{\rm prot}, \tag{6.3.1}$$

where we equate the total number of ionisations with the total number of recombinations per unit time per unit volume. n_i with $i \in \{\rm NH, e, prot\}$ is the non-ionised hydrogen, free electron and free proton number density respectively. α is the recom-

bination rate (the rate at which free electrons and protons combine to form neutral elements), calculated using the approximation proposed in [243],

$$\alpha = 1.269 \times 10^{-13} \frac{\lambda^{1.503}}{\left(1 + (\lambda/0.522)^{0.47}\right)^{1.923}} \,\mathrm{cm}^3\,\mathrm{s}^{-1}, \tag{6.3.2}$$

where $\lambda = 315614\,\mathrm{K}/T$ and T is the gas temperature (see below). Finally, we assume that two mechanisms are responsible for possible ionisation effects of the hydrogen. One is the photo-ionisation process due to the UV background, while the other considers ionisation via collisional interactions among the neutral hydrogens. The total ionisation rate $\Gamma_{\rm tot}$ is then the sum of these two components: $\Gamma_{\rm tot} = \Gamma_{\rm phot} + \Gamma_{\rm col}$. $\Gamma_{\rm phot}$ is calculated from the rate of UV background photons, $\Gamma_{\rm UVB}$, taking into account the fact that some neutral hydrogen is in dense environments, so self-shielding effects prevent it to be ionised. To implement these effects we use the fitting function in [242] (and used in [244]) based on accurate radiative transfer simulations,

$$\frac{\Gamma_{\rm phot}}{\Gamma_{\rm UVB}} = 0.98 \left[1 + \left(\frac{n_{\rm H}}{n_{\rm H,SSh}}\right)^{1.64}\right]^{-2.28} + 0.02 \left[1 + \frac{n_{\rm H}}{n_{\rm H,SSh}}\right]^{-0.84}, \tag{6.3.3}$$

where $n_{\rm H}$ is the total (ionised and non-) hydrogen number density and $n_{\rm H,SSh}$ is the self-shielding density threshold analytically predicted by [245],

$$n_{\rm H,SSh} = 6.73 \times 10^{-3}\,\mathrm{cm}^{-3} \left(\frac{\bar{\sigma}_{\nu_{\rm HI}}}{2.49 \times 10^{-18}\,\mathrm{cm}^{-2}}\right)^{-2/3} \times \left(\frac{\Gamma_{\rm UVB}}{10^{-12}\,\mathrm{s}^{-1}}\right)^{2/3}. \tag{6.3.4}$$

As can be seen from the above equations, the photo-ionisation rate is fully captured by specifying the UV background rate, $\Gamma_{\rm UVB}$, and the hydrogen absorption cross-section, $\bar{\sigma}_{\nu_{\rm HI}}$ for which we use the UVB model in [246]. On the other hand, the collisional rate, $\Gamma_{\rm col}$, depends on the temperature of the gas (which we fix to be $T = 10^4\,\mathrm{K}$, the temperature typically observed in the warm-neutral interstellar medium, see [221, 242]) and is calculated using the approximation in [247],

$$\Gamma_{\rm coll} = \Lambda_{\rm T}\,(1 - \eta)\,n_{\rm H}, \tag{6.3.5}$$

where $\eta = n_{\rm NH}/n_{\rm H}$, i.e. it is the fraction of hydrogen which is in non-ionised form,

and

$$\Lambda_{\rm T} = 1.17 \times 10^{-10} \, \frac{(T/1\,{\rm K})^{1/2} \, \exp\left(-157809\,{\rm K}/T\right)}{1+\sqrt{T/10^5\,{\rm K}}} \, {\rm cm}^3\,{\rm s}^{-1}. \tag{6.3.6}$$

The post-processing for star-forming cells described above gives the total mass fraction of hydrogen that is non-ionised ($M_{\rm NH}$): atomic (HI) and molecular hydrogen (H_2), so $M_{\rm NH} = M_{\rm HI} + M_{\rm H_2}$. As we are interested only in HI, we need to remove the fraction of non-ionised hydrogen that is in molecular form, i.e. $f_{\rm H_2} = M_{\rm H_2}/M_{\rm NH}$. To do so, we follow the approach in [221] based on the KMT model [248–250], that is sketched below. We estimate $f_{\rm H_2}$ in each star-forming Voronoi cell as

$$f_{\rm H_2} = \begin{cases} 1 - \frac{0.75\,s}{1+0.25\,s} & \text{if } s < 2 \\ \\ 0 & \text{if } s \geq 2 \end{cases}, \tag{6.3.7}$$

where s is

$$s = \frac{\log\left(1 + 0.6\,\chi + 0.01\,\chi^2\right)}{0.6\,\tau_{\rm c}}, \tag{6.3.8}$$

and

$$\chi = 0.756\,\left(1 + 3.1\,Z^{0.365}\right), \quad \tau_{\rm c} = \Sigma\,\sigma_{\rm d}/\mu_{\rm H}. \tag{6.3.9}$$

Z is the gas metallicity in units of solar metallicity, $\sigma_{\rm d}$ is the dust cross-section (estimated as $\sigma_{\rm d} = Z \times 10^{-21}\,{\rm cm}^2$), $\mu_{\rm H}$ is the mean mass per hydrogen nucleus ($\simeq 2.3 \times 10^{-24}\,{\rm g}$) and Σ is the surface density of the gas, $\Sigma = \rho_{\rm g}\,R_{\rm V}$, with $\rho_{\rm g}$ the gas density and $R_{\rm V}$ the radius of the Voronoi cell for which we calculate the fraction of H_2 [221]. The fraction of H_2 is then removed from the total non-ionised hydrogen mass ($M_{\rm NH}$) in each gas cell, to obtain the mass in atomic HI hydrogen.

6.4 Overall neutral hydrogen density

In this section we show the results from the overall neutral hydrogen density at different redshifts. We follow the definition for the overall HI abundance, $\Omega_{\rm HI}(z) = \bar{\rho}_{\rm HI}(z)/\rho_{\rm c0}$, used in [221], where $\bar{\rho}_{\rm HI}(z)$ is the mean HI density measured from simulations and $\rho_{\rm c0}$ is the present-day critical density. The results are given in Figure 6.1,

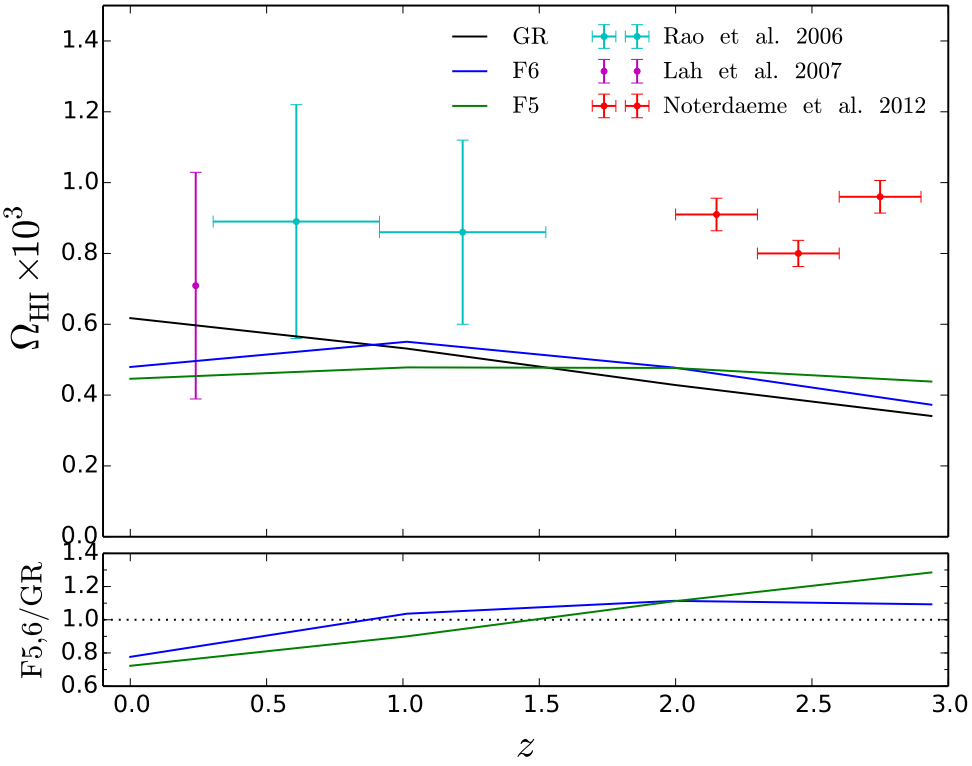

Figure 6.1: *Top panel*: Overall HI abundance, $\Omega_{\rm HI}(z) = \bar{\rho}_{\rm HI}(z)/\rho_{\rm c0}$, where $\bar{\rho}_{\rm HI}(z)$ is the mean HI density, from GR (black line), F6 (blue line) and F5 (green line) simulations, compared with observational measurements (symbols). *Bottom panel*: the relative differences in the simulation predictions from F6 (blue) and F5 (green) w.r.t. GR.

where we also show some observational measurements of the HI abundance at different redshifts from [251–253]. As we can see from this figure, the HI abundance from our simulations is lower than observations at all redshifts as was also found in [221]. This is because the neutral hydrogen in the post-reionisation epoch is concentrated in haloes where the shielding effects screen them from ionisation. It was shown in [221] by comparing low- and high-resolution simulations that there is an appreciable amount of HI in haloes down to $10^9\,\mathrm{M}_\odot$. However, our simulations do not resolve these masses accurately and consequently we miss the HI that is inside such haloes. Although this affects the absolute values of the HI found in our simulations, we do not expect it to affect appreciably our results on the relative differences among the models considered here (see discussions in [222–224]). As we will see below, the differences between the HI distributions for MG and GR are related to the differences in the halo abundances among these models. F5 and F6 produce more haloes in the low-mass end of the halo mass function, being able to cool the gas more efficiently, and a higher-resolution simulation able to resolve haloes down to $\sim 10^9$ $\mathrm{M}_\odot$ will probably detect the model differences at that mass scale (which are expected to be larger due to weaker screening for low-mass haloes).

The ratios of $\Omega_{\rm HI}(z)$ in F5 and F6 wrt GR are shown in the lower panel of Figure 6.1. We notice a similar trend in F6 and F5 when compared to GR, both showing more HI than GR at $z > 1$, while at lower redshifts they present less HI than GR. Overall, we find that HI is $\sim 20\%$ (30%) less abundant in F6 (F5) than GR at $z = 0$, and at $z = 3$ there is $\sim 10\%$ (30%) more HI in F6 (F5) than GR.

6.5 HI power spectra

We calculate the HI power spectrum $P_{\rm HI}(k)$ in real and redshift space from the simulation outputs using a cloud-in-cell (CIC) density assignment scheme (using the code [175]), with the shot noise subtracted following the prescription in [118]. In the upper panels of Figure 6.2, we demonstrate the measured power spectra for the

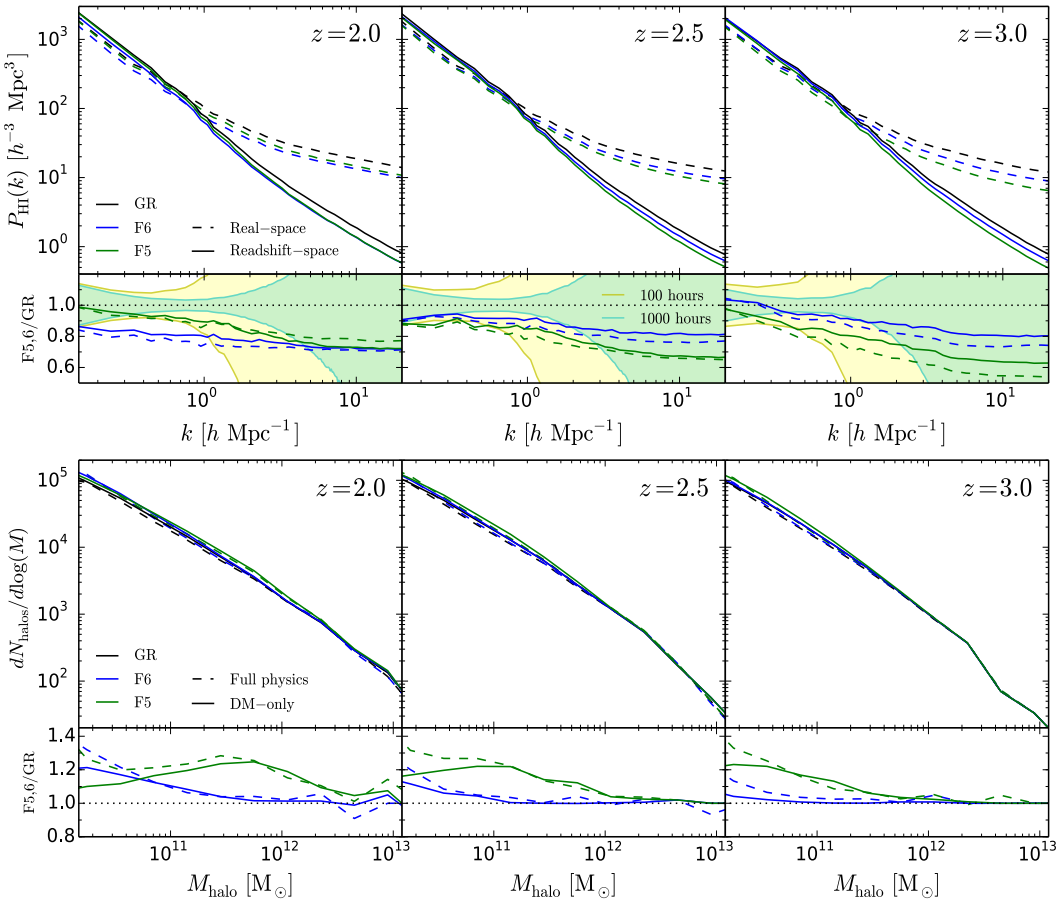

Figure 6.2: *Upper panels*: Neutral hydrogen power spectra $P_{\rm HI}$ at $z = 2.0, 2.5, 3.0$ (left to right) for the three models considered in the analysis (as labelled). The solid lines show the results in redshift space, and the dashed lines in real space (the latter will appear in our work [108]). The shaded areas in the lower sub-panels represent the expected errors from SKA1-MID measurements for GR, assuming 100 (yellow) and 1000 (green) observing hours. *Lower panels*: Differential halo mass functions at $z = 2.0, 2.5, 3.0$ (left to right) for the same models. Dashed (solid) lines show the results from full-physics (DMO) simulations. The lower subpanels show the relative differences from GR.

HI overdensity, $\rho_{\rm HI}/\bar{\rho}_{\rm HI}$, where $\bar{\rho}_{\rm HI}$ is the mean HI density as mentioned above. At $z = 3$, we find the largest deviations in $P_{\rm HI}$ among the models. Indeed, F5 and F6 show less clustering in both real and redshift space, e.g., for F5 we find a difference w.r.t. GR of $\sim 35\%$ in real space and $\sim 25\%$ in redshift space at $k \sim 2\,h\,{\rm Mpc}^{-1}$ and they increase at larger k. At $z = 2.5$, we see that the HI $P(k)$ for F5 is still lower than that for F6 at all the k-values shown, although the difference between these two models are smaller than at $z = 3$. Interestingly, at $z = 2$, we find an inversion of the trend between F5 and F6, with F6 displaying less power than F5.

In the lower panels of Figure 6.2, we compare the differential halo mass functions (HMF), $dN/d\log(M_{\rm halo})$, for main haloes from the full-physics (dashed lines) and DMO (solid) simulations. The haloes are identified using the Friends-of-Friends algorithm with a linking length of $b = 0.2$ [254]. The halo mass $M_{\rm halo}$ is defined as M_{200}, the mass contained in a sphere of radius r_{200}, within which the average density is 200 times the critical density at the specified redshift.

From Figure 6.2 we see that at $z \gtrsim 2.5$ F5, F6 are characterised by more low-mass haloes ($M_{\rm halo} \lesssim 10^{12}\,{\rm M}_\odot$) than GR. As HI can survive only in haloes where the shielding effects prevent it from ionisation, in MG there are more hosts for HI than GR. Therefore, our interpretation of the behaviour of the HI power spectra in the different models is that it primarily reflects the differences in the HMFs of these models (though these models have also different halo density profiles which could impact on the HI distribution as well), with $f(R)$ gravity being able to turn more low initial density peaks into haloes in the low-mass end. Given that low initial density peaks have less clustering, HI, as a tracer of the haloes, has a lower clustering amplitude in $f(R)$ models than in GR. At $z = 2$, the behaviour of HMFs is similar to $z = 3$, but we find more low-mass haloes in F6 than in F5 because in F5 smaller haloes merge more rapidly to form larger haloes – this can explain the inversion of the trend in the HI power spectra between F5 and F6 seen above. At $z = 0$ (not shown here) we find that the low-mass end of the HMF is strongly affected by galaxy formation and can no longer be explained solely by the difference in gravity;

S/N	$z = 3.0$	$z = 2.5$	$z = 2.0$
F6	4.3	6.7	18.3
F5	10.0	10.9	9.6

Table 6.1: The integrated S/N ratios for distinguishing a MG model from GR using redshift-space $P_{\rm HI}(k)$ with $k_{\rm max} = 2\,h\,{\rm Mpc}^{-1}$, with $({\rm S/N})^2 \equiv \sum_{k_{\rm min}}^{k_{\rm max}} \left[P_{\rm HI}^{\rm MG}(k) - P_{\rm HI}^{\rm GR}(k)\right]^2 / \sigma^2(k)$; $\sigma(k)$ is the expected 1σ error from SKA1-MID for 1000 hours (see [224, 255]), while $k_{\rm min}$ is set by the value of the box length L in our simulations, $k_{\rm min} = 2\,\pi/L$.

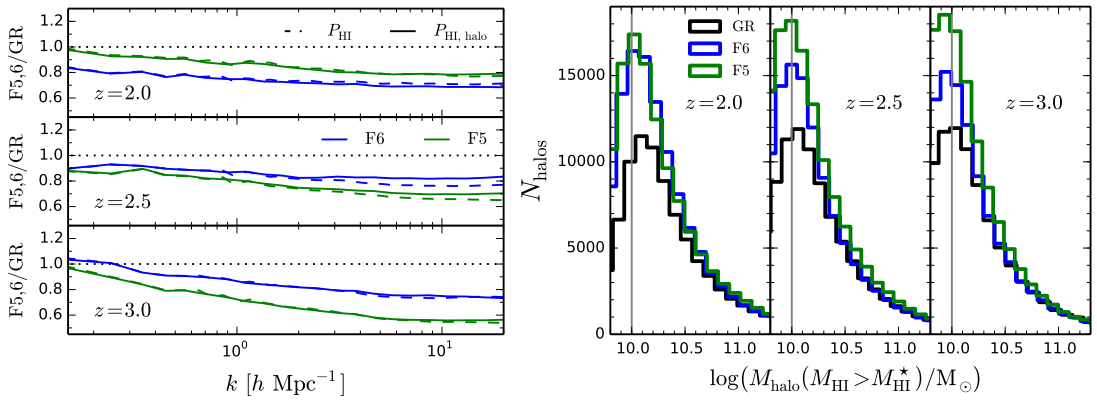

Figure 6.3: *Left panels*: Ratios of F5 (green) and F6 (blue) wrt GR for the *actual* real-space HI power spectrum (dashed lines) and the $P_{\rm HI,halo}$ defined in the text (solid lines) at $z = 2.0, 2.5, 3.0$ (top to bottom). *Right panels*: histograms of the number of haloes with HI mass $\geq M_{\rm HI}^{\star} = 10^6\,{\rm M}_{\odot}$, for GR (black), F6 (blue) and F5 (green) at $z = 2.0, 2.5, 3.0$ (left to right). The vertical grey lines show haloes with 50 particles.

at this redshift the model differences in both $P_{\rm HI}$ and HMF are smaller, implying weak constraining potential of $f(R)$ gravity at low redshifts.

A very interesting observation is that galaxy formation has a non-negligible impact on the HMF, but a comparison of the dashed and solid curves in the lower subpanels shows that the relative difference in the F6/F5 and GR HMFs is unaffected by baryonic physics for $M_{\rm halo} \gtrsim 10^{10\sim10.5}\,{\rm M}_{\odot}$ at $z = 2 \sim 3$. It implies that the impacts of baryons and MG can be separated [108], and the DMO simulations can be useful to study the $P_{\rm HI}$ (see [221]) even for MG models such as $f(R)$ gravity.

To further check the above explanation for the different behaviour of $P_{\rm HI}$, we have carried out two more tests. The left panel of Figure 6.3 compares the HI power spectrum (the *actual* $P_{\rm HI}$) in real space with a power spectrum, $P_{\rm HI,\,halo}$, calculated by assuming that for each halo all the HI contained in it is at its centre. Up to $k \sim 2\,h\,{\rm Mpc}^{-1}$, the ratios of $P_{\rm HI,\,halo}$ are very similar (within a few %) to those from

actual $P_{\rm HI}$, confirming that the model differences in $P_{\rm HI}$ at large scales are governed by halo clustering. However, at larger k, the $P_{\rm HI,\,halo}$ results start to deviate from the actual $P_{\rm HI}$ because the former do not account for the spatial distribution of HI inside the halos [221]. The histograms in the right panels of Figure 6.3 display the numbers of haloes with HI mass $M_{\rm HI} \geq 10^6\,{\rm M}_\odot$ (and thus contribute more to $P_{\rm HI}$). We can see that at $z \gtrsim 2.5$ there are more small HI-rich haloes in F5 than F6 and GR, confirming that HI is distributed in a less clustered way in F6/F5 than in GR. At $z = 2$, F6 and F5 are very similar, both having more small HI-rich haloes than GR; for $M_{\rm halo} \gtrsim 1.3 \times 10^{10}\,{\rm M}_\odot$, F6 has indeed slightly more HI-rich haloes than F5, which may explain the inversion of the $P_{\rm HI}$ for F6 than F5 at this redshift.

To understand to what extent future experiments can distinguish F6/F5 from GR by using the $P_{\rm HI}$ measured in redshift space, we have estimated the 1σ errors on the power spectrum expected from the instrumental noise of SKA1-MID radio telescope [102] for GR, following the method in [224, 255] and using the realistic baseline densities computed in [219]. We calculate the expected 1σ errors for 100 and 1000 observing hours, as shown by the shaded areas in the upper lower-subpanels of Figure 6.2. Comparing the errors with the $P_{\rm HI}$ ratios wrt GR in redshift space (solid lines), we find that F5 can be distinguished from GR at $z = 3$ and for $k < 2\,h\,{\rm Mpc}^{-1}$ by using a 1000-hour integration. F6 can be distinguished from GR at $z = 2$ and for $k < 2\,h\,{\rm Mpc}^{-1}$ with just 100 observing hours. The integrated S/N ratios for the distinguishability of the MG models from GR are shown in Table 6.1 for $k < 2\,h\,{\rm Mpc}^{-1}$.

Figure 6.3 shows that the HI host halo mass peaks at 10^{10} ${\rm M}_\odot$ at $z = 2 \sim 3$. Due to their resolution, our simulations have few host haloes with masses $\lesssim 10^9$ ${\rm M}_\odot$. Future higher-resolution runs can tell what happens to the HMFs at $\lesssim 10^9$ ${\rm M}_\odot$: if the models differ less there, our conclusions will not be significantly affected; if – in the more likely scenario – they differ more, we expect to see stronger model differences in $P_{\rm HI}$ and HMF, and probably the difference can be seen at even higher redshifts.

6.6 Summary and conclusions

Chameleon-type MG models such as $f(R)$ gravity have the particular property that chameleon screening becomes inefficient first for small structures (and underdense environments), and then move to massive objects (and dense environments). As a consequence, the HMF is enhanced early on at the low-mass end (cf. Figure 6.2) while the high-mass end is boosted by the fifth force at low redshift. To date, cosmological probes proposed to test such models are primarily at low z, focusing on either large objects [207–210] or low-density regions [211–215]. Due to the more efficient screening, the constraining power from massive objects is limited, and stronger constraints can be achieved if we are able to identify and trace low-mass objects in observations, which is more challenging. [256] shows that high-density galaxy catalogues, such as the main galaxy sample from SDSS [257] or the bright galaxy sample from DESI [100] can be used to probe the clustering of small (sub)haloes, offering a potentially stringent test of this class of models, but still at low z.

The fact that the low-mass end of the HMF can be modified by MG at high z ($z \sim 3$) suggests that strong constraints could be achieved by tracing the abundance and clustering of small haloes at high z. 21-cm intensity mapping is a very promising probe, which is sensitive to the abundance of haloes down to $\sim 10^8 \mathrm{M}_\odot$ [221] while not requiring to detect individual haloes. We showed that, thanks to the strong effect of chameleon MG on haloes $\lesssim 10^{12}\mathrm{M}_\odot$, the redshift-space HI power spectrum is modified by $\gtrsim 20\%$ ($\gtrsim 35\%$) for F6 (F5) at $z = 3$, which is stronger than or comparable to the model differences from ΛCDM in other low-z probes. This implies that future 21 cm intensity experiments can be used to test $f(R)$ gravity, and could, in principle, push the observational bounds on $|f_{R0}|$ to $\lesssim 10^{-6}$. Measurements of the 21 cm signal can also give accurate information on the expansion history [258–260] – this can be used to break potential degeneracy between modified expansion history and structure growth, e.g. viable $f(R)$ models have practically identical expansion history as ΛCDM, but structures grow differently at high z as we have seen in this chapter.

As a final remark, we note that the HI distribution in the simulations is regulated by baryonic effects such as the galactic wind feedback. It is therefore to be determined in a future work how robust the predictions on $P_{\rm HI}$ are against changes in the feedback implementation. We note also that the simulations used here cannot resolve the HI in haloes $< 10^9\,{\rm M}_\odot$ accurately, and this can affect the HI power spectrum results at high wavenumbers, $k > 2\,h\,{\rm Mpc}^{-1}$. High-resolution hydrodynamical simulations will clarify the behaviour of the HI power spectrum in GR and MG at these scales.

Chapter 7

Conclusions

Although the standard ΛCDM model has successfully passed almost all the available observational tests, the model still faces some challenges. For example, we still do not know the true nature of dark matter particles. Moreover, due to the lack of accurate observational data on how matter clusters on dwarf galaxies scales and below (together with the possible small-scale controversies faced by ΛCDM) we have little firm information on the shape of the underlying matter power spectrum at large wavenumbers. Many alternative scenarios to ΛCDM predict damped matter fluctuations on galactic and sub-galactic scales, potentially introducing new phenomenology on those scales. Independently of whether these alternatives can provide real solutions to the challenges experienced by ΛCDM, it is interesting to understand how features in the linear-theory power spectra imprint effects on non-linear structures.

Regarding the late-acceleration period, modified gravity models, though not satisfactorily resolving all the problems of the cosmological constant, can provide a useful testbed that can be used to test the theory of gravity on cosmological scales with future surveys (such as DESI [99, 100], EUCLID [101] or SKA [102]). In this thesis, we have addressed the question of how alternatives to ΛCDM affect structure formation using high-resolution N-body and hydrodynamical simulations. The main results of this study are summarised below.

7.1 Thermal velocities and non-linear structure

In Chapter 2, we investigated the impact of thermal velocities in N-body simulations of structure formation in warm dark matter models. The prescription used for adding thermal velocities introduces numerical noise into the initial conditions, which influences structure formation. At early times, the noise dramatically affects the power spectra measured from simulations with thermal velocities, with deviations of the order of $\sim \mathcal{O}(10)$ (in the matter power spectra) and of the order of $\sim \mathcal{O}(10^2)$ (in the velocity power spectra) compared to those extracted from simulations without thermal velocities. At late times, these effects are less pronounced with deviations of less than a few percent. We also found that spurious haloes start to appear in simulations which include thermal velocities at a mass that is $\sim$3 times larger than in simulations without thermal velocities.

7.2 Growth of structures in damped models

In Chapter 3, using N-body simulations, we addressed the question of how much information is retained from different scales in the initial linear power spectrum of damped models following the nonlinear growth of structure. By using different initial linear-theory matter power spectra we showed that, once the system undergoes nonlinear evolution, the shape of the linear power spectrum at high wavenumbers does not affect the non-linear power spectrum. Indeed, we found that linear power spectra which differ from one another only at wavenumbers larger than their half-mode wavenumber give rise to almost identical nonlinear power spectra at late times, regardless of the fact that they originate from different models with damped fluctuations. On the other hand, the halo mass function is more sensitive to the form of the linear power spectrum. We identified a two parameter model of the transfer function in generic nCDM-like damped scenarios, and showed that this parametrisation works as well as the standard three parameter model found in [75]. However, we note that the 2- and 3-parameter model cannot be applied to the case of

thermal inflation and BSI models, because they present an enhancement in the linear power spectrum with respect to ΛCDM before the cut-off scale (see Chapter 5).

7.3 Smooth-k space filter

Following the above results, in Chapter 4 we proposed a new filter, a smooth-k space filter, to use in the Press-Schechter approach to model the dark matter halo mass function which overcomes shortcomings of other filters. We tested this against the mass function measured in N-body simulations from Chapter 3 and found that, while the commonly used sharp-k filter fails to reproduce the behaviour of the simulation halo mass function at low masses for models with a sharp truncation in the linear power spectrum, the predictions with our new filter agree with the simulation results over a wider range of halo masses for both damped and undamped power spectra.

7.4 Thermal inflation

Thermal inflation models (which feature two inflationary stages) can display damped primordial curvature power spectra on small scales which generate damped matter fluctuations. Matter power spectra in these models are also characterised by an excess of power (with respect to the standard ΛCDM power spectrum) just below the suppression scale. In Chapter 5 we investigated the non-linear growth of structure in models of thermal inflation. We measured the non-linear matter power spectrum and extracted halo statistics, such as the halo mass function, and compared these quantities with those predicted in the standard ΛCDM model and in other models with damped matter fluctuations. We found that the thermal inflation models considered here produce measurable differences in the matter power spectrum from ΛCDM at redshifts $z > 5$ for wavenumbers $k \in [2, 64]\, h\,\mathrm{Mpc}^{-1}$, while the halo mass functions are appreciably different at all redshifts in the halo mass range $M_{\mathrm{halo}} \in [10^9, 10^{12}]\, h^{-1}\,\mathrm{M}_\odot$ resolved by our simulations. The halo mass function at $z = 0$ for thermal inflation displays an enhancement of around $\sim 20\%$ with respect

to ΛCDM and a damping at lower halo masses, with the position of the enhancement depending on the value of the free parameter in the model. The enhancement in the halo mass function (with respect to ΛCDM) increases with redshift, reaching $\sim 40\%$ at $z = 5$. We also found that the analytical Press-Schechter approach with the smooth-k filter gives the best matches to the simulation results.

7.5 21-cm physics and models of MG

Future 21 cm intensity mapping surveys such as SKA will provide precise information on the spatial distribution of the neutral hydrogen (HI) in the post-reionisation epoch ($z < 6$). As the HI abundance and distribution depends on the overall matter distribution in our Universe and the strength of gravity, these surveys will allow us to test the standard ΛCDM paradigm and, at the same time, the nature of gravity. In Chapter 6, we employed full-physics hydrodynamical simulations in chameleon $f(R)$ modified gravity carried out with the Illustris TNG model in AREPO to quantify the effects of modified gravity force on HI abundances and power spectra. We found that the enhanced growth, which low-mass dark matter haloes experience in $f(R)$ gravity at high redshifts, alters the HI power spectrum. Our results suggest that the HI power spectrum is suppressed by $\sim 20\%$ on scales $k \lesssim 2\,h\,\mathrm{Mpc}^{-1}$ for F6, a model with a weak deviation from general relativity. These differences are detected by SKA1-MID with an expected signal-to-noise level of S/N ≈ 18 at $z = 2$, making HI clustering a powerful test of gravity at these redshifts.

7.6 Future directions

In this thesis, we have focused on a limited number of effects that alternatives to the ΛCDM model produce on structure formation. In the following, we provide some suggestions on how the results obtained so far can be extended.

Thermal velocities in composite DM models – In Chapter 2, we considered the effects of thermal velocities in pure thermal WDM models. These models are charac-

terised by strong cut-offs and WDM candidate masses around keV, both of these properties preventing significant physical effects of thermal velocities. Indeed, thermal velocities only affect the inner-most parts of the haloes [149,150]. The situation may change if we consider composite DM models (e.g. mixed DM or CDM + massive νs), as such models have no strong cut-offs because of the remaining CDM influence once the WDM component has died off [134]. This means that we can have haloes down to very small scales, where the thermal motion can be important [151–153]. Analysing composite DM simulations with thermal velocities can then clarify the physical role of thermal velocities in structure formation, and, for this reason, they deserve further investigation.

Testing the accuracy of smooth-k space filter at low masses – In Chapter 4, we introduced a smooth-k space filter, showing its superior accuracy in predicting the halo mass function when compared with N-body simulations. However, in the case of thermal WDM, we found that the smooth-k space and the sharp-k space filters give approximately the same results at the halo masses that are well resolved by our simulations (i.e. $M > 10^{8.5}\, h^{-1}\, \mathrm{M}_{\odot}$). The next step would be to test even further the accuracy of our filter in the region of masses, $M < 10^{8.5}\, h^{-1}\, \mathrm{M}_{\odot}$, where the damping effects are extreme and the predictions using our filter can differ from those expected from other filters by orders of magnitudes (see e.g. Figure 4.3).

Moreover, as found in Chapter 3 (for an oscillatory power spectrum) and pointed out in [202], our results suggest that the oscillatory features appearing in the linear-theory $P(k)$ after the damping scale tend to be erased by structure formation. In the halo mass function, we can still see oscillatory behaviour, but the amplitude of the oscillations are extremely weakened by the non-linear effects (see e.g. the halo mass function for the oscillatory power spectrum in Figure 4.2). In this case, the differences in the results between our new filter and the sharp-k space filter become more apparent than in thermal WDM: the sharp-k space filter predicts larger oscillations (the same effects was found in the case of thermal inflation and BSI, see e.g. Figure 5.5). Using high-resolution N-body simulations, able to probe

the region $M < 10^{8.5}\,h^{-1}\,\mathrm{M}_\odot$, we are planning to assess the effects of the oscillations at the low-mass end of the halo mass function, clarifying the extent of the accuracy of our new filter in predicting these features[1].

Constraining damped models using 21-cm in pre-reionization epoch – The EDGES experiment [201] claims a detection of a global 21-cm absorption line at $z \sim 20$. This seems to indicate that star formation was efficient even at such high redshifts. [202, 203] have used the timing of this signal to constrain nCDM models. Indeed, these models are characterised by a delay in structure formation (and consequently in star formation) with respect to the ΛCDM due to the suppression of the power spectrum at small scales. The constraints in [202, 203] are obtained under the hypothesis that stars form in spherical haloes. However, it was suggested in [262] (but see also [263]) that in damped models, such as WDM, the first stars can form in massive filaments (or even sheets) instead of haloes. This scenario could modify the constraints reported in [202, 203], because, in general, filaments form earlier than haloes. If the stars forming inside these structures produce enough Lyman-α photons, they could be able to give an early 21-cm absorption signal in WDM, losening the constraints found in the literature. It is also interesting to note that Lyman-α photons can be produced by the radiative cooling process (without the need for star-formation) of the gas falling into the DM potential well of the filament. Indeed, during gas accretion into the DM structure, part of the initial gravitational binding energy is available to be radiated, a phenomenon which is well studied in the context of the so-called Lyman-α "blobs" at $z \sim 3$ [264, 265]. We are addressing these questions by running very high-resolution N-body simulations (able to probe 10 kpc-scale filaments) in WDM and thermal inflation cosmologies and by using a semi-analytical approach to model star-formation and gas-cooling in these massive structures. These results will help us to understand if filaments can light up the

[1] We note that a recent paper [261] has partially addressed this issue in the case of N-body simulations of ETHOS models (which feature a similar oscillation pattern in the linear power spectrum as that considered here), finding that the oscillations are extremely reduced in the halo mass function at $z = 0$ and that our filter provides a better match to simulations than the sharp-k space filter.

Universe in WDM-like scenarios, inducing a 21-cm absorption signal in line with the EDGES experiment.

Minkowski functionals and HI – Regarding the effects of modified gravity on the 21-cm power spectrum in the post-reionization epoch, an interesting aspect to develop is the use of Minkowski functionals (MF, see e.g. [266]) to study the HI distribution in our simulations. MF can give information on the HI distribution beyond the simple two-point correlation function (i.e. the power spectrum), and can be used to understand how the entire morphology of the neutral hydrogen (and not only the power spectrum) changes in MG with respect to GR.

7.7 Concluding remarks

Current and future experiments such as DES, DESI, EDGES, EUCLID, LSST and SKA will give us very precise information on the clustering power spectrum and, with that, the underlying matter distribution in our Universe. For these reasons, accurate theoretical predictions are needed to interpret these new data. In this thesis, we have presented some of these theoretical studies, both using numerical and analytical approaches, focusing on understanding how alternatives to ΛCDM models can imprint distinctive features on the non-linear Universe. We hope that our results can be used in the near future to explore even further the nature of the dark sectors and finally find an answer to the big cosmological questions.

Bibliography

[1] M. Leo, C. M. Baugh, B. Li, S. Pascoli, *The Effect of Thermal Velocities on Structure Formation in N-body Simulations of Warm Dark Matter*, JCAP **11**, 017 (2017) [arXiv:1706.07837 [astro-ph.CO]].

[2] M. Leo, C. M. Baugh, B. Li, S. Pascoli, *Non-linear growth of structure in cosmologies with damped matter fluctuations*, JCAP **08**, 001 (2018), [arXiv:1712.02742 [astro-ph.CO]].

[3] M. Leo, C. M. Baugh, B. Li, S. Pascoli, *A new smooth-k space filter approach to calculate halo abundances*, JCAP **04**, 010 (2018), [arXiv:1801.02547 [astro-ph.CO]].

[4] M. Leo, C. M. Baugh, B. Li, S. Pascoli, *N-body simulations of structure formation in thermal inflation cosmologies*, JCAP **12**, 010 (2018), [arXiv:1807.04980 [astro-ph.CO]].

[5] M. Leo, C. Arnold, B. Li, *A high-redshift test of gravity using enhanced growth of small structures probed by the neutral hydrogen distribution*, (2019) in preparation.

[6] A. Einstein, Preuss. Akad. Wiss. Berlin, Sitzber., 778 (1915a).

[7] A. Einstein, Preuss. Akad. Wiss. Berlin, Sitzber., 844 (1915b).

[8] A. Einstein, Preuss. Akad. Wiss. Berlin, Sitzber., 142 (1917).

[9] A. A. Friedmann, Zeitschr. fur Phys. 10, 377 (1922).

[10] G. Lemaître, Ann. Soc. Scient. Brux., 47A, 49 (1927).

[11] V. M. Slipher, *Spectrographic Observations of Nebulae*, Popular Astronomy **23**, 21-24 (1915).

[12] E. Hubble, *A Relation between Distance and Radial Velocity among Extra-Galactic Nebulae*, Proceedings of the National Academy of Science **15**, 168 (1929).

[13] V. J. Martinez, *Introductory review to the historical development of modern cosmology*, ASP Conf. Ser. **252**, 1 (2001) [astro-ph/0203377].

[14] M. S. Longair, *A Brief History of Cosmology*, Measuring and Modeling the Universe (2004).

[15] A. H. Guth, *The Inflationary Universe: A Possible Solution to the Horizon and Flatness Problems*, Phys. Rev. D **23**, 347 (1981).

[16] A. A. Starobinsky, *Spectrum of relict gravitational radiation and the early state of the universe*, JETP Lett. **30**, 682 (1979).

[17] A. D. Linde, *A New Inflationary Universe Scenario: A Possible Solution of the Horizon, Flatness, Homogeneity, Isotropy and Primordial Monopole Problems*, Phys. Lett. **108B**, 389 (1982).

[18] A. Albrecht and P. J. Steinhardt, *Cosmology for Grand Unified Theories with Radiatively Induced Symmetry Breaking*, Phys. Rev. Lett. **48**, 1220 (1982).

[19] A. R. Liddle and D. H. Lyth, *Cosmological Inflation and Large-Scale Structure*, Cambridge University Press, April (2000).

[20] S. Weinberg, *Cosmology*, OUP Oxford (2008), ISBN 9780198526827. URL:http://books. google.de/books?id=nqQZdg020fsC.

[21] V. F. Mukhanov and G. V. Chibisov, *Quantum Fluctuations and a Nonsingular Universe*, JETP Lett. **33**, 532 (1981).

[22] S. W. Hawking, *The Development of Irregularities in a Single Bubble Inflationary Universe*, Phys. Lett. **115B**, 295 (1982).

[23] A. H. Guth and S. Y. Pi, *Fluctuations in the New Inflationary Universe*, Phys. Rev. Lett. **49**, 1110 (1982).

[24] J. M. Bardeen, P. J. Steinhardt and M. S. Turner, *Spontaneous Creation of Almost Scale - Free Density Perturbations in an Inflationary Universe*, Phys. Rev. D **28**, 679 (1983).

[25] V. F. Mukhanov, H. A. Feldman and R. H. Brandenberger, *Theory of cosmological perturbations*, Phys. Rept. **215**, 203 (1992).

[26] G. F. Smoot *et al.* [COBE Collaboration], *Structure in the COBE differential microwave radiometer first year maps*, Astrophys. J. **396**, L1 (1992).

[27] D. N. Spergel *et al.* [WMAP Collaboration], *First year Wilkinson Microwave Anisotropy Probe (WMAP) observations: Determination of cosmological parameters*, Astrophys. J. Suppl. **148**, 175 (2003) [astro-ph/0302209].

[28] N. Aghanim *et al.* [Planck Collaboration], *Planck 2018 results. VI. Cosmological parameters*, [arXiv:1807.06209 [astro-ph.CO]].

[29] A. R. Liddle, *An Introduction to cosmological inflation*, [astro-ph/9901124].

[30] A. Riotto, *Inflation and the theory of cosmological perturbations*, ICTP Lect. Notes Ser. **14**, 317 (2003) [hep-ph/0210162].

[31] D. Baumann, *TASI Lectures on Primordial Cosmology*, [arXiv:1807.03098 [hep-th]].

[32] L. Kofman, A. D. Linde, A. A. Starobinsky, *Towards the theory of reheating after inflation*, Phys. Rev. D **56**, 3258 (1997) [arXiv:hep-ph/9704452].

[33] V. Lukovic, P. Cabella and N. Vittorio, *Dark matter in cosmology*, Int. J. Mod. Phys. A **29**, 1443001 (2014) [arXiv:1411.3556 [astro-ph.CO]].

[34] I. Tkachev, *Cosmology and Dark Matter*, [arXiv:1802.02414 [gr-qc]].

[35] M. Milgrom, *A Modification of the Newtonian dynamics as a possible alternative to the hidden mass hypothesis*, Astrophys. J. **270**, 365 (1983).

[36] E. P. Verlinde, *Emergent Gravity and the Dark Universe*, SciPost Phys. **2**, 016 (2017) [arXiv:1611.02269 [hep-th]].

[37] P. J. E. Peebles, *Large scale background temperature and mass fluctuations due to scale invariant primeval perturbations*, Astrophys. J. **263**, L1 (1982).

[38] R. Barkana and A. Loeb, *In the beginning: The First sources of light and the reionization of the Universe*, Phys. Rept. **349**, 125 (2001) [astro-ph/0010468].

[39] H. Mo, F. C. van den Bosch and S. White, *Galaxy Formation and Evolution*, Cambridge, UK: Cambridge University Press (2010).

[40] C. S. Frenk and S. D. M. White, *Dark matter and cosmic structure*, Annalen Phys. **524**, 507 (2012) [arXiv:1210.0544 [astro-ph.CO]].

[41] J. R. Primack, *Cosmological Structure Formation,* [arXiv:1505.02821 [astro-ph.GA]].

[42] S. Perlmutter *et al.* [Supernova Cosmology Project Collaboration], *Discovery of a supernova explosion at half the age of the Universe and its cosmological implications*, Nature **391**, 51 (1998) [astro-ph/9712212].

[43] S. Perlmutter *et al.* [Supernova Cosmology Project Collaboration], *Measurements of Omega and Lambda from 42 high redshift supernovae*, Astrophys. J. **517**, 565 (1999) [arXiv:astro-ph/9812133].

[44] A. G. Riess *et al.* [Supernova Search Team], *Observational evidence from supernovae for an accelerating universe and a cosmological constant*, Astron. J. **116**, 1009 (1998) [arXiv:astro-ph/9805201].

[45] B. P. Schmidt *et al.* [Supernova Search Team], *The High Z supernova search: Measuring cosmic deceleration and global curvature of the universe using type Ia supernovae*, Astrophys. J. **507**, 46 (1998) [arXiv:astro-ph/9805200].

[46] M. Colless *et al.* [2DFGRS Collaboration], *The 2dF Galaxy Redshift Survey: Spectra and redshifts*, Mon. Not. Roy. Astron. Soc. **328**, 1039 (2001) [astro-ph/0106498].

[47] I. Zehavi *et al.* [SDSS Collaboration], *Galaxy Clustering in early SDSS Redshift Data*, Astrophys. J. **571**, 172 (2002) [astro-ph/0106476].

[48] E. Hawkins *et al.*, *The 2dF Galaxy Redshift Survey: Correlation functions, peculiar velocities and the matter density of the universe*, Mon. Not. Roy. Astron. Soc. **346**, 78 (2003) [astro-ph/0212375].

[49] M. Tegmark *et al.* [SDSS Collaboration], *Cosmological parameters from SDSS and WMAP*, Phys. Rev. D **69**, 103501 (2004) [astro-ph/0310723].

[50] S. Cole *et al.* [2dFGRS Collaboration], *The 2dF Galaxy Redshift Survey: Power-spectrum analysis of the final dataset and cosmological implications*, Mon. Not. Roy. Astron. Soc. **362**, 505 (2005) [astro-ph/0501174].

[51] D. J. Eisenstein *et al.* [SDSS Collaboration], *Detection of the Baryon Acoustic Peak in the Large-Scale Correlation Function of SDSS Luminous Red Galaxies*, Astrophys. J. **633**, 560 (2005) [astro-ph/0501171].

[52] D. H. Weinberg, J. S. Bullock, F. Governato, R. Kuzio de Naray and A. H. G. Peter, *Cold dark matter: controversies on small scales*, Proc. Nat. Acad. Sci. **112**, 12249 (2015) [arXiv:1306.0913 [astro-ph.CO]]

[53] J. Dubinski, R. G. Carlberg, *The Structure of cold dark matter halos*, Astrophys. J. **378**, 496 (1991).

[54] J. F. Navarro, C. S Frenk, S. D. M. White, *The Structure of cold dark matter halos*, Astrophys. J. **462**, 563-575 (1996) [arXiv:astro-ph/9508025].

[55] J. F. Navarro, C. S Frenk, S. D. M. White, *A Universal density profile from hierarchical clustering*, Astrophys. J. **490**, 493-508 (1997) [arXiv:astro-ph/9611107].

[56] W. J. G. de Blok, S. S. McGaugh, A. Bosma, V. C. Rubin, *Mass density profiles of LSB galaxies*, Astrophys. J. **552**, L23-L26 (2001) [arXiv:astro-ph/0103102].

[57] P. Salucci, M. I. Wilkinson, M. G. Walker, G. F. Gilmore, E. K. Grebel, A. Koch, C. Frigerio Martins, R. F. G. Wyse, *Dwarf spheroidal galaxy kinematics and spiral galaxy scaling laws*, Mon. Not. Roy. Astron. Soc. **420**, 2034 (2012) [arXiv:1111.1165 [astro-ph.CO]].

[58] A. Klypin, A. V. Kravtsov, O. Valenzuela, F. Prada, *Where are the missing Galactic satellites?*, Astrophys. J. **522**, 82-92 (1999) [arXiv:astro-ph/9901240].

[59] B. Moore, S. Ghigna, F. Governato, G. Lake, T. Quinn, J. Stadel, P. Tozzi, *Dark matter substructure within galactic halos*, Astrophys. J. **524**, L19-L22 (1999) [arXiv:astro-ph/9907411].

[60] S. Mashchenko, J. Wadsley, H. M. P. Couchman, *Stellar Feedback in Dwarf Galaxy Formation*, Science **319**, 174 (2008) [arXiv:0711.4803 [astro-ph]].

[61] A. Pontzen, F. Governato, *How supernova feedback turns dark matter cusps into cores*, Mon. Not. R. Astron. Soc. **421**, 3464-3471 (2012) [arXiv:1106.0499 [astro-ph.CO]].

[62] D. Martizzi, R. Teyssier, B. Moore, *Cusp-core transformations induced by AGN feedback in the progenitors of cluster galaxies*, Mon. Not. R. Astron. Soc. **432**, 1947-1954 (2013) [arXiv:1211.2648 [astro-ph.CO]].

[63] A. M. Brooks, A. Zolotov, *Why Baryons Matter: The Kinematics of Dwarf Spheroidal Satellites*, ApJ **786**, 87 (2014) [arXiv:1207.2468 [astro-ph.CO]].

[64] J. Wang, C. S. Frenk, J. F. Navarro, L. Gao, T. Sawala, *The missing massive satellites of the Milky Way*, Mon. Not. R. Astron. Soc. **424**, 2715-2721 (2012) [arXiv:1203.4097 [astro-ph.GA]].

[65] M. Boylan-Kolchin, J. S. Bullock, M. Kaplinghat, *Too big to fail? The puzzling darkness of massive Milky Way subhaloes*, Mon. Not. Roy. Astron. Soc. **415**, L40 (2011) [arXiv:1103.0007 [astro-ph.CO]].

[66] M. Kamionkowski, A. R. Liddle, *The Dearth of halo dwarf galaxies: Is there power on short scales?*, Phys. Rev. Lett. **84**, 4525 (2000) [arXiv:astro-ph/9911103].

[67] M. J. White, R. A. C. Croft, *Suppressing linear power on dwarf galaxy halo scales*, Astrophys. J. **539**, 497 (2000) [arXiv:astro-ph/0001247].

[68] J. Yokoyama, *Inflation and the dwarf galaxy problem*, Phys. Rev. D **62**, 123509 (2000) [arXiv:astro-ph/0009127].

[69] A. R. Zentner, J. S. Bullock, *Inflation, cold dark matter, and the central density problem*, Phys. Rev. D **66**, 043003 (2002) [arXiv:astro-ph/0205216].

[70] A. Ashoorioon, A. Krause, *Power Spectrum and Signatures for Cascade Inflation.* [arXiv:hep-th/060700].

[71] T. Kobayashi, F. Takahashi, *Running Spectral Index from Inflation with Modulations*, JCAP **1101**, 026 (2011) [arXiv:1011.3988 [astro-ph.CO]].

[72] T. Nakama, J. Chluba, M. Kamionkowski, *Shedding light on the small-scale crisis with CMB spectral distortions*, Phys. Rev. D **95**, no. 12, 121302 (2017) [arXiv:1703.10559 [astro-ph.CO]].

[73] S. E. Hong, H. J. Lee, Y. J. Lee, E. D. Stewart, H. Zoe, *Effects of thermal inflation on small scale density perturbations*, JCAP **1506**, 002 (2015) [arXiv:1503.08938 [astro-ph.CO]].

[74] A. A. Starobinsky, *Spectrum of adiabatic perturbations in the universe when there are singularities in the inflation potential*, JETP Lett. **55**, 489 (1992).

[75] R. Murgia, A. Merle, M. Viel, M. Totzauer, A. Schneider, *"Non-cold" dark matter at small scales: a general approach*, JCAP **1711**, 046 (2017) [arXiv:1704.07838 [astro-ph.CO]].

[76] P. Bode, J. P. Ostriker, N. Turok, *Halo formation in warm dark matter models*, Astrophys. J. **556**, 93-107 (2001) [arXiv:astro-ph/0010389].

[77] P. Colin, V. Avila-Reese, O. Valenzuela, *Substructure and halo density profiles in a warm dark matter cosmology*, Astrophys. J. **542**, 622-630 (2000) [arXiv:astro-ph/0004115].

[78] S. H. Hansen, J. Lesgourgues, S. Pastor, J. Silk, *Constraining the window on sterile neutrinos as warm dark matter*, Mon. Not. Roy. Astron. Soc. **333**, 544-546 (2002) [arXiv:astro-ph/0106108].

[79] M.Viel, J. Lesgourgues, M. G. Haehnelt, S. Matarrese, A. Riotto, *Constraining warm dark matter candidates including sterile neutrinos and light gravitinos with WMAP and the Lyman-alpha forest*, Phys. Rev. D **71**, 063534 (2005) [arXiv:astro-ph/0501562].

[80] S. Dodelson, L. M. Widrow, *Sterile-neutrinos as dark matter*, Phys. Rev. Lett. **72**, 17-20 (1994) [arXiv:hep-ph/9303287].

[81] A. D. Dolgov, S. H. Hansen, *Massive sterile neutrinos as warm dark matter*, Astropart. Phys. **16**, 339-344 (2002) [arXiv:hep-ph/0009083].

[82] T. Asaka, M. Laine, M. Shaposhnikov, *Lightest sterile neutrino abundance within the nuMSM*, JHEP **01**, 091 (2007) [Erratum: JHEP02,028(2015)] [arXiv:hep-ph/0612182].

[83] K. Enqvist, K. Kainulainen, J. Maalampi, *Resonant neutrino transitions and nucleosynthesis*, Phys. Lett. B **249**, 531-534 (1990).

[84] X. Shi, G. M. Fuller, *A New dark matter candidate: Nonthermal sterile neutrinos*, Phys. Rev. Lett. **82**, 2832 (1999) [arXiv:astro-ph/9810076].

[85] K. Abazajian, G. M. Fuller, M. Patel, *Sterile neutrino hot, warm, and cold dark matter*, Phys. Rev. D **64**, 023501 (2001) [arXiv:astro-ph/0101524].

[86] A. Kusenko, *Sterile neutrinos, dark matter, and the pulsar velocities in models with a Higgs singlet*, Phys. Rev. Lett. **97**, 241301 (2006) [arXiv:hep-ph/0609081].

[87] K. Petraki, A. Kusenko, *Dark-matter sterile neutrinos in models with a gauge singlet in the Higgs sector*, Phys. Rev. D **77**, 065014 (2008) [arXiv:0711.4646 [hep-ph]].

[88] A. Merle, M. Totzauer, *keV Sterile Neutrino Dark Matter from Singlet Scalar Decays: Basic Concepts and Subtle Features*, JCAP **1506**, 011 (2015) [arXiv:1502.01011 [hep-ph]].

[89] J. König, A. Merle, M. Totzauer, *keV Sterile Neutrino Dark Matter from Singlet Scalar Decays: The Most General Case*, JCAP **1611**, 038 (2016) [arXiv:1609.01289 [hep-ph]].

[90] C. Boehm, R. Schaeffer, *Constraints on dark matter interactions from structure formation: Damping lengths*, Astron. Astrophys. **438**, 419-442 (2005) [arXiv:astro-ph/0410591].

[91] C. Boehm, J. A. Schewtschenko, R. J. Wilkinson, C. M. Baugh, S. Pascoli, *Using the Milky Way satellites to study interactions between cold dark matter and radiation*, Mon. Not. Roy. Astron. Soc. **445**, L31-L35 (2014) [arXiv:1404.7012 [astro-ph.CO]].

[92] J. A. Schewtschenko, R. J. Wilkinson, C. M. Baugh, C. Boehm, S. Pascoli, *Dark matter-radiation interactions: the impact on dark matter haloes*, Mon. Not. Roy. Astron. Soc. **449**, 3587 (2015)

[93] D. N. Spergel, P. J. Steinhardt, *Observational evidence for selfinteracting cold dark matter*, Phys. Rev. Lett. **84**, 3760-3763 (2000) [arXiv:astro-ph/9909386].

[94] D. J. E. Marsh, *Axion Cosmology*, Phys. Rept. **643**, 1-79 (2016) [arXiv:1510.07633 [astro-ph.CO]].

[95] J. Veltmaat, J. C. Niemeyer, *Cosmological particle-in-cell simulations with ultralight axion dark matter*, Phys. Rev. D **94**, no. 12, 123523 (2016) [arXiv:1608.00802 [astro-ph.CO]].

[96] J. Veltmaat, J. C. Niemeyer, B. Schwabe, *Formation and structure of ultralight bosonic dark matter halos*, (2018) [arXiv:1804.09647 [astro-ph.CO]].

[97] J. Martin, *Everything You Always Wanted To Know About The Cosmological Constant Problem (But Were Afraid To Ask)*, Comptes Rendus Physique **13**, 566 (2012) [arXiv:1205.3365 [astro-ph.CO]].

[98] C. P. Burgess, *The Cosmological Constant Problem: Why it's hard to get Dark Energy from Micro-physics*, Proceedings, 100th Les Houches Summer School: Post-Planck Cosmology: Les Houches, France, July 8 - August 2, 2013 [arXiv:1309.4133 [hep-th]].

[99] M. Levi *et al.* [DESI Collaboration], *The DESI Experiment, a whitepaper for Snowmass 2013*, [arXiv:1308.0847 [astro-ph.CO]].

[100] A. Aghamousa *et al.* [DESI Collaboration], *The DESI Experiment Part I: Science,Targeting, and Survey Design*, [arXiv:1611.00036 [astro-ph.IM]].

[101] R. Laureijs, *et al.*, *Euclid Definition Study Report*, [arXiv:1110.3193 [astro-ph.CO]].

[102] P. E. Dewdney *et al.* (2013), SKA Organisation, http://skatelescope.org.

[103] A. Joyce, B. Jain, J. Khoury and M. Trodden, *Beyond the Cosmological Standard Model*, Phys. Rept. **568**, 1 (2015) [arXiv:1407.0059 [astro-ph.CO]].

[104] K. Koyama, *Cosmological Tests of Modified Gravity*, Rept. Prog. Phys. **79**, no. 4, 046902 (2016) [arXiv:1504.04623 [astro-ph.CO]].

[105] H. A. Buchdahl, *Non-linear Lagrangians and cosmological theory*, Mon. Not. Roy. Astron. Soc. **150**, 1 (1970).

[106] P. Brax, A. C. Davis, B. Li and H. A. Winther, *A Unified Description of Screened Modified Gravity*, Phys. Rev. D **86**, 044015 (2012) [arXiv:1203.4812 [astro-ph.CO]].

[107] W. Hu and I. Sawicki, *Models of f(R) Cosmic Acceleration that Evade Solar-System Tests*, Phys. Rev. D **76**, 064004 (2007) [arXiv:0705.1158 [astro-ph]].

[108] C. Arnold, M. Leo and B. Li, *Simulating galaxy formation in modified gravity: Full physics hydrodynamical simulations in $f(R)$ gravity with AREPO*, in preparation (2018).

[109] K. Dolag, S. Borgani, S. Schindler, A. Diaferio and A. M. Bykov, *Simulation techniques for cosmological simulations*, Space Sci. Rev. **134**, 229 (2008) [arXiv:0801.1023 [astro-ph]].

[110] Y. B. Zeldovich, *Gravitational instability: An Approximate theory for large density perturbations*, Astron. Astrophys. **5**, 84 (1970).

[111] R. Scoccimarro, *Transients from initial conditions: a perturbative analysis*, Mon. Not. Roy. Astron. Soc. **299**, 1097 (1998) doi:10.1046/j.1365-8711.1998.01845.x [astro-ph/9711187].

[112] M. Crocce, S. Pueblas, R. Scoccimarro, *Transients from Initial Conditions in Cosmological Simulations*, Mon. Not. Roy. Astron. Soc. **373**, 369 (2006) [arXiv:astro-ph/0606505].

[113] V. Springel, *The cosmological simulation code GADGET-2*, Mon. Not. Roy. Astron. Soc. **364**, 1105 (2005) [arXiv:astro-ph/0505010].

[114] S. D. M. White and M. J. Rees, *Core condensation in heavy halos: A Two stage theory for galaxy formation and clusters*, Mon. Not. Roy. Astron. Soc. **183**, 341 (1978).

[115] G. Tormen, *Hydrodynamic Simulations of Galaxy Formation*, [astro-ph/9604081].

[116] R. S. Somerville and R. Davé, *Physical Models of Galaxy Formation in a Cosmological Framework*, Annual Review of Astronomy and Astrophysics **53**, 51-113 (2015) [arXiv:1412.2712 [astro-ph.GA]]

[117] V. Springel, *E pur si muove: Galiliean-invariant cosmological hydrodynamical simulations on a moving mesh*, Mon. Not. Roy. Astron. Soc. **401**, 791 (2010) [arXiv:0901.4107 [astro-ph.CO]].

[118] V. Springel *et al.*, *First results from the IllustrisTNG simulations: matter and galaxy clustering*, Mon. Not. Roy. Astron. Soc. **475**, 676 (2018) [arXiv:1707.03397 [astro-ph.GA]].

[119] S. Genel, *The size evolution of star-forming and quenched galaxies in the IllustrisTNG simulation*, Mon. Not. Roy. Astron. Soc. **474**, 3976 (2018) [arXiv:1707.05327 [astro-ph.GA]].

[120] A. Pillepich *et al.*, *First results from the IllustrisTNG simulations: the stellar mass content of groups and clusters of galaxies*, Mon. Not. Roy. Astron. Soc. **475**, 648 (2018) [arXiv:1707.03406 [astro-ph.GA]].

[121] F. Marinacci *et al.*, *First results from the IllustrisTNG simulations: radio haloes and magnetic fields*, Mon. Not. Roy. Astron. Soc. **480**, 5113 (2018) [arXiv:1707.03396 [astro-ph.CO]].

[122] D. Nelson *et al.*, *First results from the IllustrisTNG simulations: the galaxy color bimodality*, Mon. Not. Roy. Astron. Soc. **475**, 624 (2018) [arXiv:1707.03395 [astro-ph.GA]].

[123] A. Pillepich *et al.*, *Simulating Galaxy Formation with the IllustrisTNG Model*, Mon. Not. Roy. Astron. Soc. **473**, no. 3, 4077 (2018) [arXiv:1703.02970 [astro-ph.GA]].

[124] R. Weinberger *et al.*, *Supermassive black holes and their feedback effects in the IllustrisTNG simulation*, Mon. Not. Roy. Astron. Soc. **479**, no. 3, 4056 (2018) [arXiv:1710.04659 [astro-ph.GA]].

[125] C. Arnlold and B. Li, in preparation (2018).

[126] M. Vogelsberger *et al.*, *Properties of galaxies reproduced by a hydrodynamic simulation*, Nature **509**, 177 (2014).

[127] M. Vogelsberger *et al.*, *Introducing the Illustris Project: Simulating the coevolution of dark and visible matter in the Universe*, Mon. Not. Roy. Astron. Soc. **444**, no. 2, 1518 (2014) [arXiv:1405.2921 [astro-ph.CO]].

[128] J. Schaye *et al.*, *The EAGLE project: Simulating the evolution and assembly of galaxies and their environments*, Mon. Not. Roy. Astron. Soc. **446**, 521 (2015) [arXiv:1407.7040 [astro-ph.GA]].

[129] J. Lesgourgues, S. Pastor, *Massive neutrinos and cosmology*, Phys. Rept. **429**, 307-379 (2006) [arXiv:astro-ph/0603494].

[130] A. M. Green, S. Hofmann, D. J. Schwarz, *Small scale wimp physics*, AIP Conf. Proc. **805**, 431-434 (2006) [arXiv:astro-ph/0508553].

[131] S. Profumo, K. Sigurdson, M. Kamionkowski, *What mass are the smallest protohalos?*, Phys. Rev. Lett. **97**, 031301 (2006) [arXiv:astro-ph/0603373].

[132] M. Viel, G. D. Becker, J. S. Bolton, M. G. Haehnelt, *Warm dark matter as a solution to the small scale crisis: New constraints from high redshift Lyman-α forest data*, Phys. Rev. D **88**, 043502 (2013) [arXiv:1306.2314 [astro-ph.CO]].

[133] V. Irsic *et al.*, *New Constraints on the free-streaming of warm dark matter from intermediate and small scale Lyman-α forest data*, [arXiv:1702.01764 [astro-ph.CO]].

[134] A. Boyarsky, J. Lesgourgues, O. Ruchayskiy, M. Viel, *Lyman-alpha constraints on warm and on warm-plus-cold dark matter models*, JCAP **0905**, 012 (2009) [arXiv:0812.0010 [astro-ph]].

[135] R. Adhikari *et al.*, *A White Paper on keV Sterile Neutrino Dark Matter*, JCAP **1701**, 025 (2017) [arXiv:1602.04816 [hep-ph]].

[136] E. Bulbul, M. Markevitch, A. Foster, R. K. Smith, M. Loewenstein, S. W. Randall, *Detection of An Unidentified Emission Line in the Stacked X-ray spectrum of Galaxy Clusters*, Astrophys. J. **789**, 13 (2014) [arXiv:1402.2301 [astro-ph.CO]].

[137] A. Boyarsky, O. Ruchayskiy, D. Iakubovskyi, J. France, *Unidentified Line in X-Ray Spectra of the Andromeda Galaxy and Perseus Galaxy Cluster*, Phys. Rev. Lett. **113**, 251301 (2014) [arXiv:1402.4119 [astro-ph.CO]].

[138] J. F. Cherry, S. Horiuchi, *Closing in on Resonantly Produced Sterile Neutrino Dark Matter*, Phys. Rev. D **95**, 083015 (2017) [arXiv:1701.07874 [hep-ph]].

[139] A. Schneider, *Astrophysical constraints on resonantly produced sterile neutrino dark matter*, JCAP **1604**, 059 (2016) [arXiv:1601.07553 [astro-ph.CO]].

[140] A. Merle, A. Schneider, M. Totzauer, *Dodelson-Widrow Production of Sterile Neutrino Dark Matter with Non-Trivial Initial Abundance*, JCAP **1604**, 003 (2016) [arXiv:1512.05369 [hep-ph]].

[141] M. Lovell, V. Eke, C. Frenk, L. Gao, A. Jenkins, T. Theuns, J. Wang, S. White, A. Boyarsky, O. Ruchayskiy, *The haloes of bright satellite galaxies in a warm dark matter universe*, Mon. Not. Roy. Astr. Soc. **420**, 2318-2324 (2012) [arXiv:1104.2929 [astro-ph.CO]].

[142] A. Schneider, R. E. Smith, A. V. Maccio, B. Moore, *Non-linear evolution of cosmological structures in warm dark matter models*, Mon. Not. R. Astron. Soc. **424**, 684-698 (2012) [arXiv:1112.0330 [astro-ph.CO]].

[143] A. Schneider, R. E. Smith, D. Reed, *Halo Mass Function and the Free Streaming Scale*, Mon. Not. Roy. Astron. Soc. **433**, 1573 (2013) [arXiv:1303.0839 [astro-ph.CO]].

[144] M. R. Lovell, C. S. Frenk, V. R. Eke, A. Jenkins, L. Gao, T. Theuns, *The properties of warm dark matter haloes*, Mon. Not. Roy. Astron. Soc. **439**, 300 (2014) [arXiv:1308.1399 [astro-ph.CO]].

[145] C. Power, *Seeking Observable Imprints of Small-Scale Structure on the Properties of Dark Matter Haloes*, Publ. Astron. Soc. Austral. **30**, 53 (2013) [arXiv:1309.1591 [astro-ph.CO]].

[146] C. Power, A. S. G. Robotham, D. Obreschkow, A. Hobbs, G. F. Lewis, *Spurious haloes and discreteness-driven relaxation in cosmological simulations*, Mon. Not. Roy. Astron. Soc. **462**, 474 (2016) [arXiv:1606.02038 [astro-ph.CO]].

[147] S. Bose, W. A. Hellwing, C. S. Frenk, A. Jenkins, M. R. Lovell, J. C. Helly, B. Li, *The COpernicus COmplexio: Statistical Properties of Warm Dark Matter Haloes*, Mon. Not. Roy. Astron. Soc. **455**, 318 (2016) [arXiv:1507.01998 [astro-ph.CO]].

[148] C. J. Hogan, J. J. Dalcanton, *New Dark Matter Physics: Clues from Halo Structure*, Phys. Rev. D **62**, 063511 (2000) [arXiv:astro-ph/0002330].

[149] A. V. Maccio', O. Ruchayskiy, A. Boyarsky, J. C. Munoz-Cuartas, *The inner structure of haloes in Cold+Warm dark matter models*, Mon. Not. Roy. Astron. Soc. **428**, 882-890 (2013) [arXiv:1202.2858 [astro-ph.CO]].

[150] S. Shao, L. Gao, T. Theuns, C. S. Frenk, *The phase-space density of fermionic dark matter haloes*, Mon. Not. R. Astron. Soc. **430**, 2346-2357 (2013) [arXiv:1209.5563 [astro-ph.CO]].

[151] J. Brandbyge, S. Hannestad, T. Haugbølle, B. Thomsen, *The Effect of Thermal Neutrino Motion on the Non-linear Cosmological Matter Power Spectrum*, JCAP **0808**, 020 (2008) [arXiv:0802.3700 [astro-ph]].

[152] M. Viel, M. G. Haehnelt, V. Springel, *The effect of neutrinos on the matter distribution as probed by the Intergalactic Medium*, JCAP **1006**, 015 (2010) [arXiv:1003.2422 [astro-ph.CO]].

[153] F. Villaescusa-Navarro, S. Bird, C. Peña-Garay, M. Viel, *Non-linear evolution of the cosmic neutrino background*, JCAP **03**, 019 (2013) [arXiv:1212.4855 [astro-ph.CO]].

[154] P. Colin, O. Valenzuela, V. Avila-Reese, *On the Structure of Dark Matter Halos at the Damping Scale of the Power Spectrum with and without Relict Velocities*, Astrophys. J. **673**, 203 (2008) [arXiv:0709.4027 [astro-ph]].

[155] A. Klypin, J. Holtzman, J. Primack, E. Regos, *Structure formation with cold plus hot dark matter*, Astrophys. J. **416**, 1 (1993) [arXiv:astro-ph/9305011].

[156] M. Viel, K. Markovic, M. Baldi, J. Weller, *The Non-Linear Matter Power Spectrum in Warm Dark Matter Cosmologies*, Mon. Not. R. Astron. Soc. **421**, 50-62 (2012) [arXiv:1107.4094 [astro-ph.CO]].

[157] S. Paduroiu, Y. Revaz, D. Pfenniger, *Structure formation in warm dark matter cosmologies: Top-Bottom Upside-Down*, [arXiv:1506.03789 [astro-ph.CO]].

[158] O. Hahn, R. E. Angulo, *An adaptively refined phase-space element method for cosmological simulations and collisionless dynamics*, Mon. Not. Roy. Astron. Soc. **455**, 1115 (2016) [arXiv:1501.01959 [astro-ph.CO]].

[159] A. Toomre, *On the gravitational stability of a disk of stars*, Astrophys. J. **139**, 1217 (1964).

[160] J. Lesgourgues, *The Cosmic Linear Anisotropy Solving System (CLASS) I: Overview*, [arXiv:1104.2932 [astro-ph.IM]].

[161] J. Lesgourgues, T. Tram, *The Cosmic Linear Anisotropy Solving System (CLASS) IV: efficient implementation of non-cold relics*, JCAP **09**, 032 (2011) [arXiv:1104.2935].

[162] N. Y. Gnedin, L. Hui, *Probing the universe with the Lyman alpha forest: 1. Hydrodynamics of the low density IGM*, Mon. Not. Roy. Astron. Soc. **296**, 44 (1998) [arXiv:astro-ph/9706219].

[163] A. Garzilli, A. Boyarsky, O. Ruchayskiy, *Cutoff in the Lyman α forest power spectrum: warm IGM or warm dark matter?*, Phys. Lett. B **773**, 258 (2017) [arXiv:1510.07006 [astro-ph.CO]].

[164] S. Pueblas, R. Scoccimarro, *Generation of Vorticity and Velocity Dispersion by Orbit Crossing*, Phys. Rev. D **80**, 043504 (2009) [arXiv:0809.4606 [astro-ph]].

[165] R. W. Hockney, J. W. Eastwood, *Computer simulation using particles*, New York: McGraw-Hill (1981).

[166] F. Bernardeau, R. van de Weygaert, *A new method for accurate estimation of velocity field statistics*, Mon. Not. Roy. Astron. Soc. **279**, 693 (1996) [arXiv:astro-ph/9508125].

[167] M. C. Cautun, R. van de Weygaert, *The DTFE public software - The Delaunay Tessellation Field Estimator code*, Astrophysics Source Code Library, ascl:1105.003 (2011) [arXiv:1105.0370 [astro-ph.IM]].

[168] C. M. Baugh, E. Gaztanaga, G. Efstathiou, *A Comparison of the evolution of density fields in perturbation theory and numerical simulations - 2. Counts-*

in-cells analysis, Mon. Not. Roy. Astron. Soc. **274**, 1049 (1995) [arXiv:astro-ph/9408057].

[169] J. Wang and S. D. M. White, *Discreteness effects in simulations of Hot/Warm dark matter*, Mon. Not. Roy. Astron. Soc. **380**, 93 (2007) [arXiv:astro-ph/0702575].

[170] Alejandro Benitez-Llambay (2015), py-sphviewer: Py-SPHViewer v1.0.0. Zenodo. 10.5281/zenodo.21703.

[171] S. Colombi, A. H. Jaffe, D. Novikov, C. Pichon, *Accurate estimators of power spectra in N-body simulations*, Mon. Not. Roy. Astron. Soc. **393**, 511 (2009) [arXiv:0811.0313 [astro-ph]].

[172] P. S. Behroozi, R. H. Wechsler, H. Wu , *The Rockstar Phase-Space Temporal Halo Finder and the Velocity Offsets of Cluster Cores*, ApJ **762**, 109 (2013) [arXiv:1110.4372 [astro-ph.CO]].

[173] G. L. Bryan, M. L. Norman, *Statistical Properties of X-ray Clusters: Analytic and Numerical Comparisons*, Astrophys. J. **495**, 80 (1998) [arXiv:astro-ph/9710107].

[174] C. Power, J. F. Navarro, A. Jenkins, C. S. Frenk, S. D. M. White, V. Springel, J. Stadel, T. Quinn ,*The Inner structure of Lambda CDM halos. 1. A Numerical convergence study*, Mon. Not. Roy. Astron. Soc. **338**, 14 (2003) [arXiv:astro-ph/0201544].

[175] J. h. He, B. Li and A. J. Hawken, *Effective dark matter power spectra in $f(R)$ gravity*, Phys. Rev. D **92**, no. 10, 103508 (2015) [arXiv:1505.03656 [astro-ph.CO]].

[176] Y. P. Jing, *Correcting for the alias effect when measuring the power spectrum using FFT*, Astrophys. J. **620**, 559 (2005) [astro-ph/0409240].

[177] W. H. Press, P. Schechter, *Formation of galaxies and clusters of galaxies by selfsimilar gravitational condensation*, Astrophys. J. **187**, 425 (1974).

[178] J. R. Bond, S. Cole, G. Efstathiou, N. Kaiser, *Excursion set mass functions for hierarchical Gaussian fluctuations*, Astrophys. J. **379**, 440 (1991).

[179] R. K. Sheth, G. Tormen, *Large scale bias and the peak background split*, Mon. Not. Roy. Astron. Soc. **308**, 119 (1999) [arXiv:astro-ph/9901122].

[180] A. R. Zentner, *The Excursion Set Theory of Halo Mass Functions, Halo Clustering, and Halo Growth*, Int. J. Mod. Phys. D **16**, 763 (2007) [arXiv:astro-ph/0611454].

[181] A. J. Benson, A. Farahi, S. Cole, L. A. Moustakas, A. Jenkins, M. Lovell, R. Kennedy, J. Helly, C. Frenk, *Dark matter halo merger histories beyond cold dark matter - I. Methods and application to warm dark matter*, MNRAS **428**, 1774B (2013) [arXiv:1209.3018 [astro-ph.CO]].

[182] A. Schneider, *Structure formation with suppressed small-scale perturbations*, Mon. Not. Roy. Astron. Soc. **451**, no. 3, 3117 (2015) [arXiv:1412.2133 [astro-ph.CO]].

[183] M. Maggiore, A. Riotto, *The Halo Mass Function from Excursion Set Theory. I. Gaussian fluctuations with non-Markovian dependence on the smoothing scale*, Astrophys. J. **711**, 907 (2010) [arXiv:0903.1249 [astro-ph.CO]].

[184] J. Carlson, M. White, N. Padmanabhan, *Critical look at cosmological perturbation theory techniques*, Phys. Rev. D **80**, 043531 (2009) [arXiv:0905.0479 [astro-ph.CO]].

[185] D. H. Lyth, E. D. Stewart, *Cosmology with a TeV mass GUT Higgs*, Phys. Rev. Lett. **75**, 201 (1995) [arXiv:hep-ph/9502417].

[186] D. H. Lyth, E. D. Stewart, *Thermal inflation and the moduli problem*, Phys. Rev. D **53**, 1784 (1996) [hep-ph/9510204].

[187] T. Banks, D. B. Kaplan, A. E. Nelson, *Cosmological implications of dynamical supersymmetry breaking*, Phys. Rev. D **49**, 779 (1994) [arXiv:hep-ph/9308292].

[188] B. de Carlos, J. A. Casas, F. Quevedo, E. Roulet, *Model independent properties and cosmological implications of the dilaton and moduli sectors of 4-d strings*, Phys. Lett. B **318**, 447 (1993) [arXiv:hep-ph/9308325].

[189] K. Cho, S. E. Hong, E. D. Stewart, H. Zoe, *CMB Spectral Distortion Constraints on Thermal Inflation*, JCAP **1708**, no. 08, 002 (2017) [arXiv:1705.02741 [astro-ph.CO]].

[190] S. E. Hong, H. Zoe, K. Ahn, *Small-scale Effects of Thermal Inflation on Halo Abundance at High-z, Galaxy Substructure Abundance and 21-cm Power Spectrum*, Phys. Rev. D **96**, no. 10, 103515 (2017) [arXiv:1706.08049 [astro-ph.CO]].

[191] J. Lesgourgues, D. Polarski, A. A. Starobinsky, *CDM models with a BSI step - like primordial spectrum and a cosmological constant*, Mon. Not. Roy. Astron. Soc. **297**, 769 (1998) [arXiv:astro-ph/9711139].

[192] F. Y. Cyr-Racine, K. Sigurdson, J. Zavala, T. Bringmann, M. Vogelsberger, C. Pfrommer, *ETHOS - an effective theory of structure formation: From dark particle physics to the matter distribution of the Universe*, Phys. Rev. D **93**, no. 12, 123527 (2016) [arXiv:1512.05344 [astro-ph.CO]].

[193] M. Vogelsberger, J. Zavala, F. Y. Cyr-Racine, C. Pfrommer, T. Bringmann, K. Sigurdson, *ETHOS - an effective theory of structure formation: dark matter physics as a possible explanation of the small-scale CDM problems*, Mon. Not. Roy. Astron. Soc. **460**, no. 2, 1399 (2016) [arXiv:1512.05349 [astro-ph.CO]].

[194] M. R. Lovell *et al.*, *Satellite galaxies in semi-analytic models of galaxy formation with sterile neutrino dark matter*, Mon. Not. Roy. Astron. Soc. **461**, no. 1, 60 (2016) [arXiv:1511.04078 [astro-ph.CO]].

[195] M. R. Lovell *et al.*, *ETHOS - an effective theory of structure formation: predictions for the high-redshift Universe - abundance of galaxies and reionization*, Mon. Not. Roy. Astron. Soc. **477**, no. 3, 2886 (2018) [arXiv:1711.10497 [astro-ph.CO]].

[196] M. P. van Daalen, J. Schaye, I. G. McCarthy, C. M. Booth, C. Dalla Vecchia, *The impact of baryonic processes on the two-point correlation functions of galaxies, subhaloes and matter*, Mon. Not. Roy. Astron. Soc. **440**, no. 4, 2997 (2014) [arXiv:1310.7571 [astro-ph.CO]].

[197] T. Sawala *et al.*, *The APOSTLE simulations: solutions to the Local Group's cosmic puzzles*, Mon. Not. Roy. Astron. Soc. **457**, no. 2, 1931 (2016) [arXiv:1511.01098 [astro-ph.GA]].

[198] W. A. Hellwing, M. Schaller, C. S. Frenk, T. Theuns, J. Schaye, R. G. Bower, R. A. Crain, *The effect of baryons on redshift space distortions and cosmic density and velocity fields in the EAGLE simulation*, Mon. Not. Roy. Astron. Soc. **461**, no. 1, L11 (2016) [arXiv:1603.03328 [astro-ph.CO]].

[199] M. C. Artale *et al.*, *Small-scale galaxy clustering in the EAGLE simulation*, Mon. Not. Roy. Astron. Soc. **470**, no. 2, 1771 (2017) [arXiv:1611.05064 [astro-ph.GA]].

[200] M. R. Lovell *et al.*, *Properties of Local Group galaxies in hydrodynamical simulations of sterile neutrino dark matter cosmologies*, Mon. Not. Roy. Astron. Soc. **468**, 4285-4298 (2017) [arXiv:1611.00010 [astro-ph.GA]].

[201] J. D. Bowman, A. E. E. Rogers, R. A. Monsalve, T. J. Mozdzen, N. Mahesh, *An absorption profile centred at 78 megahertz in the sky-averaged spectrum*, Nature **555**, 67–70 (2018).

[202] A. Schneider, *Constraining Non-Cold Dark Matter Models with the Global 21-cm Signal*, (2018) [arXiv:1805.00021 [astro-ph.CO]].

[203] A. Lidz, L. Hui, *The Implications of a Pre-reionization 21 cm Absorption Signal for Fuzzy Dark Matter*, (2018) [arXiv:1805.01253 [astro-ph.CO]].

[204] J. P. Gardner *et al.*, *The James Webb Space Telescope*, Space Sci. Rev. **123**, 485 (2006) [arXiv:astro-ph/0606175].

[205] R. Davies *et al.*, *MICADO: first light imager for the E-ELT*, Ground-based and Airborne Instrumentation for Astronomy VI **9908**, 99081Z (2016) [arXiv:1607.01954 [astro-ph.IM]].

[206] R. Li, C. S. Frenk, S. Cole, L. Gao, S. Bose, W. A. Hellwing, *Constraints on the identity of the dark matter from strong gravitational lenses*, Mon. Not. Roy. Astron. Soc. **460**, 363 (2016) [arXiv:1512.06507 [astro-ph.CO]].

[207] M. Cataneo *et al.*, *New constraints on $f(R)$ gravity from clusters of galaxies*, Phys. Rev. D **92**, no. 4, 044009 (2015) [arXiv:1412.0133 [astro-ph.CO]].

[208] H. Wilcox *et al.*, *The XMM Cluster Survey: Testing chameleon gravity using the profiles of clusters*, Mon. Not. Roy. Astron. Soc. **452**, no. 2, 1171 (2015) [arXiv:1504.03937 [astro-ph.CO]].

[209] X. Liu *et al.*, *Constraining $f(R)$ Gravity Theory Using Weak Lensing Peak Statistics from the Canada-France-Hawaii-Telescope Lensing Survey*, Phys. Rev. Lett. **117**, no. 5, 051101 (2016) [arXiv:1607.00184 [astro-ph.CO]].

[210] S. Peirone, M. Raveri, M. Viel, S. Borgani and S. Ansoldi, *Constraining f(R) Gravity with Planck Sunyaev-Zel'dovich Clusters*, Phys. Rev. D **95**, no. 2, 023521 (2017) [arXiv:1607.07863 [astro-ph.CO]].

[211] L. Lombriser, F. Simpson and A. Mead, *Unscreening Modified Gravity in the Matter Power Spectrum*, Phys. Rev. Lett. **114**, no. 25, 251101 (2015) [arXiv:1501.04961 [astro-ph.CO]].

[212] Y. C. Cai, N. Padilla and B. Li, *Testing Gravity using Cosmic Voids*, Mon. Not. Roy. Astron. Soc. **451**, no. 1, 1036 (2015) [arXiv:1410.1510 [astro-ph.CO]].

[213] M. Cautun, E. Paillas, Y. C. Cai, S. Bose, J. Armijo, B. Li and N. Padilla, *The Santiago-Harvard-Edinburgh-Durham void comparison – I. SHEDding light on chameleon gravity tests*, Mon. Not. Roy. Astron. Soc. **476**, no. 3, 3195 (2018) [arXiv:1710.01730 [astro-ph.CO]].

[214] J. Armijo, Y. C. Cai, N. Padilla, B. Li and J. A. Peacock, *Testing modified gravity using a marked correlation function*, Mon. Not. Roy. Astron. Soc. **478**, no. 3, 3627 (2018) [arXiv:1801.08975 [astro-ph.CO]].

[215] C. Hernàndez-Aguayo, C. M. Baugh and B. Li, *Marked clustering statistics in $f(R)$ gravity cosmologies*, Mon. Not. Roy. Astron. Soc. **479**, no. 4, 4824 (2018) [arXiv:1801.08880 [astro-ph.CO]].

[216] A. Terukina, L. Lombriser, K. Yamamoto, D. Bacon, K. Koyama and R. C. Nichol, *Testing chameleon gravity with the Coma cluster*, JCAP **1404**, 013 (2014) [arXiv:1312.5083 [astro-ph.CO]].

[217] S. Bharadwaj, B. B. Nath, B. B. Nath and S. K. Sethi, *Using HI to probe large scale structures at $z \sim 3$*, J. Astrophys. Astron. **22**, 21 (2001) [astro-ph/0003200].

[218] A. Loeb and S. Wyithe, *Precise Measurement of the Cosmological Power Spectrum With a Dedicated 21cm Survey After Reionization*, Phys. Rev. Lett. **100**, 161301 (2008) [arXiv:0801.1677 [astro-ph]].

[219] P. Bull *et al.*, *Late-time cosmology with 21cm intensity mapping experiments*, Astrophys. J. **803**, no. 1, 21 (2015) [arXiv:1405.1452 [astro-ph.CO]].

[220] M. G. Santos *et al.*, *Cosmology with a SKA HI intensity mapping survey*, PoS AASKA14 (2015) 019 [arXiv:1501.03989 [astro-ph.CO]].

[221] F. Villaescusa-Navarro *et al.*, *Ingredients for 21 cm Intensity Mapping*, Astrophys. J. **866**, no. 2, 135 (2018) [arXiv:1804.09180 [astro-ph.CO]].

[222] F. Villaescusa-Navarro, P. Bull and M. Viel, *Weighing neutrinos with cosmic neutral hydrogen*, Astrophys. J. **814**, no. 2, 146 (2015) [arXiv:1507.05102 [astro-ph.CO]].

[223] I. P. Carucci, F. Villaescusa-Navarro, M. Viel and A. Lapi, *Warm dark matter signatures on the 21cm power spectrum: Intensity mapping forecasts for SKA*, JCAP **1507**, no. 07, 047 (2015) [arXiv:1502.06961 [astro-ph.CO]].

[224] I. P. Carucci, P. S. Corasaniti and M. Viel, *Imprints of non-standard Dark Energy and Dark Matter Models on the 21cm Intensity Map Power Spectrum*, JCAP **1712**, no. 12, 018 (2017) [arXiv:1706.09462 [astro-ph.CO]].

[225] E. McDonough and R. H. Brandenberger, *Searching for Signatures of Cosmic String Wakes in 21cm Redshift Surveys using Minkowski Functionals*, JCAP **1302** (2013) 045 [arXiv:1109.2627 [astro-ph.CO]].

[226] Y. Wang *et al.*, *Topology of neutral hydrogen distribution with the Square Kilometre Array*, PoS AASKA **14**, 033 (2015) [arXiv:1501.00749 [astro-ph.CO]].

[227] P. Brax, C. van de Bruck, A. C. Davis and D. J. Shaw, *f(R) Gravity and Chameleon Theories*, Phys. Rev. D **78**, 104021 (2008) [arXiv:0806.3415 [astro-ph]].

[228] J. Wang, L. Hui and J. Khoury, *No-Go Theorems for Generalized Chameleon Field Theories*, Phys. Rev. Lett. **109**, 241301 (2012) [arXiv:1208.4612 [astro-ph.CO]].

[229] J. J. Ceron-Hurtado, J. h. He and B. Li, *Can background cosmology hold the key for modified gravity tests?*, Phys. Rev. D **94**, no. 6, 064052 (2016) [arXiv:1609.00532 [astro-ph.CO]].

[230] I. Sawicki and E. Bellini, *Limits of quasistatic approximation in modified-gravity cosmologies*, Phys. Rev. D **92**, no. 8, 084061 (2015) [arXiv:1503.06831 [astro-ph.CO]].

[231] C. M. Will, *The Confrontation between General Relativity and Experiment*, Living Rev. Rel. **17**, 4 (2014) [arXiv:1403.7377 [gr-qc]].

[232] J. Khoury and A. Weltman, *Chameleon cosmology*, Phys. Rev. D **69**, 044026 (2004) [astro-ph/0309411].

[233] J. Khoury and A. Weltman, *Chameleon fields: Awaiting surprises for tests of gravity in space*, Phys. Rev. Lett. **93**, 171104 (2004) [astro-ph/0309300].

[234] B. P. Abbott *et al.* [LIGO Scientific and Virgo and Fermi-GBM and INTEGRAL Collaborations], *Gravitational Waves and Gamma-rays from a Binary Neutron Star Merger: GW170817 and GRB 170817A*, Astrophys. J. **848**, no. 2, L13 (2017) [arXiv:1710.05834 [astro-ph.HE]]

[235] F. Schmidt, *Dynamical Masses in Modified Gravity*, Phys. Rev. D **81**, 103002 (2010) [arXiv:1003.0409 [astro-ph.CO]].

[236] G. B. Zhao, B. Li and K. Koyama, *Testing General Relativity using the Environmental Dependence of Dark Matter Halos*, Phys. Rev. Lett. **107**, 071303 (2011) [arXiv:1105.0922 [astro-ph.CO]].

[237] Y. Li and W. Hu, *Chameleon Halo Modeling in f(R) Gravity*, Phys. Rev. D **84**, 084033 (2011) [arXiv:1107.5120 [astro-ph.CO]].

[238] L. Lombriser, J. Yoo and K. Koyama, *Relativistic effects in galaxy clustering in a parametrized post-Friedmann universe*, Phys. Rev. D **87**, 104019 (2013) [arXiv:1301.3132 [astro-ph.CO]].

[239] E. Puchwein, M. Baldi and V. Springel, *Modified Gravity-GADGET: A new code for cosmological hydrodynamical simulations of modified gravity models*, Mon. Not. Roy. Astron. Soc. **436**, 348 (2013) [arXiv:1305.2418 [astro-ph.CO]].

[240] C. Arnold, E. Puchwein and V. Springel, *Scaling relations and mass bias in hydrodynamical $f(R)$ gravity simulations of galaxy clusters*, Mon. Not. Roy. Astron. Soc. **440**, no. 1, 833 (2014) [arXiv:1311.5560 [astro-ph.CO]].

[241] C. Arnold, P. Fosalba, V. Springel, E. Puchwein and L. Blot, *The modified gravity lightcone simulation project I: Statistics of matter and halo distributions*, Mon. Not. Roy. Astron. Soc. **483**, 790 (2019) [arXiv:1805.09824 [astro-ph.CO]].

[242] A. Rahmati, A. P. Pawlik, M. Raicevic and J. Schaye, *On the evolution of the HI column density distribution in cosmological simulations*, Mon. Not. Roy. Astron. Soc. **430**, 2427 (2013) [arXiv:1210.7808 [astro-ph.CO]].

[243] L. Hui and N. Y. Gnedin, *Equation of state of the photoionized intergalactic medium*, Mon. Not. Roy. Astron. Soc. **292**, 27 (1997) [astro-ph/9612232].

[244] A. Rahmati, J. Schaye, R. G. Bower, R. A. Crain, M. Furlong, M. Schaller and T. Theuns, *The distribution of neutral hydrogen around high-redshift galaxies and quasars in the EAGLE simulation*, Mon. Not. Roy. Astron. Soc. **452**, no. 2, 2034 (2015) [arXiv:1503.05553 [astro-ph.CO]].

[245] J. Schaye, *Model independent insights into the nature of the Lyman-alpha forest and the distribution of matter in the universe*, Astrophys. J. **559**, 507 (2001) [astro-ph/0104272].

[246] F. Haardt, and P Madau, *Modelling the UV/X-ray cosmic background with CUBA*, Clusters of Galaxies and the High Redshift Universe Observed in X-rays, Neumann, D. M. and Tran, J. T. V., eds. (2001).

[247] T. Theuns, A. Leonard, G. Efstathiou, F. R. Pearce and P. A. Thomas, *P**3M-SPH simulations of the lyman-alpha forest,* Mon. Not. Roy. Astron. Soc. **301**, 478 (1998) [astro-ph/9805119].

[248] M. R. Krumholz, C. F. McKee and J. Tumlinson, *The Atomic to Molecular Transition in Galaxies. I: An Analytic Approximation for Photodissociation Fronts in Finite Clouds*, Astrophys. J. **689** (2008) 865 [arXiv:0805.2947 [astro-ph]].

[249] M. R. Krumholz, C. F. McKee and J. Tumlinson, *The Atomic to Molecular Transition in Galaxies. II: HI and H_2 Column Densities*, Astrophys. J. **693**, 216 (2009) [arXiv:0811.0004 [astro-ph]].

[250] C. F. McKee, Christopher F. and M. R. Krumholz, *The Atomic-to-Molecular Transition in Galaxies. III. A New Method for Determining the Molecular Content of Primordial and Dusty Clouds*, Astrophys. J. **709**, 308 (2010) [arXiv:0908.0330 [astro-ph.GA]]

[251] S. M. Rao, D. A. Turnshek and D. B. Nestor, *Damped lyman alpha systems at z<1.65: the expanded sdss hst sample*, Astrophys. J. **636**, 610 (2006) [astro-ph/0509469].

[252] P. Lah *et al.*, *The HI content of star-forming galaxies at z = 0.24*, Mon. Not. Roy. Astron. Soc. **376**, 1357 (2007) [astro-ph/0701668].

[253] P. Noterdaeme *et al.*, *Column density distribution and cosmological mass density of neutral gas: Sloan Digital Sky Survey-III Data Release 9*, A&A, **547**, L1 (2012) [arXiv:1210.1213 [astro-ph.CO]]

[254] M. Davis, G. Efstathiou, C. S. Frenk, S. D. M. White, *The evolution of large-scale structure in a universe dominated by cold dark matter*, Astrophys. J. **292**, 371 (1985).

[255] I. P. Carucci, F. Villaescusa-Navarro and M. Viel, *The cross-correlation between 21 cm intensity mapping maps and the Ly? forest in the post-reionization era*, JCAP **1704**, no. 04, 001 (2017) [arXiv:1611.07527 [astro-ph.CO]].

[256] J. h. He, L. Guzzo, B. Li and C. M. Baugh, *No evidence for modifications of gravity from galaxy motions on cosmological scales*, Nat. Astron. **2**, no. 12, 967 (2018) [arXiv:1809.09019 [astro-ph.CO]].

[257] M. R. Blanton *et al.* [SDSS Collaboration], *NYU-VAGC: A Galaxy catalog based on new public surveys*, Astron. J. **129**, 2562 (2005) [astro-ph/0410166].

[258] R. Ansari *et al.* [Cosmic Visions 21 cm Collaboration], *Inflation and Early Dark Energy with a Stage II Hydrogen Intensity Mapping experiment*, [arXiv:1810.09572 [astro-ph.CO]].

[259] F. B. Abdalla *et al.* [Cosmology SWG Collaboration], *Cosmology from HI galaxy surveys with the SKA*, [arXiv:1501.04035 [astro-ph.CO]].

[260] P. Bull, *Extending cosmological tests of General Relativity with the Square Kilometre Array*, Astrophys. J. **817**, no. 1, 26 (2016) [arXiv:1509.07562 [astro-ph.CO]].

[261] O. Sameie, A. J. Benson, L. V. Sales, H. B. Yu, L. A. Moustakas and P. Creasey, *The effect of dark matter-dark radiation interactions on halo abundance – a Press-Schechter approach*, [arXiv:1810.11040 [astro-ph.CO]].

[262] L. Gao, T. Theuns, *Lighting the Universe with filaments*, Science **317**, 1527 (2007) [arXiv:0709.2165 [astro-ph]].

[263] S. Hirano, J. M. Sullivan, V. Bromm, *First star formation in ultralight particle dark matter cosmology*, Mon. Not. Roy. Astron. Soc. **473**, no. 1, L6 (2018) [arXiv:1706.00435 [astro-ph.CO]].

[264] Z. Haiman, M. Spaans and E. Quataert, *Lyman alpha cooling radiation from high-redshift halos*, Astrophys. J. **537**, L5 (2000) [astro-ph/0003366].

[265] C.-A. Faucher-Giguere, D. Keres, M. Dijkstra, L. Hernquist and M. Zaldarriaga, *Lyman-alpha Cooling Emission from Galaxy Formation*, Astrophys. J. **725**, 633 (2010) [arXiv:1005.3041 [astro-ph.CO]].

[266] S. Bag, R. Mondal, P. Sarkar, S. Bharadwaj, T. R. Choudhury, V. Sahni, *Studying the morphology of HI isodensity surfaces during reionization using Shapefinders and percolation analysis*, (2018) [arXiv:1809.05520 [astro-ph.CO]].

Appendix A

Numerical convergence

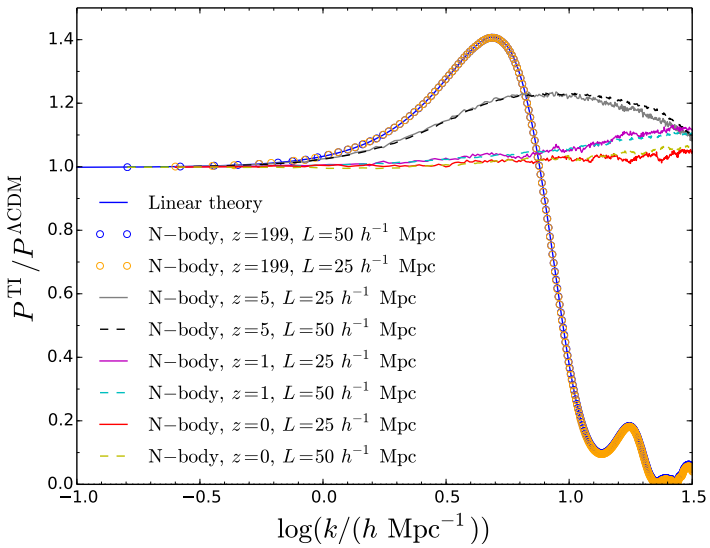

Figure A.1: Ratios of the matter power spectrum measured from simulations of thermal inflation with $k_b = 3\,\mathrm{Mpc}^{-1}$ with respect to that from standard ΛCDM at redshifts $z = 199, 5, 1, 0$. Solid curves represent simulations with $L = 25\,h^{-1}\,\mathrm{Mpc}$, while dashed curves show simulations with $L = 50\,h^{-1}\,\mathrm{Mpc}$. The solid blue line shows the linear theory prediction and is mostly obscured by the orange symbols. Blue symbols show results from ICs at $z = 199$ for simulations with $L = 50\,h^{-1}\,\mathrm{Mpc}$, while orange symbols are from ICs of simulations with $L = 25\,h^{-1}\,\mathrm{Mpc}$.

In this appendix, we study the accuracy of simulations with box length and particle number $\{L = 25\,h^{-1}\,\mathrm{Mpc}, N = 512^3\}$ for the model of thermal inflation studied in Chapter 5. We have run another set of simulations with parameters $\{L = 50\,h^{-1}\,\mathrm{Mpc}, N = 512^3\}$, for both the standard ΛCDM and the thermal inflation with $k_b = 3\,\mathrm{Mpc}^{-1}$. In Figure A.1 we show the ratio of the power spectrum measured

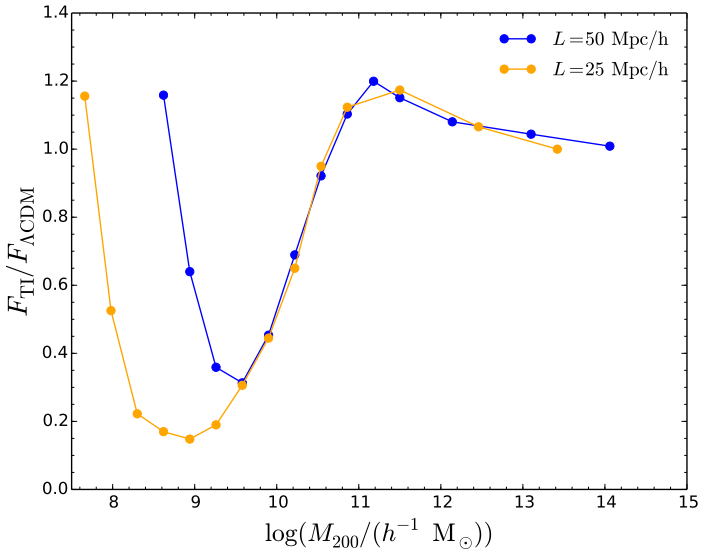

Figure A.2: Ratio of the halo mass function measured from simulations of thermal inflation with $k_b = 3\,\mathrm{Mpc}^{-1}$ with respect to that from standard ΛCDM at redshift $z = 0$. Blue symbols show results from simulations with $L = 50\,h^{-1}\,\mathrm{Mpc}$, while orange symbols show results from the smaller box, $L = 25\,h^{-1}\,\mathrm{Mpc}$.

from the thermal inflation model with respect to that from standard ΛCDM at redshifts $z = 5, 1$ and 0 for simulations with $L = 50\,h^{-1}\,\mathrm{Mpc}$ (dashed curves) and $L = 25\,h^{-1}\,\mathrm{Mpc}$ (solid curves). As can be seen from the figure, the power spectra measured from the simulations with different box lengths are in good agreement at small wavenumbers (up to the Nyquist frequency of the larger box simulation).

A similar analysis can be done for the halo mass function. In Figure A.2 we show the results at $z = 0$ for this quantity measured from simulations with $L = 50\,h^{-1}\,\mathrm{Mpc}$ and $L = 25\,h^{-1}\,\mathrm{Mpc}$. As we can see, the numerical results from the two boxes converge at large halo masses, $M_{200} > 10^{10}\,h^{-1}\,\mathrm{M}_\odot$. At lower masses the results from the larger box are dominated by spurious structures as expected.